# The chemical composition of hot compact stars

**Master's thesis in Physics**

Presented by

**Matti Dorsch**

21. 03. 2019

Dr. Karl Remeis Sternwarte Bamberg
Friedrich-Alexander-Universität Erlangen-Nürnberg



Supervisors:
Prof. Dr. Ulrich Heber
Dr. Marilyn Latour

# Abstract

Nuclear fusion during different stages in stellar evolution changes the abundance of elements, from the fusion of hydrogen to helium in main sequence stars to the synthesis of the heavy metals through neutron capture in the atmospheres of the highly evolved asymptotic giant branch stars. Therefore, the determination of element abundances in stellar atmospheres can give important clues about stellar evolution. This work sets out to study the peculiar metal abundance pattern in the atmospheres of helium-rich hot subdwarf stars, a group of stars whose origin is not fully understood yet.

Hot subdwarf stars are core helium burning stars that represent late stages in the evolution of low-mass stars. They can be divided into two classes: subdwarf B stars (sdB) with effective surface temperatures between $20\,000\,\mathrm{K}$ and $38\,000\,\mathrm{K}$ and subdwarf O stars (sdO) at higher temperatures. Unlike other core helium burning stars, hot subdwarfs are compact stars that have a hydrogen envelope too thin to sustain hydrogen shell burning.

Recently, extreme enrichment in several heavy elements (such as yttrium, zirconium, tin, and lead) with respect to the Sun was found in the small group of intermediately helium-rich sdOB stars (iHe sdOBs). This work adds three new stars to this class of "heavy metal" stars: HD 127493, HZ 44, and Feige 46. The abundance analysis performed is based on modern model atmospheres and synthetic spectra computed with the Tlusty/Synspec software package. These models were used to derive the atmospheric parameters (effective temperature, surface gravity, and helium abundance) from optical hydrogen and helium lines. A detailed metal abundance analysis using these parameters was performed based on high-resolution optical and ultra-violet spectra. To derive the abundances of elements heavier than zinc, additional atomic data were added to Synspec. Atomic data for transitions in ionized heavy elements (most importantly wavelengths and oscillator strengths) were collected from several theoretical works. Stellar masses were determined by combining atmospheric parameters, photometric data, and precise parallax distance measurements from the *Gaia* satellite.

The abundances of 28 metallic elements were determined in HZ 44, 14 in HD 127493, and 9 in Feige 46. Upper limits were derived for 14 elements in HZ 44 and 17 in HD 127493. HD 127493 and HZ 44 are about 10 000 times enriched in lead, while HZ 44 is also about 1500 times enriched in zirconium. Both stars are enriched in nitrogen, but depleted in carbon and oxygen, indicating that material processed through hydrogen fusion in the CNO-cycle was mixed to the surface. Feige 46 is very similar to the prototypical iHe sdOB, LS IV−14°116, and shares its extreme enrichment in zirconium and strontium at about 20 000 times solar. In contrast to HD 127493 and HZ 44, it is enriched in carbon and nitrogen and depleted in oxygen.

The derived masses for HD 127493 and HZ 44 are consistent with the canonical subdwarf mass of $0.47\,M_\odot$.

Since both HD 127493 and HZ 44 are hotter than the previously studied heavy-metal rich subdwarfs, this class might span a broader temperature range than previously thought. This might be because the important optical Zr IV and Pb IV lines become very weak at temperatures above $40\,000\,\mathrm{K}$, even at very high enrichment, which means that a possible enhancement can only be found from ultraviolet spectra. A short test performed in this work revealed that the He-sdO CD−31° 4800 does not share this extreme enrichment. Hydrogen-rich sdBs are known to be enriched in Ge and Pb, but not to the extend observed in iHe sdOBs. The observed overabundances in heavy elements are likely linked to the effects of diffusion.

# Contents

# 1    Introduction

For a long time, the origin of the chemical elements was an unsolved mystery. While the role of carbon, nitrogen, and oxygen as catalysts in the fusion of hydrogen to helium (the so-called CNO-process) was discussed already by von Weizsäcker (1937, 1938) and Bethe (1939), it took until 1946, when Hoyle (1946) considered the possibility that nuclear fusion in the cores of collapsing stars synthesizes heavier elements from hydrogen and helium. He later refined this theory in Hoyle (1954) where he explained how nuclear fusion in massive stars could create elements from carbon to iron. It wasn't until the famous paper by Burbidge et al. (1957) that the creation of elements heavier than iron through neutron-capture in stars became widely accepted. Today, the determination of the abundance of heavy elements in the atmospheres of many stars has been found to be in good agreement with the predictions of nuclear synthesis calculations. However, not all stars show abundance patterns consistent with these predictions. For example, a small group of so-called subdwarf stars have recently been found to be more than 10 000 times enriched with respect to the Sun in the heavy elements zirconium and lead (Naslim et al. 2011, 2013; Jeffery et al. 2017b). Similar observations were made for several helium-rich hot white dwarf stars (Rauch et al. 2017b; Werner et al. 2018). This extreme enrichment is not directly predicted by nuclear synthesis, but can likely be explained by an entirely different process; it is thought to be the result of strong diffusion effects in the peculiar atmospheres of these types of stars. This work will add three new stars to the list of "heavy metal" stars. In the following introductory chapter I start by giving a short overview over the characteristics and evolution of white dwarf and hot subdwarf stars.

## 1.1    Stellar evolution: White dwarf and hot subdwarf stars

This work is focused on studying the abundance of heavy elements in the atmospheres hot, compact stars. There are two main types of these stars: white dwarf stars and the somewhat less well known hot subdwarf stars. White dwarf (WD) stars are characterized by very high surface gravities and surface temperatures that range from the hottest stars known, with temperatures above 120 000 K, down to about 6 000 K (compare Fig. 1). Subdwarf stars span a temperature range between 20 000 K and 38 000 K (sdB) and up to 100 000 K (sdO, Schönberner & Drilling 1984), but have lower surface gravities (and are therefore more luminous at the same temperature).
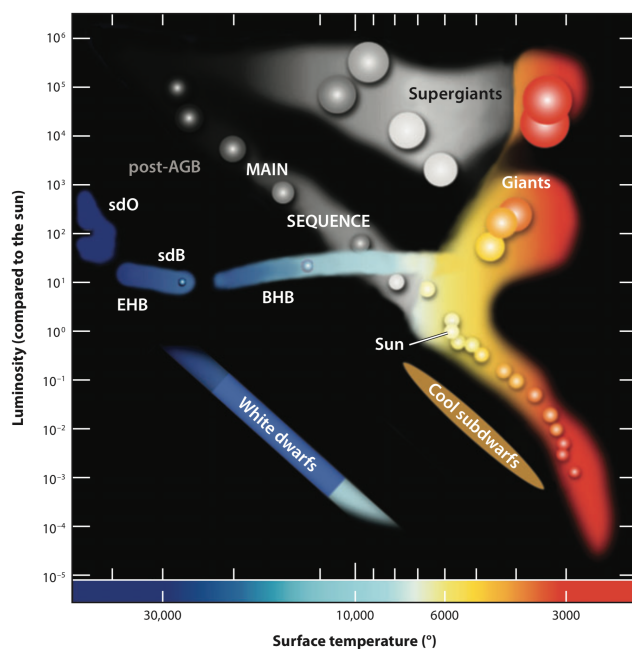


**Figure 1.**    Hertzsprung-Russell diagram (HRD): Hot subdwarfs populate the region below the upper main-sequence O- and B-stars and above the white dwarf cooling sequence. Taken from Heber (2009).

White dwarfs represent the final stage in the evolution of low-mass stars, such as the Sun. The

majority of stars is sustained by nuclear fusion, starting with the fusion of hydrogen to helium in main sequence (MS) stars. After the hydrogen reservoir in their core is exhausted, stars leave the main sequence as nuclear fusion continues in a shell around the core. For solar-mass stars, this happens after approximately nine billion years. Since the core is no longer sustained by fusion, it contracts and heats up in the process. As a result, the stellar envelope expands dramatically and the surface temperature drops. This is why this phase in stellar evolution is called the red giant branch (RGB) phase. Helium ashes from the shell fusion accumulate in the core and the central temperature slowly rises as the core contracts and is stabilized by the pressure of the now degenerate electron gas. After about one billion years on the RGB, the central temperatures are high enough to ignite He-fusion in the degenerate core. Because of electron degeneracy the core can not immediately expand at the onset of He-burning and temperatures rise rapidly, which in turn accelerates He fusion. This runaway process, the so-called He-flash, only stops when the core finally becomes non-degenerate and expands. The stars then depart from the RGB and spend about 100 million years on the so-called horizontal branch (HB), while they fuse helium to carbon and oxygen in their core as well as hydrogen to helium in a shell surrounding it. The eventual exhaustion of helium in the core leads to a second giant phase, the asymptotic giant branch (AGB), as both hydrogen and helium fusion continue in the envelope. Solar-mass stars never reach core temperatures high enough to ignite carbon fusion. In a final stage of stellar evolution, they shed their envelopes through a set of thermal pulses that result from instabilities between the hydrogen- and helium-burning shells. The ejected envelope can then briefly be observed as a so-called planetary nebula (PN), which disperses after about 10 000 years. The central star of this nebula (CSPN) is often observed as a very hot white dwarf that will then cool down over the course of billions of years. White dwarf stars no longer experience nuclear fusion and are only sustained by the degenerate electron pressure in their cores. Hot subdwarfs, in contrast, are core helium burning stars. What distinguishes them from normal HB stars is that their hydrogen envelope is not massive enough to sustain H shell fusion – they do not evolve through a second giant phase but transition directly to the WD cooling sequence once He fusion ceases in their core. This lack of an extended envelope is why their masses are thought to be close to the mass required for the the He-flash (~0.47 $M_\odot$; Han et al. 2002), at least for those subdwarfs that are not the result of the merging of two He-WDs. The mass distribution of hot subdwarfs has been confirmed to peak at this canonical mass by observations (Fontaine et al. 2012; Van Grootel et al. 2013).

### 1.1.1 The hot subdwarf population

Only recently quantitative spectral analyses have been performed for a large number of hot subdwarfs. The effective temperatures and He abundances found by four of the largest surveys are shown in Fig. 2. The largest group of analyzed hot subdwarfs are of spectral type B. These stars populate the extreme horizontal branch (EHB), which extends the HB toward higher temperatures. About 50 % of them are found in close binary systems (Maxted et al. 2001; Copperwheat et al. 2011). The helium abundance in sdBs has been found to increase with temperature in two distinct sequences (Edelmann et al. 2003). Only about 5 % of sdBs have helium-dominated atmospheres (Ahmad & Jeffery 2006), including one of the stars discussed here: Feige 46.

The majority of sdO stars have atmospheres dominated by helium. They do not seem to follow a tight helium sequence such as the sdBs. In addition, their atmospheric metal abundances vary significantly. Stroeer et al. (2007) and Hirsch (2009) showed that He-sdOs can be sorted into three types based on their carbon and nitrogen abundances. Most He-sdOs in the temperature range between 40 000 K and 43 000 K are enriched in nitrogen, but depleted in carbon and oxygen ("type N"). Two of the stars discussed here, HD 127493 and HZ 44, belong to this category. A group He-sdOs enriched in both carbon and nitrogen is found at slightly higher temperatures ("type CN"). The smallest group of He-sdOs is enriched in carbon but depleted in nitrogen ("type C"). Helium-sdOs seem to have a significantly lower binary fraction than sdBs (Napiwotzki et al. 2004).

A very small number of hot subluminous stars are of mixed H/He composition. Because their
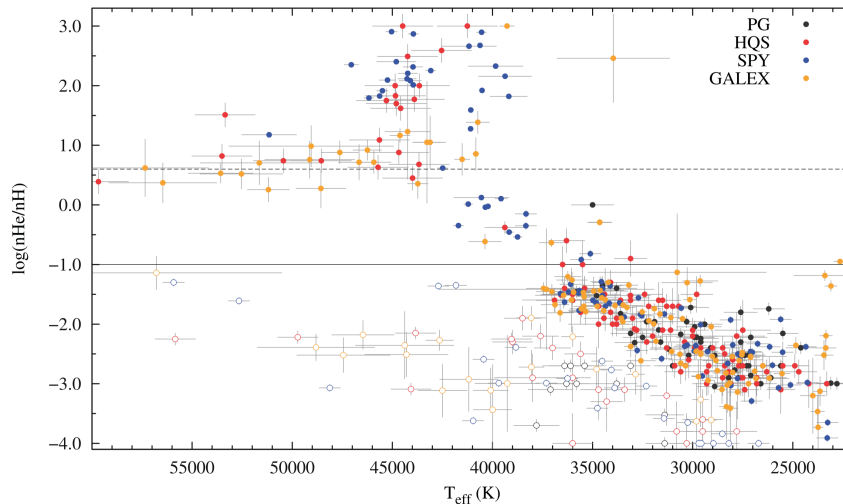
**Figure 2.** Distribution of hot subdwarfs in the $T_{\mathrm{eff}} - \log N_{\mathrm{He}}/N_{\mathrm{H}}$ plane. The color of the dots corresponds to measurements from different surveys. The minority groups of H-sdOs and lower He-sequence sdBs are marked with open dots. The PG survey only includes sdB stars. The individual surveys are described in Heber (2016). Taken from Heber (2016).

metal content is very different from the extreme He-sdOs, Naslim et al. (2013) suggested to distinguish intermediate H/He composition subdwarfs (iHe-sdOBs) with $\log N_{\mathrm{He}}/N_{\mathrm{H}} < 0.6$ as a separate class. Naslim et al. (2011) have discovered trans-iron elements, in particular zirconium and lead, to be strongly overabundant in the iHe-sdOB LS IV$-14°116$. Since then, three additional intermediate He-sdOBs have been found to be extremely enriched in heavy elements (Naslim et al. 2013; Jeffery et al. 2017b).

### 1.1.2    Formation and evolution

The formation of these heterogeneous classes of He-sdO/sdB stars is not yet understood well. They are believed to represent stages of several distinct post-RGB evolutionary paths. Since this work is focused on iHe-sdOB stars that are not known to be in binaries, we consider only those evolutionary scenarios that can produce single, He-rich subdwarfs. Two rivaling scenarios have been proposed to explain the hydrogen deficiency: a late He-flash (Castellani & Castellani 1993; Lanz et al. 2004; Miller Bertolami et al. 2008) or the merging of two helium white dwarfs (Webbink 1984; Zhang & Jeffery 2012).

**The hot flasher scenario**    If the hydrogen envelope of a star is removed at the tip of the RGB just before the He-flash would occur, it will evolve in a significantly different way than the canonical post-RGB evolution. Proposed mechanisms to strip the envelope in apparent single stars include stellar winds (Sweigart 1997) or even common envelope ejection due to interactions with a sub-stellar companion (Charpinet et al. 2011; Schaffenroth et al. 2014). When the hydrogen envelope is removed, the post-RGB star will first evolve to high temperatures and then follow the white dwarf cooling sequence. Depending on the mass of the remaining envelope, the He-flash can occur at different stages in this evolution. D'Cruz et al. (1996) have coined the term "hot flashers" for these scenarios.

Lanz et al. (2004) have identified three types of hot flasher evolution; evolutionary tracks for all cases are shown in Fig. 3. The main distinction between the three tracks is the extend to which the remaining hydrogen shell is mixed with the He-core. Different ignition times lead to different temperatures and surface compositions when the EHB is reached. All cases follow a similar pattern: after the initial He-flash, the stellar structure changes and the post-RGB star evolves toward lower luminosities and temperatures. As the He-burning luminosity rises, the surface luminosity rises again. Since the first He-flash occurs off-center (neutrino-cooling leads to lower

**Figure 3.** Theoretical HRD showing four hot flasher evolutionary tracks: Two early flasher cases (red), the shallow mixing case (yellow), and the deep mixing case (blue). Taken from Battich et al. (2018).
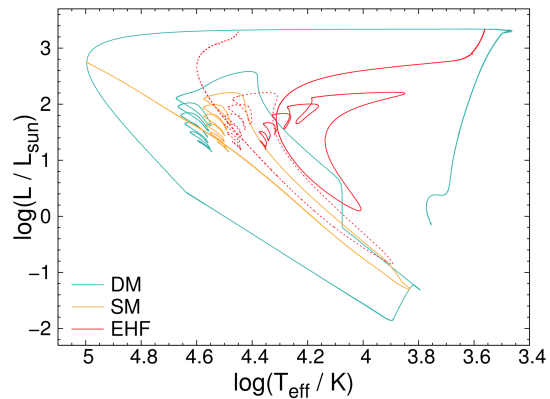
temperatures in the very center), the He-burning zone propagates inward, which leads to several subsequent flashes (loops in Fig. 3). The high luminosity of the initial He-flash drives a convection zone in the core. This convection would normally not effect the hydrogen envelope since they are separated by the hydrogen-burning shell. However, when the envelope is sufficiently thin at the time of the flash, the hydrogen-burning shell can no longer prevent mixing with the core. In the case of an *early hot flasher* during the phase of constant luminosity, no hydrogen is mixed in the core, which results in the creation of a hydrogen-rich sdB that shares the surface composition of its RGB progenitor. If the He-flash happens at the beginning of the cooling sequence, the hydrogen burning shell is thinner and some helium from the core is mixed to the surface (*shallow mixing*). This scenario can produce helium-rich sdOBs that are also enriched in carbon and nitrogen. *Deep mixing* of the hydrogen shell with the core happens as a consequence of an even later flash. When hydrogen is mixed in the hot, carbon-rich core, it is violently burned in a secondary flash that consumes most of the remaining envelope, which results in an extremely He-rich, carbon-enhanced sdO or sdB. Miller Bertolami et al. (2008) and Battich et al. (2018) have performed detailed evolutionary computations of all three cases. They find that all late hot flasher tracks result in carbon-rich surface abundances once the stars reach the EHB. However, it should be noted that the surface abundances of hot subdwarfs are not directly comparable to results from these calculations as they are strongly influenced by the effects of diffusion (discussed in Sect. 5.12.1). Still, even diffusion will not convert a carbon-rich atmosphere into a carbon-poor one. Therefore, the late flasher scenario can not explain the abundances observed in He-sdOs of the N-type (such as HD 127493 and HZ 44), while it is consistent with CN-rich He-sdOBs like Feige 46.

**White dwarf merger** The merging of two He-WDs naturally explains the lack of He-sdOs in binaries. Zhang & Jeffery (2012) have shown that the merging of two He-WDs can create He-sdOs of the N-type. Close binary systems lose orbital momentum due to the emission of gravitational waves. The resulting chemical composition of the surface depends on the mass transfer rate. If the mass transfer is sufficiently slow, material from the less massive (secondary) WD forms an accretion disc around the more massive (primary) WD. The temperatures in this disc are too low for nuclear fusion, so the resulting surface composition resembles that of the He-WD progenitors. Higher mass-loss rates lead to dynamically unstable transfer – the secondary WD is tidally disrupted and most of its mass is transfered instantly, forming a hot envelope around the primary WD. Modeling this rapid process is possible using hydrodynamic calculations, as performed by Dan et al. (2011) and Schwab et al. (2012).

Schwab (2018) has used the result of these calculations to continue the evolution of the merger product until it reaches the EHB as a He-rich, core He-burning subdwarf. Figure 4 shows the evolution of his $0.2\,M_\odot + 0.3\,M_\odot$ model and has particular phases in the evolution numbered. The merger product initially expands (between marks 2 and 3), before contracting as it radiates energy away (3 to 4). Eventually, He-fusion ignites off-center (4), similar to the hot flasher scenarios. The evolution from this stage to the EHB takes only about $10^6$ years, while the evolution on the EHB (not shown in Fig. 4) takes in the order of $10^8$ years. A comparison between the WD-merger mod-
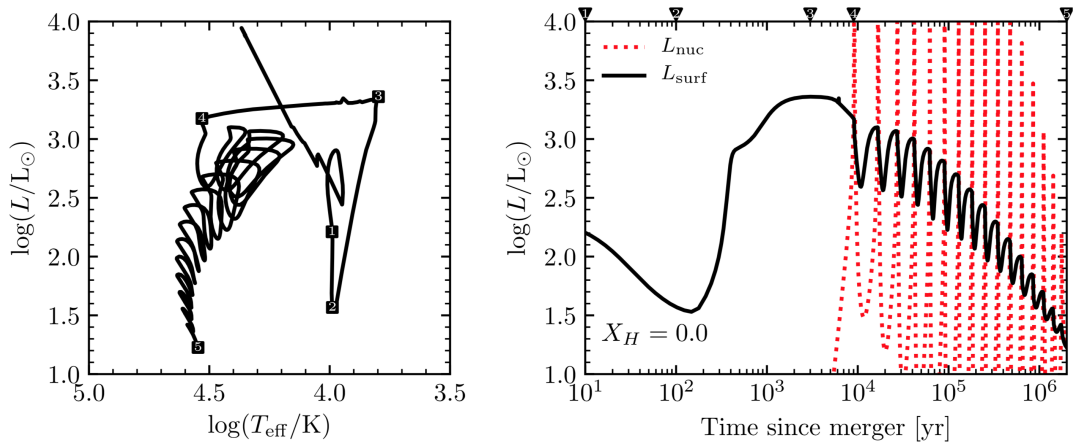
**Figure 4.** Double He-WD merger track from Schwab (2018). The left-hand panel shows the post-merger evolution in the HR diagram. The right-hand panel shows the nuclear (dashed red) and surface luminosity (black) from He-fusion as a function of time since the merging. Numbered squares in the HR diagram and triangles in the luminosity plot mark particular phases in the evolution.

els from Zhang & Jeffery (2012) and the observed population shows that He-sdOs do not cluster on the EHB, but are mostly distributed in the regions where secondary He-flashes are predicted. Schwab (2018) did not compute the abundance of metals at the surface. However, Zhang & Jeffery (2012) have shown that He-WD merger models can produce N-rich, C-poor He-sdOs when no processed material is mixed to the surface (slow, low-mass mergers with $M_{\text{final}} < 0.65 M_{\odot}$), but also C-, Ne-rich, N-poor surfaces when processed material is dredged up in the faster evolution that follows a higher-mass merger ($M_{\text{final}} > 0.65 M_{\odot}$). Therefore, merger scenarios are preferred over hot flasher models for N-type He-sdOs. Both hot flasher and mergers can produce C-type sdOBs. CN-type He-sdOBs are best explained with the hot flasher scenario (Zhang & Jeffery 2012).

The biggest problem with merger scenarios is that they predict rotational velocities $v_{\text{rot}} > 30 \, \text{km s}^{-1}$ (Schwab 2018), which is not observed in He-sdOs (Hirsch 2009; Geier & Heber 2012).

### 1.1.3 Nuclear synthesis

In the context of interpreting surface abundances in hot subdwarfs, it is important to consider the different processes of nuclear synthesis during stellar evolution. If material from the stellar interior is mixed to the surface, regardless of whether during a merger or simply by convection after the He-flash, the signature of these processes may be observable.

- Solar-mass and less massive stars on the main sequence generate most of their energy by fusing hydrogen to helium in the so-called p-p chain. There are three variants of this chain, the most important one being the PP-I chain:

$$p + p \rightarrow {}^2\text{H} + e^+ + \nu$$
$$^2\text{H} + p \rightarrow {}^3\text{He} + \gamma$$
$$^3\text{He} + {}^3\text{He} \rightarrow {}^4\text{He} + 2p$$
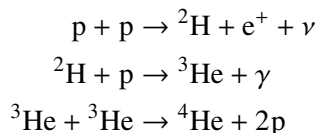
- The second important H-fusion process is the CNO-cycle, which is dominant at higher core temperatures ($T_{\text{core}} \gtrsim 1.7 \times 10^7 \, \text{K}$), hence in more massive stars ($M \gtrsim 1.3 M_{\odot}$, Schuler et al. 2009). It is especially interesting with respect to the observable surface metal composition as it changes the abundances of C, N, and O. The most important variant of the CNO-process is the CNO-I branch:

$$^{12}\text{C} + p \rightarrow {}^{13}\text{N} + \gamma, \qquad {}^{14}\text{N} + p \rightarrow {}^{15}\text{O} + \gamma$$
$$^{13}\text{N} \rightarrow {}^{13}\text{C} + e^+ + \nu, \qquad {}^{15}\text{O} \rightarrow {}^{15}\text{N} + e^+ + \nu$$
$$^{13}\text{C} + p \rightarrow {}^{14}\text{N} + \gamma, \qquad {}^{15}\text{N} + p \rightarrow {}^{12}\text{C} + {}^4\text{He}$$
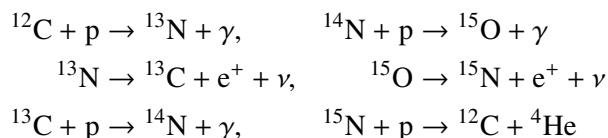
Since the timescales of these reactions are short compared to $^{14}N(p, \gamma)^{15}O$, this process leads to a high equilibrium abundance of nitrogen. This is why sub-solar C and O abundances and enriched N are often referred to as the CNO-cycle pattern.

- As discussed before, it is the circumstance in which helium fusion is ignited that distinguishes sdB stars from ordinary HB stars. After the initial He-flash, He is converted to C in the triple alpha process.

$$^4\text{He} + {}^4\text{He} \rightarrow {}^8\text{Be}$$
$$^4\text{He} + {}^8\text{Be} \rightarrow {}^{12}\text{C} + \gamma$$
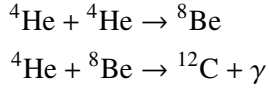
  This process is the main source of C in the universe since only extremely small amounts of C and no heavier elements were produced in the big bang.

- Temperatures high enough to continue the alpha process are not sustained in sdO/B progenitors due to their low mass. However, they might be reached for a short time during He-flashes.

$$^{12}\text{C} + {}^4\text{He} \rightarrow {}^{16}\text{O} + \gamma$$
$$^{16}\text{O} + {}^4\text{He} \rightarrow {}^{20}\text{Ne} + \gamma$$
$$\vdots$$
$$^{52}\text{Fe} + {}^4\text{He} \rightarrow {}^{56}\text{Ni} + \gamma$$
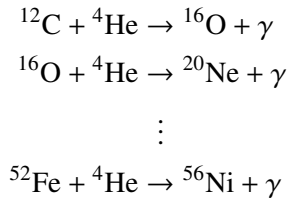
  It is highly unlikely that reactions beyond Ne production occur during He-flashes of low mass stars. These reactions are restricted to late stages in the evolution of high-mass stars ($M \gtrsim 10 M_\odot$). The alpha ladder ends at $^{56}$Ni since it is has the highest binding energy in the sequence.

- Heavier elements, such as those observed in the atmospheres of some intermediate He-sdOBs are created by different processes. One such process is the s-process, where neutrons are added to existing nuclei. If the new, heavier nucleus is unstable, it will $\beta^- -$decay, thereby converting a neutron to a proton, and increasing the atomic number before additional neutrons are added (in contrast to the r-process, where multiple neutrons are added before the nucleus decays). This process ends at $^{210}_{84}$Po, which $\alpha$-decays to $^{206}_{82}$Pb. The heaviest stable element created through the s-process is $^{209}_{83}$Bi. The creation of elements through the s-process requires a continuous source of neutrons. There are not many environments that can supply neutrons over the long timescales that are required to create substantial amounts of the heavier elements. In AGB stars, proposed sources of neutrons are processes that happen during a thermal pulse (Busso et al. 1999).

# 2 Stellar atmospheres and synthetic spectra

All our knowledge about stars is based on the analysis of their light. A sound understanding of the very thin layer at the stellar surface from which photons can escape (the stellar photosphere) is essential to connect models of the stellar interior with observations. A wealth of information about the stellar atmosphere is encoded in the spectrum of this light. The effective temperature $T_{\text{eff}}$, surface gravity $g$, as well as radial velocity $v_{\text{rad}}$ and projected rotational velocity $v \sin i$ can be determined directly from the observed spectrum. The basic stellar properties luminosity $L$, mass $M$, and radius $R$ can be obtained by combining the spectroscopic analysis with flux-calibrated observations (or photometry) and an independent measure of distance (for instance from parallax measurements provided by the *Gaia* satellite). However, to extract this information, one has to model the temperature and (electron) density stratification in the stellar atmosphere as well as the complex emergent radiation field.

To compute synthetic spectra that can be compared to observations, a model of the stellar atmosphere is required. Model atmospheres are typically calculated for a given set of effective temperature, surface gravity, and chemical composition (including hydrogen, helium, and metals). The synthetic spectra created from these models can therefore be used to derive these parameters directly. The output model atmosphere consists of the stratification of temperature, density, and occupation numbers for considered levels and ions in the atmosphere down to a depth where the atmosphere becomes opaque at all frequencies. The following section will give a short description of the solution to the basic stellar atmosphere problem. There are many sources that provide a more detailed description, for example the very detailed account by Werner & Dreizler (1999) and the textbook of Hubeny & Mihalas (2014).

To construct a model atmosphere that holds the specified boundary conditions at the surface, one has to model the interactions between photons, ions, and electrons as photons from the bottom of the stellar atmosphere are transferred toward the stellar surface. Stellar atmosphere programs make a number of approximations to iteratively determine the structure of the atmosphere. The first approximation is the assumption of *hydrostatic equilibrium* – gravitational and gas (and radiative) pressure are balanced. This assumption introduces the restriction that stellar winds can not be modeled.

It can further be assumed that every volume element in the atmosphere emits as much flux as it absorbs, and that the energy transport to the surface due to photons is dominating, while convective energy transport can be neglected (*radiative equilibrium*). The interaction of photons with electrons and ions influences the efficiency of the energy transport. Specifically the occupation density of individual levels determines how likely photon absorption or emission processes are. For instance, if the energy of a photon is close to the energy difference between two levels, it can be absorbed to excite a bound electron to a higher state. This leads to absorption lines at distinctive energies ($\leftrightarrow$ wavelengths) in the observed spectrum that depend on the atomic properties of the absorbing ion.

In deep layers of the atmosphere, where collisional processes between ions and electrons dominate over radiative processes, the populations of energy levels and ionization stages are coupled only to the density and temperature of the local plasma. In this case, one can assume the plasma to be in local thermal equilibrium (LTE) since the mean free path of photons (and therefore also electrons and ions) is very small compared to the distance over which the temperature changes.

- The particle velocity distribution is given by a Maxwell-Boltzmann distribution

$$p(v) = 4\pi \left( \frac{m}{2\pi k_\mathrm{B} T} \right)^{3/2} v^2 e^{-mv^2/2k_\mathrm{B}T}$$

  where $T$ is the local temperature, $k_B$ the Boltzmann constant, $v$ is the particle velocity, and $m$ is its mass.

- The ratio of populations of any two energy levels is given by the Boltzmann equation

$$\frac{n_i}{n_k} = \frac{g_i}{g_k} e^{-(E_i - E_k)/k_B T}$$

  where $n_i$ is the population of level $i$, $E_i$ its energy with respect to the ground state, and $g_i$ the statistical weight

$$g_i = 2 \cdot J_i + 1$$

  where $J_i$ is the total angular momentum quantum number. The population of a level $i$ relative to the total number density of its ionization stage $I$ is then given by:

$$\frac{N_i}{N_I} = \frac{g_i e^{-E_i/k_B T}}{\sum_k g_k e^{-E_k/k_B T}} = \frac{g_i e^{-E_i/k_B T}}{U_I}.$$

  Here, $U_I$ is called the partition function.

- The number ratio of atoms in two subsequent ionization stages is given by the Saha equation

$$\frac{N_{I+1}}{N_I} = \frac{2U_{I+1}}{n_e U_I} \left( \frac{2\pi m_e k_B T}{h^2} \right)^{3/2} e^{-\chi_I / k_B T}$$

where $h$ is the Planck constant, $m_e$ the electron mass, and $n_e$ the local electron density. This can be combined with the condition of charge conservation to obtain the ionization fractions for all atoms. Therefore, once the partition functions for all levels are known, the only additional atomic data needed are the ionization energies $\chi_I$.

The LTE approximation is valid for electrons in the stellar photosphere. However, the LTE approximation may no longer be sufficient for photons in the line-forming regions of hot stars such as those discussed here. The occupation numbers of atomic levels depend on the non-local radiation field since photons from deeper, hotter layers in the atmosphere are not immediately absorbed and interact with ions in higher, usually cooler layers. In this non-LTE case, the Saha and Boltzmann equations may no longer apply in the outer layers of the atmosphere. They have to be replaced by a balance of collisional and radiative processes: the so-called *statistical equilibrium* and its formulation through the rate equations. The final model atmosphere is a result of the simultaneous solution of the highly coupled and non-linear radiation transfer equations and the equations of hydrostatic, radiative, and statistical equilibrium.

In non-LTE, individual spectral lines are allowed to contribute not only to the total opacity, but also to the atomic level populations. Since the Boltzmann and Saha equations can no longer be used to compute these populations, detailed model ions are required. Figure 5 visualizes an example model ion, the Ge v ion used by Rauch et al. (2012) with the TMAP[1] model atmosphere code. The large number of transitions and mutual interaction between all included model ions considerably increases the required computation time.



**Figure 5.** Grotian diagram for the TMAP Ge v model ion from Rauch et al. (2012). Energy levels are ordered by their LS-coupling terms (*JJ*-coupling terms for the six levels in the center). The most important transitions are labeled with their wavelength in Å.

It is very useful to give individual level populations with respect to the LTE population densities, expressed as departure coefficients. The latter may be quite different for different levels. Hence, some levels may be close to LTE (departure coefficient $\approx 1$), while others may be over- or under-populated. The same holds for ionization stages. Usually, the departures from LTE are small for

---

[1]Tübingen NLTE Model-Atmosphere Package, http://astro.uni-tuebingen.de/~rauch/TMAP/TMAP.html

the dominant stage of ionization but they may be large for others.

As described above, the calculation of atmospheric structures is a non-linear and strongly coupled process. However, it is still instructive to qualitatively consider individual processes in the atmosphere and their effects on the observable stellar spectrum. Only the most important effects are listed in the following:

- Effective temperature $T_{\mathrm{eff}}$: Since the ionization equilibrium strongly depends on the temperature, the relative strength of He II to He I lines can be used to determine the temperature. This is also possible using the strength of metal lines from different ionization stages, if their abundance is known (or adjusted simultaneously).

- Surface gravity $g$: The surface gravity strongly influences the density and pressure in the stellar atmosphere. Since the broadening of hydrogen and He II lines is dominated by the linear Stark effect mainly due to free electrons, the extend of the wings of these strong spectral lines is an indicator of surface gravity. An increase in electron density also lowers the ionization potential of all atoms, so lines that originate from energy levels close to the ionization energy become weaker with higher surface gravity.

- Chemical composition: If the effective temperature and surface gravity are known, the strength of metal lines depends mostly on the chemical composition of the atmosphere.

- The radial velocity can simply be determined from the Doppler shift of spectral lines, preferably sharp metal lines.

- Projected rotational velocity $v \sin i$: If a star is rotating, one side of the star rotates toward the observer while the other side rotates away, which means that light from each side is blue- or red-shifted, respectively. Since stars appear as point sources to modern telescopes, only the average spectrum over the stellar disk is observed, so the line profiles are broadened. The projected rotational velocity $v \sin i$ can be measured, only, because the axis of rotation may be inclined at an angle $i$.

## 3   Computer codes

### 3.1   Model atmospheres with TLUSTY

The model atmospheres used in this work were computed using TLUSTY, a program for plane-parallel, horizontally homogeneous model stellar atmospheres in hydrostatic and radiative equilibrium. It was initially developed by Hubeny (1988) and has been constantly extended and updated in the last decades (e. g. Hubeny & Lanz 1995). Recently, a detailed three-part manual was published by Hubeny & Lanz (2017a,b,c).

TLUSTY is able to compute simple LTE model atmospheres that converge within minutes but also very complex NLTE metal line-blanketed atmospheres that take several hours to construct. LTE models that consider molecular opacity through opacity tables and convection in the mixing-length formalism can be used to model cool stars, in principle as late as spectral types K. However, TLUSTY's strong suit is the simultaneous treatment of a large number of metal line transitions in NLTE that makes it possible to accurately model the spectra of compact, hot stars. Only for the hottest, or low-surface gravity stars (e. g. CSPN and Wolf-Rayet stars) the stellar winds that become important are not considered in TLUSTY. The abundances of elements in the atmosphere are always assumed to be homogeneous – possible stratification due to diffusion effects is neglected. For each ion that is included in NLTE, a model atom has to be provided. This model atom contains information about energy levels, transition probabilities, and photoionization cross-sections. The large number of transitions in iron and nickel (about 6 million in the models used here) requires special treatment. TLUSTY uses the opacity sampling (OS) method in which the line opacity is sampled on a grid of frequency points for each element included.
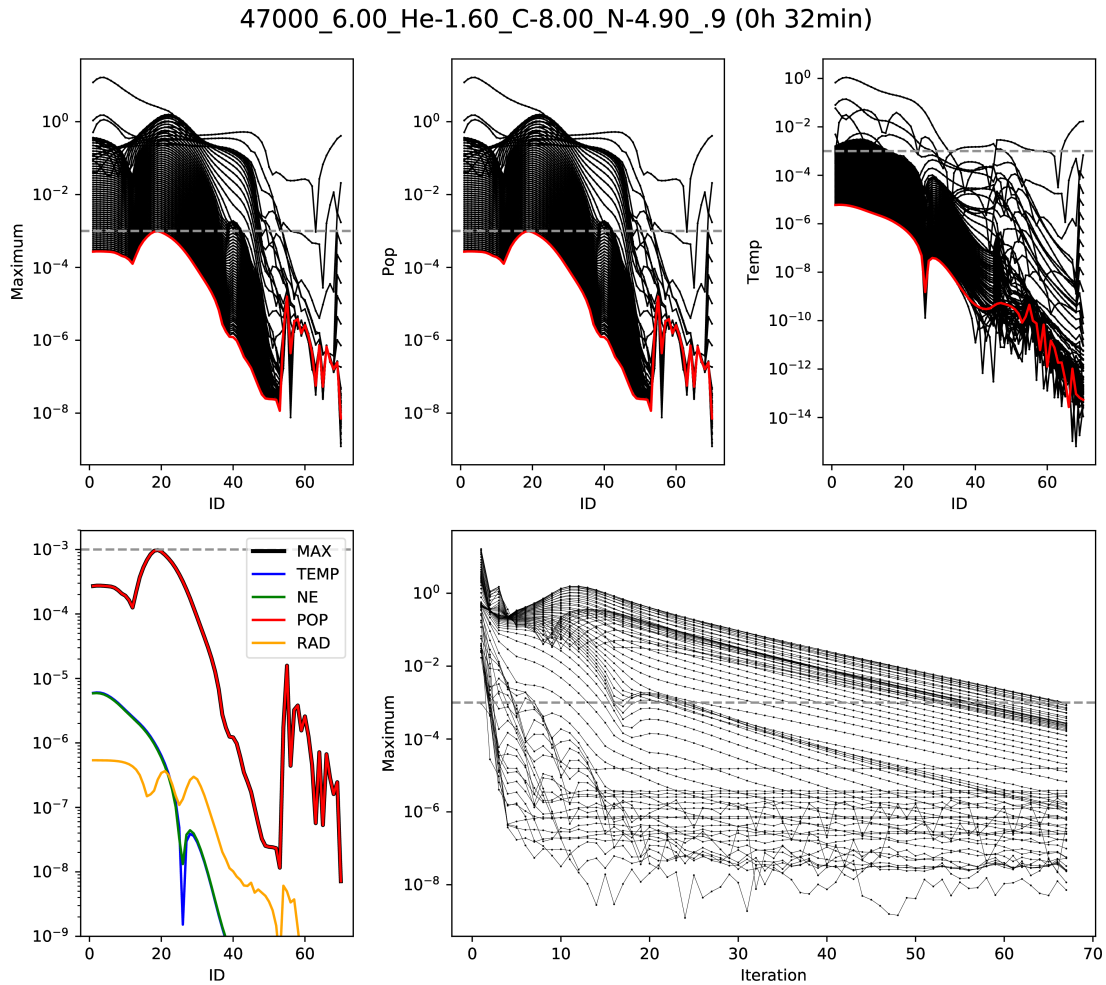
**Figure 6.** Example of a TLUSTY convergence plot. The top panels show from left to right: the maximum relative change, the change in population number, and the change in temperature per depth point with iteration number. The last iteration is highlighted in red. The left bottom panel shows the changes in temperature, electron density, population number, and mean radiation intensity for the last iteration. The maximum change for all depth points with progressing iterations is shown in the bottom right panel. In this particular case, the starting model was a HHe only model with $T_{eff}$ = 47000, $\log g$ = 6.0, and $\log N_{He}/N_H$ = $-1.6$ (appropriate for the H-sdO Feige 110), while the target model included additionally C and N in NLTE.

To construct a model atmosphere with new parameters, one usually starts with a model that includes only hydrogen and helium in NLTE. Then, additional elements are added in small steps to make sure that the model converges properly. Figure 6 shows the convergence of a HHeCN model that had a HHe model as its starting point. A model is considered converged when the relative changes in population numbers, temperature, electron density, and mean radiation intensity with respect to the last iteration are less than 0.1% for every depth point.

## 3.2  Synthetic spectra with SYNSPEC

SYNSPEC is part of the TLUSTY package and is used to create a detailed synthetic spectrum. Figure 7 shows the final synthetic spectral energy distributions (SEDs) in the FUV region for three of the stars discussed in this work: HD 127493, HZ 44, and Feige 46. All SEDs are convoluted with a Gaussian kernel with a FWHM of 4 Å for clarity. The most important features in this spectral range are the ionization edges of He I at 504 Å and H at 912 Å. Even at wavelengths shorter than the H ionization edge, the flux in all stars is at least one order of magnitude higher than at 4000 Å.
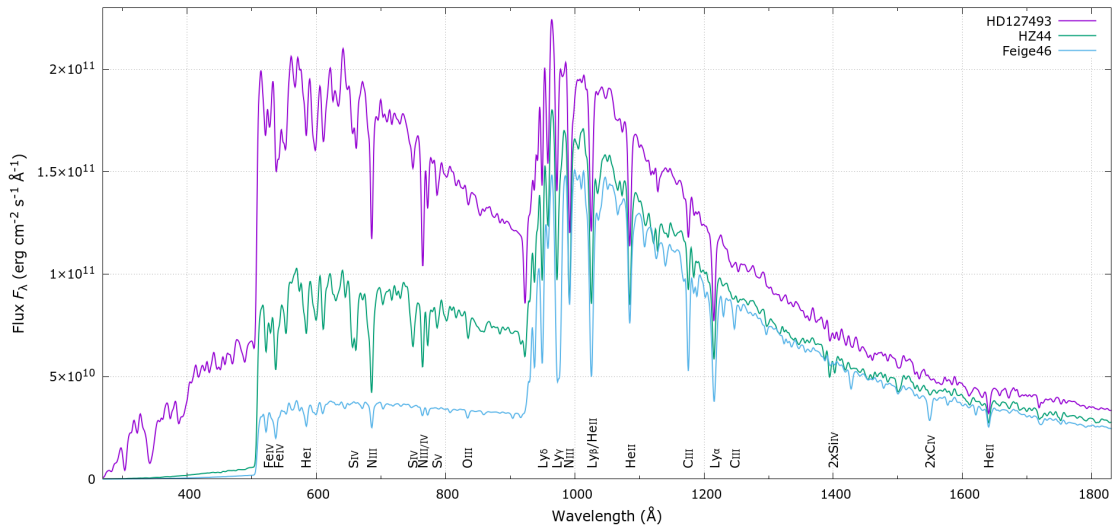
**Figure 7.** Synthetic spectra including line blanketing for HD 127493, HZ 44, and Feige 46 in the UV region. The spectra are convoluted with a 4 Å Gaussian for clarity. The difference in flux in the EUV region is due to the different temperatures of the stars. The two edges at 504 Å and 912 Å correspond to the ionization energies of He I and H, respectively. Some of the strongest lines are labeled. In Feige 46, the Ly γ line is blended with a very strong C III line.

In addition to the model atmosphere SYNSPEC requires the same model atoms and broadening tables as used by TLUSTY. It also requires a separate list of all metal lines that should be included in the final spectrum. This line list specifies transition wavelengths and oscillator strengths as well as the excitation energy and total angular momentum quantum number of the lower and upper levels. Strong lines are only well reproduced in the final spectrum if accurate Stark broadening coefficients are given. The line list used in this work includes about 1.3 million lines between 880 Å and 10 000 Å. Available atomic data (especially oscillator strengths but also accurate wavelengths) are scarce for lines from ionized, heavy elements. The atomic data collected for these ions will be described in Sect. 5.5.

All elements for which no model atoms are available can still be included using the LTE approximation. As discussed in Sect. 2, this requires the computation of partition functions. For ions with atomic number $Z < 30$ or ionization stages I-II, all necessary data to include a line in LTE are already implemented in SYNSPEC 51. Since the dominant ionization stages for most elements in the sdOB stars discussed here are the stages IV-V, additional atomic data had to be supplemented to include heavy elements such as Ge, As, Zr, or Pb. Table 1 lists the number of levels considered for each ion and their respective ionization energy $\chi_I$. We use the non-standard PFSPEC subroutine in SYNSPEC to compute partition fractions for these ions as it was already implemented and used for C VI, N VI-VII, and O VI-VIII. It generalizes the Boltzmann equation above to include the possibility of *dissolved* levels. In high electron densities, the additional electric field perturbs the potential of the atomic nucleus and lowers the ionization potential by a temperature- and density-dependent amount. Energy levels that lie above this lowered ionization energy do not exist anymore – they are dissolved. In reality, energy levels close to the lowered ionization energy have a certain probability to be dissolved. A similar effect also leads to lower ionization energies: the electrical attraction between the nucleus and any bound electron is reduced by the influence of other bound electrons (*electron shielding*). This effect can be accounted for approximately by replacing the nuclear charge $Z$ with an effective nuclear charge $Z^*$:

$$Z_i^* = Z - s_i$$

where $s_i$ is the screening number of level $i$. Finally, the partition function is computed in the following way:

$$P = 14.69 - 0.20 - 2/3 \cdot \log n_e$$

$$w_i = \begin{cases} P + 4 \cdot \log Z_i^* - 4 \cdot \log i & Z^* > 0 \\ 0 & Z^* \leq 0 \\ 1 & w_i > 1 \end{cases}$$

$$U_i = g_i \cdot w_i \cdot \exp(-E_i/k_B T)$$

$$U_I = \sum_i U_i$$

where $w_i$ is the occupation probability ($1 - w_i$ is the probability that the level is dissolved and lies in the continuum). As it turned out, $w_i$ is always equal to one using the treatment presented here for ions in the considered stars, effectively reducing this method to the traditional Boltzmann equation. This is why we chose to disregard the screening numbers after initial testing by setting $s_i = 1$ for all added ions and levels.

**Table 1.** Number of new levels per ion added to Synspec and their ionization potential.

| Ion | $N_{levels}$ | $\chi_I$ (eV) | Source | Ion | $N_{levels}$ | $\chi_I$ (eV) | Source | Ion | $N_{levels}$ | $\chi_I$ (eV) | Source |
|---|---|---|---|---|---|---|---|---|---|---|---|
| Ga IV | 191 | 63.24 | 1 | Zr IV | 34 | 34.42 | 1 | Te VII | 59 | 124.20 | 1 |
| Ga V | 91 | 86.01 | 1 | Zr V | 101 | 80.35 | 1 | Te VIII | 1 | 143.00 | 1 |
| Ga VI | 157 | 112.70 | 1 | Zr VI | 96 | 96.38 | 1 | Xe IV | 94 | 45.00 | 1 |
| Ga VII | 180 | 140.80 | 1 | Zr VII | 1 | 112.00 | 1 | Xe V | 53 | 54.14 | 1 |
| Ge IV | 39 | 45.72 | 1 | Zr VIII | 1 | 133.70 | 1 | Xe VI | 72 | 66.70 | 1 |
| Ge V | 101 | 90.50 | 1 | Mo IV | 80 | 40.33 | 1 | Xe VII | 67 | 91.60 | 1 |
| Ge VI | 104 | 115.90 | 1 | Mo V | 257 | 54.42 | 1 | Ba IV | 31 | 47.00 | 1 |
| Ge VII | 167 | 144.90 | 1 | Mo VI | 112 | 68.83 | 1 | Ba V | 51 | 58.00 | 1 |
| Ge VIII | 1 | 176.40 | 1 | Mo VII | 95 | 125.64 | 1 | Ba VI | 49 | 71.00 | 1 |
| As IV | 33 | 50.15 | 1 | Mo VIII | 76 | 143.60 | 1 | Tl IV | 43 | 50.72 | 1 |
| As V | 8 | 62.77 | 1 | In IV | 17 | 55.45 | 1 | Tl V | 1 | 62.60 | 1 |
| As VI | 43 | 121.19 | 1 | In V | 32 | 69.30 | 1 | Tl VI | 1 | 80.00 | 1 |
| As VII | 49 | 147.00 | 1 | In VI | 1 | 90.00 | 1 | Pb IV | 102 | 42.33 | 1 |
| Se IV | 28 | 42.95 | 1 | Sn IV | 20 | 40.74 | 1 | Pb V | 44 | 69.00 | 1 |
| Se V | 14 | 68.30 | 1 | Sn V | 24 | 77.03 | 1 | Pb VI | 1 | 82.90 | 1 |
| Kr IV | 78 | 50.85 | 1 | Sn VI | 29 | 94.00 | 1 | Bi IV | 37 | 45.32 | 1 |
| Kr V | 42 | 64.69 | 1 | Sb IV | 28 | 44.20 | 1 | Bi V | 14 | 56.00 | 1 |
| Sr IV | 254 | 56.28 | 1 | Sb V | 8 | 55.70 | 1 | Bi VI | 114 | 88.00 | 1 |
| Sr V | 143 | 70.70 | 1 | Sb VI | 59 | 99.51 | 1 | Th IV | 24 | 28.65 | 2 |
| Sr VI | 21 | 88.00 | 1 | Sb VII | 1 | 117.00 | 1 | Th V | 1 | 58.00 | 1 |
| Y IV | 129 | 60.61 | 1 | Te IV | 15 | 37.40 | 1 | Th VI | 1 | 69.10 | 1 |
| Y V | 113 | 75.35 | 1 | Te V | 44 | 58.70 | 1 | Th VII | 1 | 82.00 | 1 |
| Y VI | 1 | 91.39 | 1 | Te VI | 8 | 69.10 | 1 | | | | |

**Notes.** References: (1) NIST[2], (2) http://web2.lac.u-psud.fr/lac/Database/Tab-energy/

## 3.3   Computation of atmospheric model grids

We constructed three new model grids that are tailored to fit the atmospheric abundances of DA white dwarfs (no helium), DAO white dwarfs (some helium), and He-sdOs. A summary of the grid parameters is shown in Table 2.

---

[2]National Institute of Standards and Technology, https://physics.nist.gov/PhysRefData/ASD/lines_form.html

**Table 2.** Newly constructed model grids used for determining atmospheric parameters.

| Grid | Elements | $T_{\mathrm{eff}}$ (K) min. | max. | step | $\log g$ (cgs) min. | max. | step | $\log N_{\mathrm{He}}/N_{\mathrm{H}}$ min. | max. | step | $N_{\mathrm{models}}$ |
|---|---|---|---|---|---|---|---|---|---|---|---|
| DAO | HHeCNO[a] | 40 000 | 100 000 | 4000 | 6.00 | 8.00 | 0.2 | −3.6 | −0.8 | 0.2 | 2640 |
| DA | HHeCNO[b] | 36 000 | 100 000 | 4000 | 6.00 | 8.80 | 0.2 | −6.0 | −4.0 | 1.0 | 765 |
| He-sdO | HHeCNSi[c] | 35 000 | 48 000 | 1000 | 4.70 | 6.00 | 0.1 | −1.0 | +2.1 | 0.1 | 6272 |

**Notes.** [a] based on the metal abundance pattern of WD 1214+267 from Good et al. (2005). [b] based on the metal abundance pattern of G191–B2B from Rauch et al. (2013). [c] based on the metal abundance pattern of HD 127493 from Dorsch et al. (2018).

The initial goal of this project was to study DA(O) white dwarfs, in particular their metal abundances and the so-called Balmer line problem. The Balmer line problem refers to the inability to model all Balmer lines simultaneously with consistent atmospheric parameters at temperatures exceeding $T_{\mathrm{eff}}$ = 50 000 K (Napiwotzki 1992). Werner (1996) showed that this problem can be solved for the hot sdO BD +28° 4211 and the DAO LS V +46° 21 by using detailed NLTE model atoms for C, N, and O, and including Stark broadening. Barstow et al. (2001) and Barstow et al. (2003) found a related problem for DA(O) white dwarfs – the effective temperatures determined from Balmer lines differed significantly from the temperature derived from Lyman lines (the so-called Lyman/Balmer line problem). In their analysis of DA(O) stars, Gianninas et al. (2010) have shown that the Balmer line problem in DAOs is linked to the presence of metal lines in the spectrum, as metal-rich stars are more likely affected. Preval et al. (2015) showed that this discrepancy could be improved significantly by not only including metals up to Ni, but also using the improved Stark broadening tables for hydrogen lines by Tremblay & Bergeron (2009). Latour et al. (2015) showed for BD +28° 4211 that there are still considerable differences between high signal-to-noise (S/N) optical spectra and NLTE models that use Stark broadening for C, N, O and also include Mg, Si, S, Fe, and Ni in NLTE. However, they could finally eliminate these discrepancies by adopting ten times solar abundances for C, N, O, and Fe as a fudge factor.

In the end, the idea of testing this approach for DA(O) stars in this work was abandoned in favor of a more detailed metal abundance analysis of HZ 44 and HD 127493, in part due to the lack of good archival data for DA(O) stars that have not yet been studied extensively. Still, the two DA(O) grids listed in Table 2 can in principle be used as a basis to construct accurate models for these stars using the method of Latour et al. (2015).

Since all three grids were initially based on an older version of the He-sdO grid, they were constructed using the older Tlusty 200 / Synspec 49 versions – the most recent versions are Tlusty 205 and Synspec 51.

A proper treatment of hydrogen line broadening, both in the calculation of the atmospheric structure as well as in the final spectrum synthesis, is essential for determining reliable atmospheric parameters from the Balmer lines. Our grids of Tlusty models use approximate Stark broadening after Hubeny et al. (1994), while the final spectra were created using the detailed Lemke (1997) hydrogen line broadening tables based on the unified theory of Stark broadening from Vidal, Cooper & Smith (1970, VCS).

For the He-sdO/Bs discussed in this work, broadening tables for helium lines are of special importance. Our newly constructed atmospheric grids use the broadening tables by Shamey (1969) for He I $\lambda\lambda$ 4026.189, 4387.930, and 4921.930 Å and results from Barnard et al. (1974) for He I 4471.500 Å. We do not use the treatment of Dimitrijevic & Sahal-Brechot (1984) (available for He I $\lambda\lambda$ 3819.60, 3867.50, 3871.79, 3888.65, 3926.53, 3964.73, 4009.27, 4120.80, 4120.80, 4168.97, 4437.55, 4471.50, 4713.20, 4921.93, 5015.68, 5047.74, 5875.70, 6678.15, 4026.20, and 4387.93 Å). Line profiles for these lines, if not included in the Shamey (1969) or Barnard et al. (1974) tables, are given by a Voigt profile with approximate Stark broadening. He II line broadening is considered using the Schoening & Butler (1989) tables, including He II $\lambda\lambda$ 1640, 4686,

3204, 2734, 2512, 2386, 10125, 6561, 5412, 4860, 4542, 4339, 4200, and 4101 Å. Future improvements to our models should include additional and updated helium line profiles.

The newly computed model grids can be used to visualize some of the effects discussed in Sect. 2. This includes for example the temperature-dependence of the He I-II ionization equilibrium. Figure 8 shows the He ionization fractions for models with varying effective temperatures from the HeCNSi grid. It is interesting to realize that the abundance of both He I and He II decreases continuously from 35 000 K to 48 000 K, while the abundance of the completely ionized He III increases.
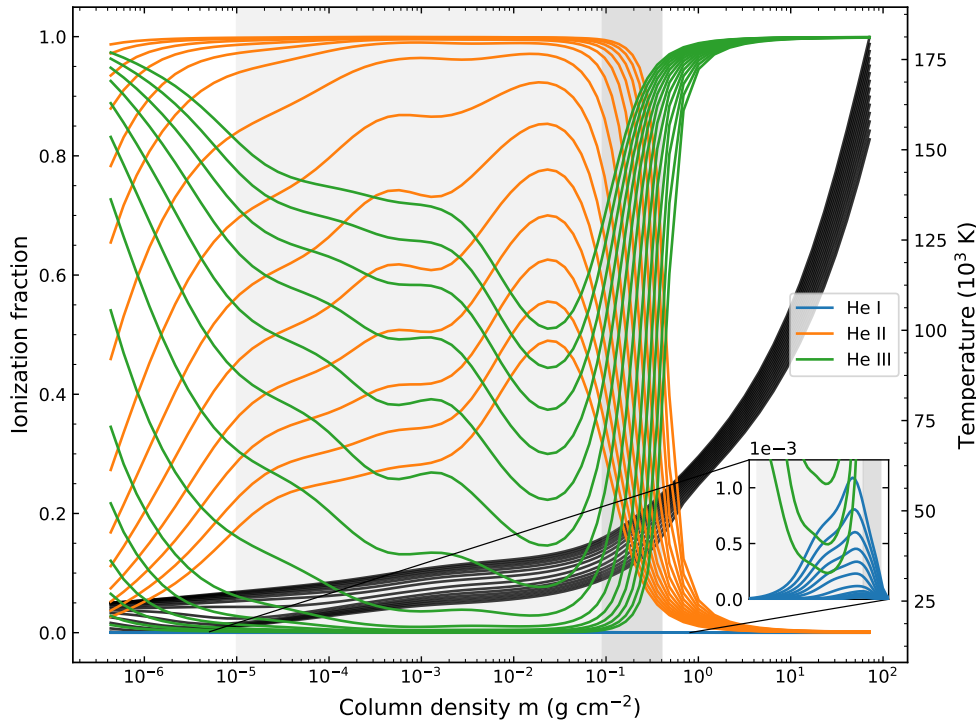


**Figure 8.** Ionization fractions for helium in model atmospheres from the HeCNSi grid, with effective temperatures from 35 000 to 48 000 K in steps of 1000 K. All models have $\log g = 5.6$ and $\log N_{\mathrm{He}}/N_{\mathrm{H}} = 0.6$, as well as the same metal abundances. The black curves show the temperature stratification. The dark grey area marks the continuum forming region, the lighter grey area marks the range where the strongest lines in the UV are formed. The inset shows the population of He I.

However, Fig. 9 shows that the strength of the strongest optical He II line, He II 4686 Å, does in fact increase from 35 000 K and reaches its maximum line strength at 45 000 K before it slowly weakens again. Also, decreasing the abundance of helium (between $\log N_{\mathrm{He}}/N_{\mathrm{H}} = +2.1$ and $-1.0$) in models with $T_{\mathrm{eff}} = 39\,000$ K and $\log g = 5.6$ actually increases the strength of optical He II lines. This can be explained by inspecting the population numbers of the involved energy levels: optical He II lines originate from transitions between relatively high-lying levels (He II 4686 Å with a 3s lower level at 48.37 eV, other optical lines involve the 4s lower level at 51.01 eV). These levels are only populated at sufficiently high temperatures and since the temperature in the line-forming region increases with lower He abundances, the strength of these lines increases as well. Since the temperature in the line-forming region increases with lower He abundances, the strength of these lines increases as well. The same is not the case for He I lines: here the abundance, even at 35 000 K, is much lower (see inset in Fig. 8) and the optical lines originate from lower levels (e.g. He I 4713 Å originates from a 2p transition at 20.96 eV), so their strength decreases with temperature.
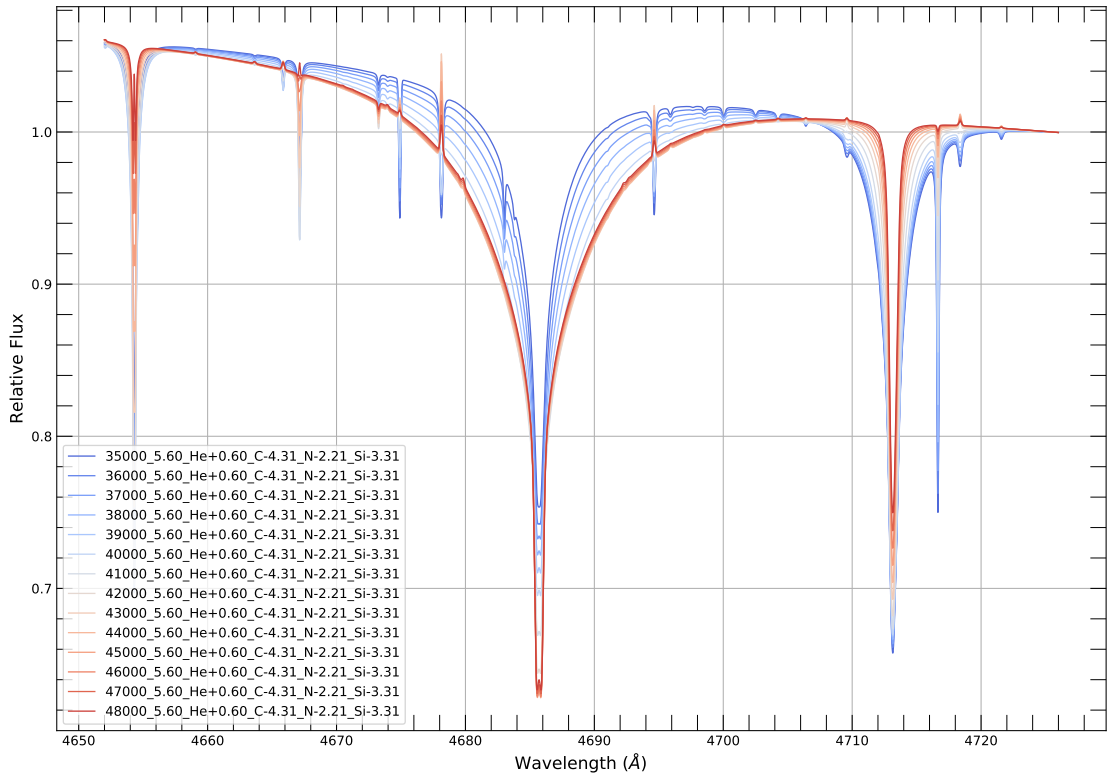
**Figure 9.** He II 4686 Å and He I 4713Å in synthetic spectra from the HeCNSi grid, with effective temperatures from 35 000 to 48 000 K in steps of 1000 K, colored from blue (cooler) to red (hotter). All models have $\log g = 5.6$, $\log N_\mathrm{He}/N_\mathrm{H} = 0.6$, and the same metal abundances. All spectra are normalized to their flux levels at 4725 Å.

## 3.4   $\chi^2$ **minimization using** SPAS

The synthetic grids created with SYNSPEC were fitted to observations using the $\chi^2$ minimization program SPAS (**S**pectrum **P**lotting and **A**nalysing **S**uite) developed by Hirsch (2009). This program can be used for spline interpolation in a three-dimensional grid of synthetic spectra, for example in $T_\mathrm{eff}$, $\log g$, and $\log N_\mathrm{X}/N_\mathrm{H}$ (where $X$ is the varied element). The program compares interpolated spectra to the observed spectrum and automatically tries to find the best combination of parameters using the downhill simplex method. Two methods of error estimation are available. The bootstrapping method tries to estimate the uncertainties by randomly removing data points, redoing the fit, and then computing the standard deviation of fit results. The resulting error estimates seem not to be very reliable since they strongly depend on the sampling of data points and usually underestimate the errors. Bootstrapping is only used for the determination of atmospheric parameters. When fitting metal lines to determine abundances, it is more meaningful to compute the standard deviation between single line fits. In the following, abundances of elements will usually be determined from a simultaneous fit of all considered lines, while the uncertainties are given as standard deviations of single line abundances.

## 4   The white dwarfs G191–B2B & RE 0503−289

The fact that some white dwarfs have been studied in detail before and have excellent data available makes them ideal targets for testing our method to determine the abundance of heavy metals. Two white dwarfs, the DA G191–B2B and the DO RE 0503−289 have been studied in detail by Rauch et al. (2017b) and Werner et al. (2018), especially as part of their "Stellar laboratories" series. While G191–B2B is metal-poor, the extraordinary quality of the UV data, including FUSE and STIS high-resolution spectra, reveals even weak lines. The helium-rich RE 0503−289 shows one of the most extreme enhancements in heavy metals in any hot star known. It should be noted

that it is not our goal to match the accuracy achieved by TMAP models for hot WDs that include heavy elements in NLTE. Instead, we aim to reliably model the strongest lines of the most abundant moderately ionized heavy elements in the significantly cooler intermediate He-sdOBs. Since ionization stages IV-VI can be seen in both types of stars, a comparison is possible, nevertheless.

To this end, we have constructed non-LTE models of G191–B2B and RE 0503–289. Their parameters are listed in Table 3. In the following, abundances relative to hydrogen will be referred to by using the abbreviation [X/H] = log $N_X/N_H$, where X is an element other than H and $N_X$ is the number density of particles of type X in the stellar atmosphere.

For G191–B2B, we restrict ourself to a few lines in the best-quality UV spectra, namely STIS E140H spectra ($R = 114\,000$) taken with the Hubble Space Telescope (HST) and MDRS spectra ($R \approx 19\,000$) from the FUSE satellite. The Ge IV line profiles produced by our models (see Fig. 10) agree reasonably well with the STIS spectrum at the abundance determined by Rauch et al. (2012), [Ge/H] = −7.35. This indicates that deviations from LTE are small for Ge IV transitions in the line-forming region of G191–B2B.
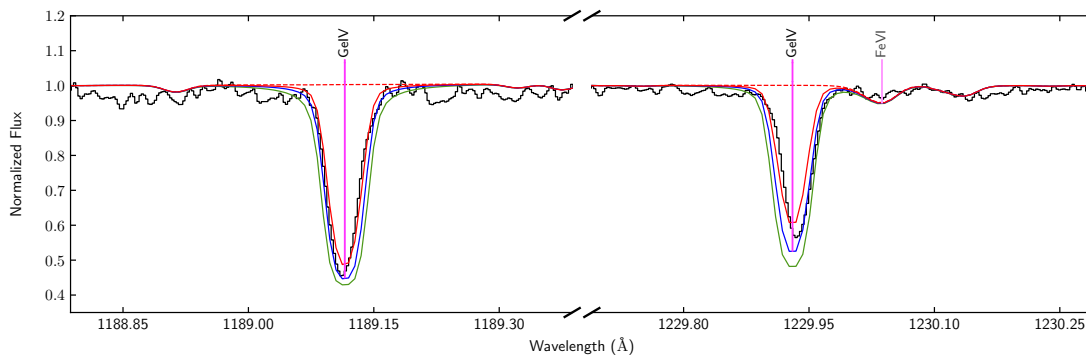


**Figure 10.** The Ge IV $\lambda\lambda$ 1189.028, 1229.840 Å resonance lines in the STIS spectrum of G191–B2B. The blue model has an abundance of [Ge/H] = −7.35, while the red and green models have abundances 0.3 dex lower and higher, respectively. The dashed red model is without Ge.

For Te VI and Mo VI lines in the FUSE spectrum of RE 0503−289, deviations from the reference abundances determined by Rauch et al. (2017b) and Rauch et al. (2016a) become larger. As shown in Fig. 11, both Te VI and Mo VI lines are too strong in our models if the reference abundances are adopted ([Te/H] = −2.23, [Mo/H] = −2.23). This may result from strong departures from the LTE approximation due to high temperatures in the atmosphere. However, Ge V lines in RE 0503−289, such as Ge V 1038.4 Å, fit well at the abundance determined by Rauch et al. (2012).
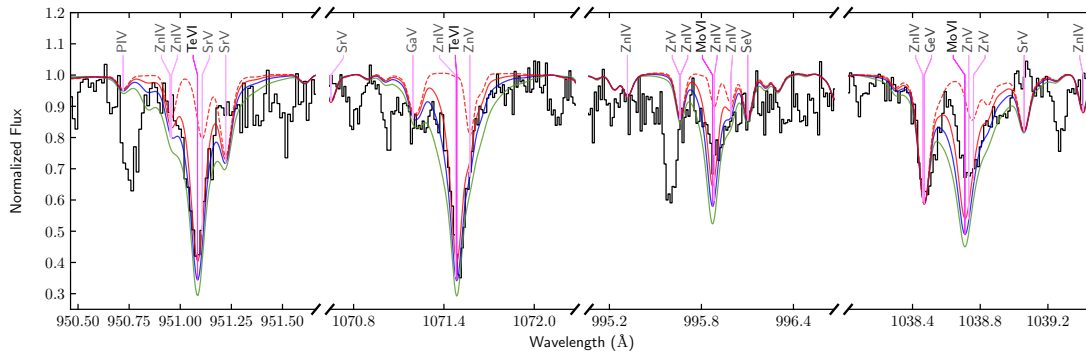


**Figure 11.** The strongest Te VI and Mo VI lines in the FUSE spectrum of RE 0503−289. The blue model has abundances of [Te/H] = −2.23, [Mo/H] = −2.23 while the red and green models have abundances 0.4 dex lower and higher, respectively. The dashed red model excludes Te and Mo.

We conclude that, while deviations from TMAP non-LTE results can exceed 0.4 dex for some ions

in hot WD stars, systematic errors are expected to be smaller for the cooler intermediate He-sdOBs that will be discussed in Chapter 5.

**Table 3.** Tlusty model parameters for G191–B2B[a] and RE 0503−289[b] .

| | Abundance ($\log N_X/N_H$) | | | | Abundance ($\log N_X/N_H$) | | |
|---|---|---|---|---|---|---|---|
| Element | G191–B2B | RE 0503−289 | NLTE ions | Element | G191–B2B | RE 0503−289 | NLTE ions |
| He | −5.31 | +2.86 | I-II | Ge | −7.35 | −2.19 | – |
| C | −6.28 | +0.74 | III-IV | As | −8.30 | −3.19 | – |
| N | −6.83 | −1.93 | III-V | Se | – | −1.22 | – |
| O | −5.92 | −0.26 | III-VI | Kr | −7.89 | −2.74 | – |
| Al | −6.38 | – | III | Sr | – | −1.65 | – |
| Si | −5.72 | −1.77 | III-IV | Zr | – | −2.00 | – |
| P | −7.30 | −3.99 | IV-V | Mo | −8.25 | −2.23 | – |
| S | −6.75 | −2.43 | III-VI | Sn | −8.53 | −2.29 | – |
| Fe | −4.93 | −3.16 | III-VI | Sb | – | −2.91 | – |
| Ni | −6.18 | −2.43 | IV-V | Te | – | −2.23 | – |
| Zn | −7.27 | −2.29 | – | Xe | −8.90 | −2.52 | – |
| Ga | −7.43 | −2.83 | – | Ba | −7.54 | −2.11 | – |

**Notes.** [a] $T_{\rm eff}$ = 60 000 K, $\log g$ = 7.6, abundances from Rauch et al. (2016a) and references therein, converted to [X/H] . [b] $T_{\rm eff}$ = 70 000 K, $\log g$ = 7.5, abundances from Rauch et al. (2017b); Werner et al. (2018) and references therein, converted to [X/H].

# 5  Analysis: HZ 44 & HD 127493

The text of this chapter is largely taken from a draft paper by Dorsch, Latour, and Heber (2019, to be submitted to A&A). Mayor contributions of the co-authors were limited to Sections 5.1 to 5.4 and 5.12 to 5.13.

## 5.1  HZ 44 & HD 127493

HZ 44 and HD 127493 were among the first sdOs that had been identified in the 1950s. HZ 44 was discovered in the first survey for faint blue stars in the halo by Humason & Zwicky (1947). The first spectral analysis of the helium line spectrum of HZ 44 was published in the pioneering paper of Münch (1958). From a curve of growth analysis Peterson (1970) derived metal abundances for the first time, but we know of no contemporary study.

HZ 44 is a spectrophotometric standard star (Massey et al. 1988; Oke 1990; Landolt & Uomoto 2007a), used for the calibration of the HST (Bohlin et al. 1990; Bohlin 1996; Bohlin et al. 2001), as well as that of *Gaia* (Marinoni et al. 2016), and therefore has frequently been observed. High resolution spectra are available from the far-UV to the red in the FUSE, IUE, and HIRES@Keck data archives.

HD 127493 has been used as secondary spectrophotometric standard star (Spencer Jones 1985; Kilkenny et al. 1998; Bessell 1999). Therefore, very accurate photometry is available but spectroscopic observations are scarce. Starting with the curve of growth analyses of Peterson (1970) and Tomley (1970) abundances of C, N, O, Ne, Mg, and Si were derived. The first NLTE model atmospheres were calculated by Kudritzki (1976), who revised the atmospheric parameters. Abundances of carbon (Gruschinske et al. 1980) and C, N, O and Si (Simon et al. 1980) were derived from equivalent widths of ultraviolet lines. A NLTE analyis of optical spectra allowed Bauer & Husfeld (1995) to determine the abundances of C, N, O, Ne, Mg, Al, and Si. The most recent NLTE analysis by Hirsch (2009) revised the atmospheric parameters and determined C and

N abundances from optical spectra. Hence, our knowledge of the chemical composition is rather limited. The abundance analysis performed in this chapter is based on, revises, and extends results from Dorsch et al. (2018).

## 5.2   Spectroscopic observations

For both stars excellent archival data are available in both the optical and UV ranges. An overview of the spectra we collected and used is given in Table 4, with additional details on the individual observations listed in Table 11 in the appendix.

**Table 4.** Spectra used for the analysis of HZ 44 and HD 127493.[a]

| Star | Instrument | Range (Å) | R | S/N |
|------|-----------|-----------|-----|------|
| HD 127493 | IUE SWP | 1150 − 1970 | 10 000 | 14 |
| | GHRS | 1225 − 1745 | 0.07 Å[b] | 40 |
| | IUE LWR | 1850 − 3273 | 10 000 | 14* |
| | FEROS | 3700 − 9200 | 48 000 | 180* |
| HZ 44 | FUSE | 905 − 1188 | 19 000 | 30 |
| | IUE SWP | 1150 − 1970 | 10 000 | 10 |
| | HIRES | 3022 − 7580 | 36 000 | 142* |
| | ISIS | 3700 − 5260 | 1.5 Å[b] | 170* |

**Notes.** [a] The signal-to-noise ratio is the average over the spectrum. [b] The resolution for long-slit spectrographs is given instead as $\Delta\lambda$. [*] Determined using numerical methods.

We used optical FEROS spectra to determine the atmospheric parameters of HD 127493 and measure photospheric metal abundances. FEROS is an echelle spectrograph mounted at the MPG/ESO-2.20m telescope operated by the European Southern Observatory (ESO) in La Silla. It features a high resolving power of R ≈ 48000 (Kaufer et al. 1999) and its usable spectral range, from ∼3700 Å to ∼9200 Å, includes all the Balmer lines as well as many He I, He II, and metal lines. The three available spectra of HD 127493 were co-added to achieve a high signal-to-noise ratio (S/N) of ≳ 100 in the 4000 − 6000 Å range. The S/N decreases drastically towards both ends of the spectral range and especially below 3800 Å.

Both stars have been observed with the International Ultraviolet Explorer (IUE) satellite with the short-wavelength prime (SWP) camera. We retrieved three archival INES[3] spectra for HD 127493, and two for HZ 44. The individual spectra were co-added for each star spectra to increase the S/N. They continuously cover the 1150 − 1980 Å range with a resolution of R ∼ 10000. Additional IUE spectra taken with the LWR camera (covering the 1850 − 3350 Å range) are also available for both stars. However, these spectra have a lower quality and the S/N drops sharply at both ends of the spectra. Fewer lines are observed in this wavelength range but the IUE LWR spectrum of HD 127493 has nevertheless been useful for the abundance analysis.

HD 127493 has also been observed with the Goddard High-Resolution Spectrograph (GHRS) mounted on the Hubble Space Telescope (HST). These spectra are publicly available in the MAST[4] archive and cover the 1225 Å − 1745 Å range with a resolution of about 0.07 Å. The final spectrum is a combination of ten observations spanning 35 Å each and lacks coverage in the following regions: 1450.5 Å − 1532.5 Å, 1567.7 Å − 1623.2 Å, and 1658.1 Å − 1713.0 Å. Since the wavelength calibration was not perfect, we cross-correlated the individual spectra to match the synthetic spectrum of HD 127493. In addition, they were shifted to match the flux level of the IUE spectra.

HZ 44 has been observed with the Far Ultraviolet Spectroscopic Explorer (FUSE) satellite that

---

[3]IUE Newly-Extracted Spectra, http://sdc.cab.inta-csic.es/ines/index2.html
[4]Mikulski Archive for Space Telescopes, https://archive.stsci.edu/index.html

covers the spectral range between 905 Å and 1188 Å. We retrieved three calibrated observations from MAST, two taken through the LWRS (30" × 30") aperture, and one through the MDRS (4" × 20") aperture. We co-added all spectra from the eight segments in each observation. After inspection it turned out that the MDRS spectrum had a better quality and a better wavelength calibration, so we relied on this spectrum for our analysis. A large number of strong metal lines lie in the spectral region covered by FUSE, including lines from trans-iron elements, many of which have not yet been identified.

To determine the atmospheric parameters of HZ 44 we used a low resolution, high S/N spectrum taken with the Intermediate dispersion Spectrograph and Imaging System (ISIS) mounted at the Cassegrain focus of the 4.2m William Herschel Telescope on La Palma.

The spectra of HZ 44 taken with the HIRES echelle spectrograph mounted at the Keck I telescope on Mauna Kea were most valuable for our abundance analysis. A total of 68 extracted HIRES spectra of HZ 44 from several programs covering various wavelength ranges are available in the Keck Observatory Archive (KOA[5]). We co-added the spectra of four high S/N HIRES observations to produce the spectrum used for our abundance analysis. To access the ranges between 3022 Å and 3128 Å and above 5990 Å we considered two additional HIRES spectra that were used specifically for these regions. Additional spectra were also retrieved from the archive and used to measure radial velocities. Unfortunately, the normalization of HIRES spectra is difficult since the spectral orders are narrower than many broad Balmer or helium lines. This is not a problem for sharp metal lines, but renders the spectra next to useless for the determination of atmospheric parameters of HZ 44.

## 5.3 Atmospheric parameters and radial velocities

In order to analyze these spectra, we computed non-LTE model atmospheres using the TLUSTY and SYNSPEC codes developed by Hubeny (1988); Lanz & Hubeny (2003). The models used for determining metal abundances are described in Sect. 5.6.

We derived atmospheric parameters for both stars using optical spectra (besides HIRES) and the He-sdO grid of synthetic spectra as described in Sect. 3.3. The selection of all lines we used, as well as the global best-fit model for HD 127493 is shown in Fig. 12. Our final atmospheric parameters of HZ 44 are determined from the ISIS spectrum shown in Fig. 13. The results from a simultaneous fit of all selected H and He I-II lines for both stars are shown in Table 5. In addition, atmospheric parameters for HD 127493 derived by Hirsch (2009) are listed since they are based on the same FEROS spectrum.

**Table 5.** Parameters derived from optical spectroscopy.

| Name | $T_{\mathrm{eff}}$ [K] | $\log g$ [cgs] | $\log N(\mathrm{He})/N(\mathrm{H})$ | $v_{\mathrm{rot}} \sin i$ [km s$^{-1}$] | Spectrum | Ref |
|------|------|------|------|------|------|------|
| HZ 44 | $39096 \pm 600$ | $5.64 \pm 0.10$ | $0.08 \pm 0.05$ | $< 5$ | ISIS | 1 |
| HD 127493 | $42070 \pm 184$ | $5.61 \pm 0.04$ | $0.33 \pm 0.06$ | $< 10$ | FEROS | 1 |
| | $42484 \pm 250$ | $5.60 \pm 0.05$ | $0.62 \pm 0.30$ | $< 10$ | FEROS | 2 |

**Notes.** References: [1] this work [2] Hirsch (2009) . The uncertainties stated were determined using different methods. Uncertainties on our results are determined using the bootstrapping method. Please to refer Hirsch (2009) for an explanation of their uncertainties.

We found no indication of rotation or microturbulence in either star; some optical metal lines are in fact broader in the model even assuming $v_{\mathrm{rot}} \sin i = 0 \, \mathrm{km\,s^{-1}}$.

Schork (2017) measured radial velocities of HZ 44 in 27 HIRES spectra, which were taken between 1995 and 2016, and determined an average radial velocity of $v_{\mathrm{rad}} = -12.7 \pm 0.4 \, \mathrm{km\,s^{-1}}$.

---

[5]Keck Observatory Archive, https://koa.ipac.caltech.edu/cgi-bin/KOA/nph-KOAlogin

We adopt this radial velocity for our abundance analysis. For HD 127493 we can confirm the radial velocity measurement from Hirsch (2009) as $v_{\rm rad} = -16\,{\rm km\,s^{-1}}$. The star has no known companion.
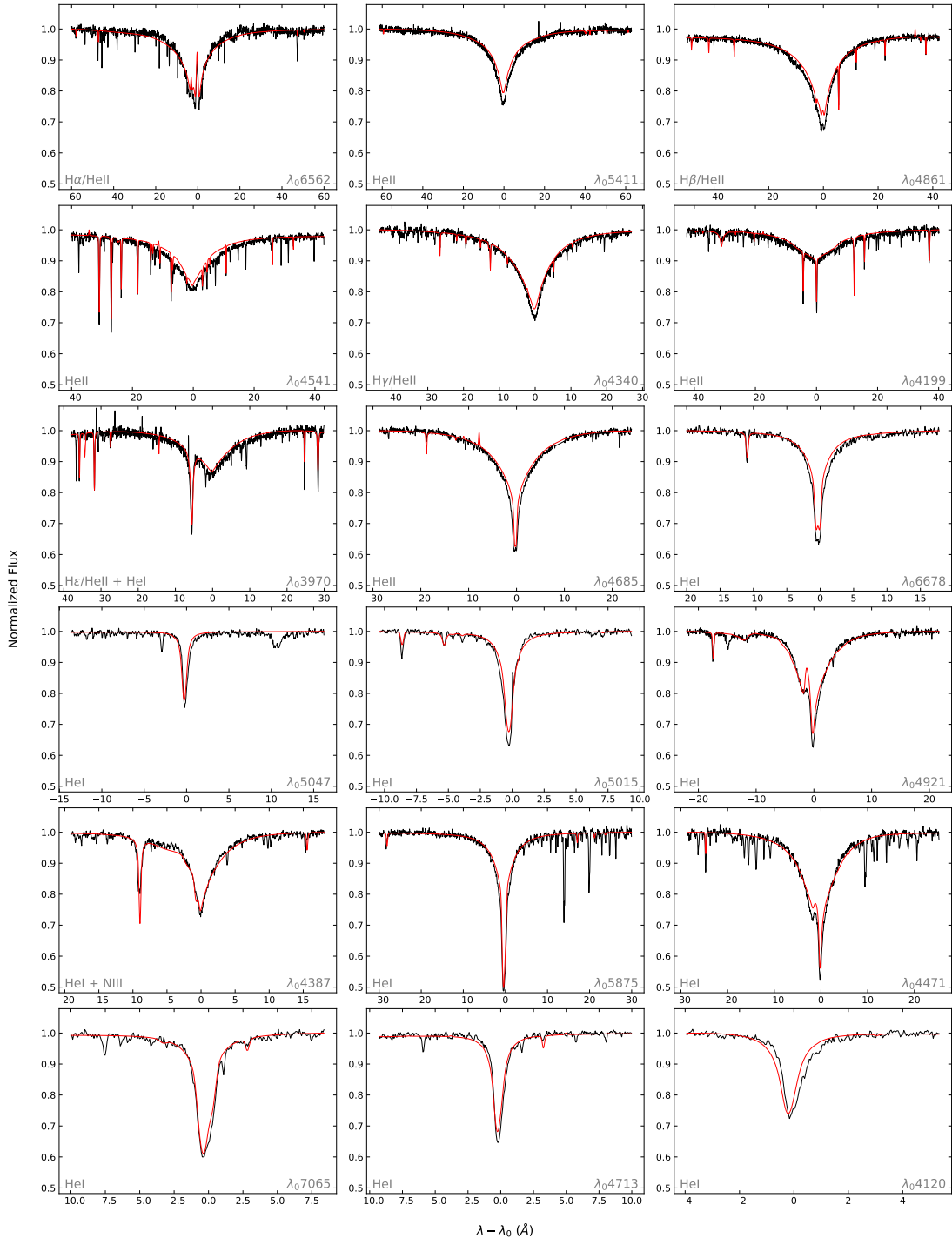


**Figure 12.**  Best fit (red) to the Balmer and helium lines selected in the normalized FEROS spectrum of HD 127493 (black).

## 5.4  Angular diameters, interstellar reddening, and stellar masses

With the release of *Gaia* DR2, high accuracy parallax ($\omega$) and therefore distance measurements have become available for a large sample of hot subdwarfs. This allows us to derive more precise spectroscopic masses for these stars. We collected photometric measurements from several surveys and converted them into fluxes (see Tables 12 and 13 in the appendix). In addition, we
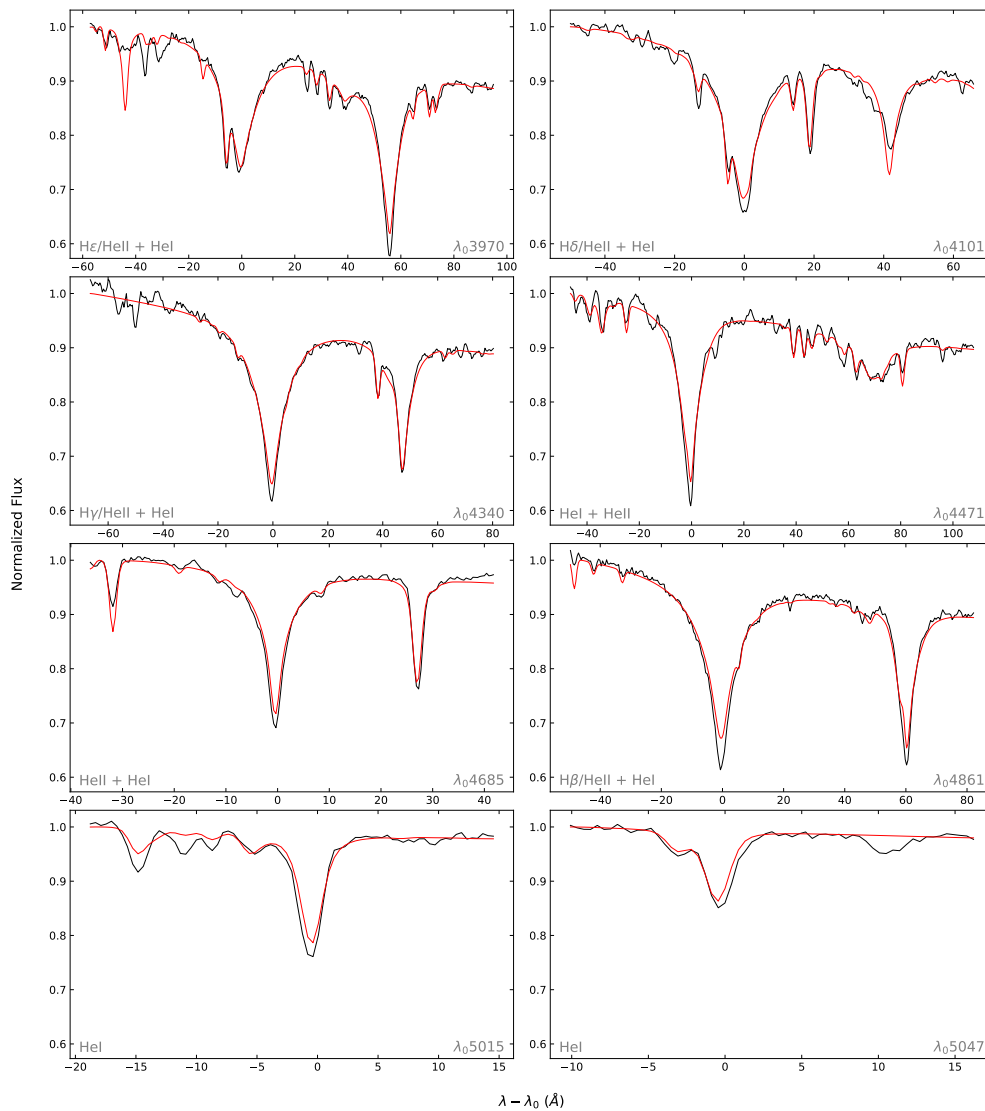
**Figure 13.** Best fit (red) to the Balmer and helium lines selected in the flux-calibrated ISIS spectrum of HZ 44 (black).

use low-resolution, large-aperture IUE spectra that were averaged in three regions (1300–1800 Å, 2000–2500 Å, 2500–3000 Å) as "box filters" to cover the UV region. Our photometric fitting procedure is described in detail in Heber et al. (2018). The $\chi^2$ fitting procedure scales our final synthetic spectra to match the photometric data and has the solid angle $\theta = 2R/D$ and the color excess $E_{B-V}$ as free parameters. Reddening is modeled with $R_V = 3.1$ as the extinction parameter (a standard value for the diffuse interstellar medium) and the corresponding mean extinction law from Fitzpatrick (1999). The resulting solid angle can be combined with the *Gaia* parallax distance to obtain the stellar radius, from which the stellar mass can be computed using the surface gravity derived from spectroscopy. The SED-fits are shown in Fig. 14 and the derived parameters in Table 6. Considering the non-detection of radial velocity variations and the evident lack of an infrared (IR) excess, we can state that there is no indication of binarity in HZ 44. The SED of HD 127493 shows no IR excess that would hint at a companion. The masses determined from the SED-fits are consistent with the canonical subdwarf mass, 0.47 $M_\odot$ (Fontaine et al. 2012, and references therein).

## 5.5  Atomic data

While atomic data and line lists for elements lighter than the iron-group are readily accessible via, for example, the Kurucz compilations and the NIST database, data for trans-iron elements
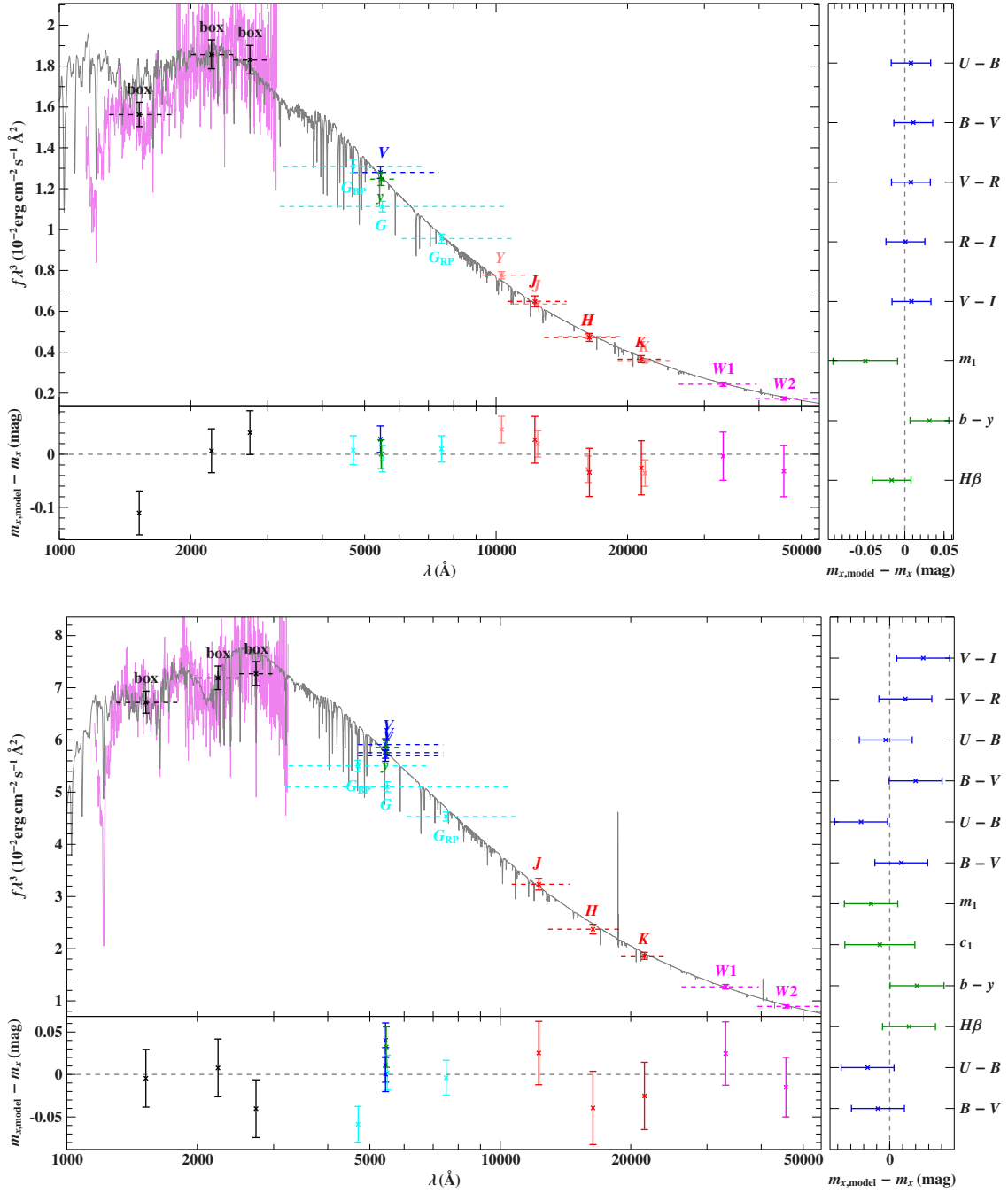
**Figure 14.** Comparison of synthetic spectra with photometric data for HZ 44 (top) and HD 127493 (bottom): The *main panel* shows the spectral energy distribution. The three black data points labeled "box" are binned fluxes from a low-dispersion IUE spectrum. Filter-averaged fluxes are shown as colored data points, which were converted from observed magnitudes (the dashed horizontal lines indicate the respective filter widths), while the grey solid line represents a synthetic spectrum using the atmospheric parameters given in Table 5. The residual panels at the bottom and right hand side show the differences between synthetic and observed magnitudes/colors. The following color codes are used to identify the photometric systems: Johnson-Cousins (blue), Strömgren (green), *Gaia* (cyan), UKIDSS (rose), 2MASS (red), WISE (magenta).

**Table 6.** Parallax and SED-fit results.

| Results | HZ 44 | HD 127493 |
|---|---|---|
| $\omega$ (mas) | $2.479 \pm 0.079$ | $5.821 \pm 0.091$ |
| $d$ (pc) | $403 \pm 13$ | $172 \pm 3$ |
| $\theta$ ($10^{-11}$ rad) | $2.134 \pm 0.011$ | $4.527 \pm 0.025$ |
| $E_{B-V}$ | $0.010 \pm 0.004$ | $0.052 \pm 0.004$ |
| $R/R_\odot$ | $0.191 \pm 0.007$ | $0.172 \pm 0.003$ |
| $M/M_\odot$ | $0.594 \pm 0.142$ | $0.432 \pm 0.053$ |

are much more scarce. Since these elements are of particular interest for the analysis of our two stars we invested particular effort into searching the literature and collecting data (energy levels, line positions and oscillator strengths) for many trans-iron elements. We list in Table 7 the ions we took into consideration as well as the references for their atomic data. We also include in this table, for each ion, the number of lines visible (with a predicted equivalent width greater than 5 mÅ) in the final model spectrum of HZ 44. The basis of our line list is the most recent line list published by Kurucz (2018), available online[6]. We then proceeded to add all lines with ionization stages IV-V provided by the Tübingen Oscillator Strengths Service (TOSS[7]) . The list was further extended with data listed in ALL, the Atomic Line List (v2.05b21)[8]. Additional lines were added from the theoretical works listed in Table 7. Finally the list was merged with the collection of lines from low-lying energy levels by Morton (2000), preferring more recent data if available.

## 5.6 Metal abundance analysis

Model atmospheres were calculated for the parameters listed in Table 5. As the first step, we extended model atmospheres from the atmospheric grid to include all metals that could be identified. We used the newest TLUSTY/SYNSPEC versions and hydrogen line broadening tables from Tremblay & Bergeron (2009) for these new models. All ions for which model atoms are available are included in non-LTE (see Table 8), while the remaining elements are treated with the LTE approximation. Heavy elements in ionization stages IV-VI were included in SYNSPEC as described in Sect. 3.2. Abundances in the TLUSTY model were set to values estimated by eye at this point. Based on this preliminary model, a series of synthetic spectra with a range of abundances for each element were created with SYNSPEC. The abundance of each element was determined one-by-one using the downhill-simplex fitting program SPAS developed by Hirsch (2009). This method works well for un-blended lines but is not reliable for heavily blended lines, in particular from heavy elements in the UV region. The abundance of these elements was estimated by manually comparing models with the observation. Even with this method, the placement of the continuum (especially in the FUSE range) remains an important source of uncertainty. As noted by Pereira et al. (2006), the true continuum in the FUSE spectral region may be well above the highest observed fluxes. This complicates the continuum placement since some opacity (photospheric and interstellar) is missing even in our line-blanketed synthetic spectra.

We could only derive upper limits for some elements. This includes elements with low abundances but also elements that show lines in the FUSE range only, where the aforementioned problems are most severe. For some elements no information about the abundance in HD 127493 could be determined (Cl, K, As, Se, Sb, Te, Xe, Bi). This is due to insufficient spectral coverage: the elements in question have their strongest spectral lines only in those spectral ranges where no observations are available (FUSE, UVA).

---

[6]Kurucz/Linelists, http://kurucz.harvard.edu/linelists/gfnew/gfall08oct17.dat
[7]Tübingen Oscillator Strengths Service, http://dc.g-vo.org/TOSS
[8]Atomic Line List (v2.05b21), http://www.pa.uky.edu/~peter/newpage/

**Table 7.**   Sources of oscillator strengths that are not included in the Kurucz line-list (`gfall08oct17.dat`) and number of lines.

| Ion | $N_{\mathrm{UV}}$ | $N_{\mathrm{VIS}}$ | Reference | Ion | $N_{\mathrm{UV}}$ | $N_{\mathrm{VIS}}$ | Reference | Ion | $N_{\mathrm{UV}}$ | $N_{\mathrm{VIS}}$ | Reference |
|---|---|---|---|---|---|---|---|---|---|---|---|
| Ga III | 3 | 2 | 15, 2(28) | Sr v* | 23 | – | 3 | Te v* | 1 | – | 1(30) |
| Ga IV | 69 | – | 3 | Y III* | 1 | 2 | 10, 16 | Te vI* | 2 | – | 3 |
| Ga v | 37 | – | 3 | Zr IV | 11 | 8 | 3 | Xe IV* | 5 | – | 3 |
| Ge III | 1 | – | 1(25,18) | Zr v | – | – | 3 | Xe v* | 4 | – | 3 |
| Ge IV | 7 | 6 | 23, 2(28) | Mo IV* | 92 | – | 29,3 | Ba v* | 2 | – | 3 |
| Ge v | 24 | – | 3 | Mo v* | 69 | – | 3 | Tl III* | – | – | 5 |
| As III | – | – | 1(26,19,17) | Mo vI* | 5 | – | 3 | Pb III | 2 | – | 7, 1(24) |
| As IV | – | – | 2(27), 1(25) | In III* | 5 | – | 4 | Pb IV | 17 | 9 | 11, 5, 8, 1(24) |
| As v | 2 | – | 1(19) | Sn III | – | – | 13 | Pb v | 36 | – | 9 |
| Se IV* | 3 | – | 1(22) | Sn IV | 7 | – | 4, 12 | Bi III* | – | – | 1(23) |
| Se v* | 4 | – | 3 | Sb III* | – | – | 1(17) | Bi IV* | – | – | 1(21) |
| Kr IV* | 42 | 5 | 3 | Sb IV* | 1 | – | 1(20) | Bi v* | 1 | – | 5 |
| Kr v* | – | – | 3 | Sb v* | 2 | – | 4 | Th IV* | 2 | – | 6 |
| Sr IV* | 109 | 1 | 3 | Te III* | – | – | 14 | | | | |

**Notes.** The number of lines with predicted equivalent width greater than 5 mÅ in the final model of HZ 44 and in spectral ranges where observations are available for HZ 44 are listed (UV: $916 - 1980$ Å, VIS: $3022 - 7580$ Å). Ions with upper limits only are marked with a *. References from compilations are listed as compilation (references). References:
(1) Morton (2000), (2) ALL, van Hoof (2017), (3) TOSS, Rauch et al. (2015), (4) Safronova et al. (2003), (5) Safronova & Johnson (2004), (6) Safronova & Safronova (2013), (7) Alonso-Medina et al. (2009), (8) Alonso-Medina et al. (2011), (9) Colón et al. (2014), (10) Naslim et al. (2011), (11) Naslim et al. (2013), (12) Biswas et al. (2018), (13) Haris & Tauheed (2012), (14) Zhang et al. (2013), (15) Nielsen et al. (2005), (16) Redfors (1991), (17) Andersen & Lindgard (1977), (18) Andersen et al. (1979), (19) Pinnington et al. (1981), (20) Pinnington et al. (1985b), (21) Pinnington et al. (1988), (22) Bahr et al. (1982), (23) Migdałek (1983), (24) Ansbacher et al. (1988), (25) Curtis (1992), (26) Marcinek & Migdalek (1993), (27) Churilov & Joshi (1996), (28) O'Reilly & Dunne (1998), (29) Kurucz (2018), (30) Pinnington et al. (1985a)

**Table 8.**   Model atoms used for the final model with their number of explicit levels (L) and superlevels (SL).

| Ion | L | SL | Ion | L | SL | Ion | L | SL | Ion | L | SL |
|---|---|---|---|---|---|---|---|---|---|---|---|
| H I | 17 | – | O IV | 31 | 8 | Si II | 23 | 10 | Ar IV | 39 | – |
| He I | 24 | – | O v | 35 | 5 | Si III | 31 | 15 | Ar v | 25 | – |
| He II | 20 | – | O vI | 15 | 5 | Si IV | 19 | 4 | Ca II | 32 | – |
| C II | 34 | 5 | Ne II | 23 | 9 | P IV | 14 | – | Ca III | 15 | 4 |
| C III | 34 | 12 | Ne III | 22 | 12 | P v | 13 | 4 | Ca IV | 17 | 4 |
| C IV | 35 | 2 | Ne IV | 10 | 2 | S II | 23 | 10 | Fe III | 50 | – |
| N II | 32 | 10 | Mg II | 21 | 4 | S III | 29 | 12 | Fe IV | 43 | – |
| N III | 40 | 8 | Mg III | 37 | 3 | S IV | 33 | 5 | Fe v | 42 | – |
| N IV | 34 | 14 | Mg IV | 29 | 5 | S v | 20 | 5 | Ni III | 36 | – |
| N v | 21 | 4 | Mg v | 18 | 2 | S vI | 13 | 3 | Ni IV | 38 | – |
| O II | 36 | 12 | Al II | 20 | 9 | Ar II | 42 | 12 | Ni v | 48 | – |
| O III | 28 | 13 | Al III | 19 | 4 | Ar III | 27 | 17 | Total | 1290 | 249 |

Table 14 shows the derived photospheric abundances of HZ 44 and HD 127493. A comparison to solar abundances taken from Asplund et al. (2009) is shown in Fig. 21. The solar abundances of As, Se, Sb, Te, and Bi are based on meteorite measurements. For some elements, the uncertainty on the solar photospheric abundance contributes significantly to the total uncertainty on the ratio with solar abundances: Ne, Ar, Cl, In, Sn, Tl, Pb, and Th.

The uncertainty we state on upper limits and by-eye abundances is defined as follows: at the upper bound the lines are judged to be clearly too strong, while they can not be discerned from noise at the lower bound. In the following subsections, we present in detail the result of our abundance analysis for each element: light elements (C, N, O) in Sect. 5.6.1, intermediate elements (F, Ne, Na, Mg, Al, Si, P, S, Cl, Ar, K, Ca, Ti) in Sect. 5.6.2, iron group elements treated in non-LTE (Fe, Ni) in Sect. 5.6.3, iron-group elements treated in LTE (V, Cr, Mn, Co, Cu) in Sect. 5.6.4, detected trans-iron elements ( Ge, Ga, As, Zr, Sn, Pb) in Sect. 5.7, trans-iron elements with upper limit (Kr, Sr, Y, Mo, Sb, Te, Xe, Th) in Sect. 5.8, and finally in Sect. 5.9 the elements for which we could not even asses an upper limit due to the weakness of their predicted lines (Sc, In, Ba, Tl, Bi). We then discuss the chemical portrait we obtained for both stars (Sect. 5.10) and compare our abundances with earlier estimates (Sect. 5.11). In the following text we give our abundances as $\log N_X/N_H$ and use the shorter notation [X/H] as before. To put this abundance in perspective, we additionally state the corresponding number density relative to solar values $n_X/n_{X,\odot}$ (as opposed to $[X/H]/[X/H]_\odot$).

### 5.6.1 Light metals (C, N, O)

The *carbon* abundance in HZ 44 was measured using nine optical C III lines. The abundance derived this way, [C/H] = $-4.31 \pm 0.13$ ($8.6 \times 10^{-2}$ times solar), is consistent with the strong C III and C IV lines observed in the UV region.
Carbon lines are weaker in the optical spectrum of HD 127493. We use the resonance doublet C IV $\lambda\lambda$ 1548, 1551 Å and the C III sextuplet lines at 1175 Å to derive an abundance of [C/H] = $-4.30 \pm 0.08$ ($3.9 \times 10^{-2}$ times solar).

The *nitrogen* abundances measured in HZ 44 from different ionization stages/lines in the optical region are not very consistent[9]. Most N III lines are well reproduced; some are too strong (e. g. N III $\lambda\lambda$ 4378.99, 4379.20 Å), while few are too weak (e. g. N III 4003.58 Å). We identified only one strong N IV line in the optical spectrum of HZ 44 (N IV 4057.76 Å), which fits the final model well. We measure an abundance of [N/H] = $-2.39 \pm 0.21$ (29 times solar) for HZ 44.
To constrain the N abundance in HD 127493 we used optical N III-IV lines in addition to UV lines, including the N V $\lambda\lambda$ 1238.8, 1242.8 Å resonance lines, the strong N IV 1718 Å line, and several N III lines. All ionization stages give a consistent abundance of about [N/H] = $-2.09 \pm 0.17$ (26 times solar).

The abundance of *oxygen* in HZ 44 was measured using optical O II and O III lines. Although these lines are weak compared to lines from other elements, they can still be used to find an abundance of [O/H] = $-3.77 \pm 0.13$ ($12 \times 10^{-2}$ times solar). The strongest observed O lines in the UV (O III 1150.884 Å in FUSE and O IV 1343.514 Å in the IUE/SWP spectrum) support this value. O IV $\lambda\lambda$ 1338.615, 1343.514 Å are also observed in the GHRS spectrum of HD 127493 but blended with Ni lines. Since no optical lines are detectable we only set an upper limit of [O/H] $\leq -4.3$ ($2 \times 10^{-2}$ times solar) and note that the actual abundance is likely not significantly lower.

### 5.6.2 Intermediate metals (F to Ti)

For HZ 44, all elements from fluorine to titanium were analyzed. Due to the lack of UVA and FUSE spectra, P, Cl, Ar, K, and Ti could not be studied in HD 127493. HD 127493 is also hotter than HZ 44, so important lines from lower ionization stages are weak or not detectable in the

---

[9]Many strong N II lines are too broad and shallow in the model, even assuming a rotation velocity and microturbulence of $0\,\mathrm{km\,s^{-1}}$ and were therefore excluded from the fit (e. g. N II $\lambda\lambda$ 3995.00, 4041.31, 4236.91 Å). In HD 127493 some N II lines appear in emission in the model but not the observation (e. g. N II $\lambda\lambda$ 4530.41, 5005.15 Å). This may be related to numerical issues due to low population numbers.

FEROS spectrum (e. g. Na II, F II).

No *fluorine* lines are observed in HZ 44, which allows us to provide an upper limit of [F/H] ≤ −5.0 ± 0.4 (130 times solar) based on F II λλ 3503.11, 3505.63, 3847.09, 3849.99, and 3851.67 Å. None of these F II lines are strong enough in HD 127493 set a meaningful limit on the abundance.

The *neon* abundance measurement for HZ 44 is based on several strong Ne II lines, which are somewhat weaker in HD 127493 due to its higher temperature but strong enough to determine the Ne abundance. Most of them lie between 3300 Å and 3800 Å though some strong Ne II lines exist at longer wavelengths. Fitting all accessible Ne lines results in [Ne/H] = −3.23 ± 0.11 (3.3 times solar) for HZ 44 and [Ne/H] = −2.38 ± 0.18 (3.1 times solar) for HD 127493. The weaker Ne III lines are reasonably well reproduced with the abundance stated above.

*Sodium* lines are weak, but clearly visible in HZ 44, most notably Na II λλ 3285.608, 3533.057, 3631.272, and 4392.808 Å. We find [Na/H] = −4.43 ± 0.06 (10 times solar) for HZ 44. Na II λλ 4392.808, 4405.124 Å allow an upper limit of [Na/H] ≤ −3.4 ± 0.3 (48 times solar) to be set for HD 127493.

The strongest observed *magnesium* lines are by far the Mg II triplet at 4481 Å. All other optical lines are too weak to be observed in either star. We derive [Mg/H] = −3.80 (1.9 times solar) for HZ 44 and [Mg/H] = −3.39 (2.1 times solar) for HD 127493, consistent with Mg II 2798.823 Å in the IUE LWR spectrum.

We measure the *aluminum* abundance in HZ 44 to be [Al/H] = −4.86 ± 0.11 (2.4 times solar) based on eleven optical Al III lines. This abundance is consistent with strong Al III lines observed in the UV range, including the Al III λλ 1854.716, 1862.790 Å resonance lines. The Al abundance in HD 127493, [Al/H] = −4.53±0.10 (2.2 times solar), is derived from Al III λλ 4479.971, 4512.565, 4529.189, and 5696.604 Å.

Both stars show strong *silicon* lines in optical and UV spectra. For HD 127493 we used three lines in the UV (including the resonance doublet Si IV λλ 1394, 1403 Å) for our fit in addition to four lines from the optical range. Both UV and optical lines give a consistent abundance of [Si/H] = −3.31 ± 0.14 (3.2 times solar). The abundance measurement for HZ 44 is based on ten optical Si III and nine optical Si IV lines. The derived abundance of [Si/H] = −3.88 ± 0.11 (2.0 times solar) is consistent with the resonance lines Si IV λλ 1394, 1403 Å, the very strong Si IV λλ 1066.6, 1122.5, 1128.3 Å, and Si III 1113.2 Å in the FUSE spectrum, as well as many more silicon lines in the UV region.

The strongest observed *phosphorus* lines lie in the FUSE spectral range, which is only accessible for HZ 44. This includes the P V λλ 1117.98, 1128.01 Å, and P IV 950.657 Å resonance lines as well as several strong P IV lines, e. g. P IV 1030.515 Å. In the optical/UVA range, there are only three observable lines: P IV λλ 3347.739, 3364.470 Å (see Fig. 15) and P IV 4249.655 Å. We derive an abundance of [P/H] = −5.66 ± 0.25 (4.1 times solar) for HZ 44. The only unambiguously identified P line in HD 127493, P IV 1888.524 Å, can be used to derive an upper limit of [P/H] = −4.7 ± 0.3 (16 times solar).

Besides many strong *sulfur* III-IV lines at optical wavelengths, we observed strong S III-VI lines in the UV spectrum of HZ 44 (e. g. S IV λλ 1062.66, 1072.97, 1623.94 Å). However, some of those lines are listed with inaccurate wavelengths and oscillator strengths in the newest Kurucz line list. The abundance measurement of [S/H] = −3.87 ± 0.37 (4.9 times solar) based on optical S III-IV lines is consistent with the UV lines. Several optical S III lines are too weak and broad in the model (e. g. S III λλ 3497.280, 3662.01, 3717.77, 3928.61, 4361.47 Å) and were excluded from the fit. Sulfur lines are weaker in HD 127493. We derive an abundance of [S/H] = −3.90 ± 0.35 (2.0 times solar) from UV lines (the strongest being S V 1502 Å).

*Chlorine* shows strong lines from low-lying levels in the FUSE spectral region (Cl IV λλ 973.217, 977.565, 977.899, 984.959, 985.755 Å). Although these lines are strong in HZ 44, it is hard to determine abundances from them. They are quite insensitive to changes in abundance due to saturation effects. In addition, the usual problems with lines in the FUSE spectra apply: they suffer from unidentified blends, both of stellar and interstellar origin. With [Cl/H] ≤ −7.0 ± 0.7 (0.05 times solar), the upper limit for HZ 44 derived from these lines is astonishingly low despite

the large uncertainty.

*Argon* shows many strong lines in the UVA spectrum of HZ 44. We determine an abundance of [Ar/H] = −3.79 ± 0.11 (31 times solar) for HZ 44 based on optical/UVA lines. Some strong optical Ar III lines (e. g. Ar III $\lambda\lambda$ 3286.11, 3302.19, 3311.56 Å) were excluded from the fit since they show the same discrepancies already observed in N II lines – they are very narrow in the observation and too broad in the model. Except for a very weak Ar III 4182.965Å line, we could identify no optical Ar lines in HD 127493. The upper limit for HD 127493 derived from this line is still super-solar at [Ar/H] ≤ −3.6 ± 0.2 (21 times solar). The blended Ar IV $\lambda\lambda$ 1409.300, 1435.556 Å and Ar IV 2641.090 Å fit well at this abundance, Ar V 1371.868 Å suggests an even lower abundance.

We found no strong *potassium* lines in the UV spectrum of HZ 44, but some of medium strength are visible in the optical region. We found no strong *potassium* lines in the UV spectrum of HZ 44, but some optical lines can clearly be identified. Several lines appear to lie at shorter wavelengths than listed in the Kurucz line list. Since the difference correlates with their LS-coupling terms, it seemed reasonable in order to shift them to match their observed position. Their wavelengths and configurations are listed in Table 9. Other K lines are clearly identified at wavelengths very close to their listed value (K III $\lambda\lambda$ 3052.016, 3468.314, 3513.822 Å). As shown in Fig. 15, lines with a $^4$P lower term had to be shifted by approximately −0.1 Å whereas the shift was larger for all lines with $^2$P lower terms. All identified lines are reproduced reasonably well with an abundance of [K/H] ≤ −4.92 ± 0.16 (55 times solar), when shifted to the observed position. Since the identification is ambiguous for two lines, the uncertainty on this abundance measurement is higher than the standard deviation stated here.

**Table 9.** K III lines with deviation between predicted and observed wavelengths (compare Fig. 15).

| $\lambda_{\mathrm{Kurucz}}$ (Å) | $\lambda_{\mathrm{obs}}$ (Å) | $\Delta\lambda$ (Å) | Configuration |
|---|---|---|---|
| 3253.973 | 3253.563 | −0.41 | $4s\,^2P_{3/2} - 4p\,^2D^\circ_{3/2}$ |
| 3278.787 | 3278.687 | −0.10 | $4s\,^4P_{5/2} - 4p\,^4P^\circ_{3/2}$ |
| 3289.046 | 3288.796 | −0.25 | $4s\,^2P_{3/2} - 4p\,^2D^\circ_{5/2}$ |
|  | 3288.986* | −0.06 |  |
| 3322.396 | 3322.326 | −0.07 | $4s\,^4P_{5/2} - 4p\,^4P^\circ_{5/2}$ |
|  | 3321.546* | −0.85 |  |
| 3358.426 | 3358.346 | −0.08 | $4s\,^4P_{3/2} - 4p\,^4P^\circ_{1/2}$ |
| 3364.326 | 3363.706 | −0.62 | $4s\,^2P_{1/2} - 4p\,^2P^\circ_{3/2}$ |
| 3468.314 | 3468.260 | −0.05 | $4s\,^4P_{3/2} - 4p\,^4P^\circ_{5/2}$ |
| 3513.822 | 3513.782 | −0.04 | $4s\,^4P_{1/2} - 4p\,^4P^\circ_{3/2}$ |

**Notes.** The configurations are taken from NIST. The superscript * marks alternative identifications. Energy levels are represented by their highest occupied electron orbital $n\,l$, where $n$ is the principal quantum number (1, 2, 3, 4, ...) of the electron shell and $l$ is the orbital angular momentum number (s, p, d, f, g, ...) of the subshell, followed by the LS coupling term $^{2S+1}L_J$, where $S$ is the total spin, $L$ the total orbital angular momentum (S, P, D, F, G, ...), and $J$ the total angular momentum quantum number. The term superscript ° indicates odd parity.

While there are no usable *calcium* lines in the optical spectrum of HD 127493, HZ 44 shows some strong Ca II and Ca III lines. The optical resonance lines Ca II $\lambda\lambda$ 3934, 3968 Å are almost entirely photospheric. Similar to the problematic N II lines, some strong Ca III lines were excluded from the fit (e. g. Ca III $\lambda\lambda$ 3372.679, 3537.777 Å) since they have sharp cores and are too broad and shallow in the model. Non-LTE effects can not be blamed since we included Ca II and Ca III in non-LTE. We measure [Ca/H] = −3.9 ± 0.24 (28 times solar) for HZ 44 and derive an upper limit of [Ca/H] ≤ −3.9 ± 0.2 (12 times solar) for HD 127493. This upper limit might be close to the actual abundance since including Ca at this abundance improves the fit for blended UV lines such as Ca III 1545.300 Å and Ca IV $\lambda\lambda$ 1647.438, 1648.622, 1655.533 Å.

**Figure 15.** The strongest K III lines in the observed spectrum of HZ 44. The model using the Kurucz wavelengths is shown in red, while a model with shifted lines is shown in blue. Alternative line shifts are shown in green (marked with $^*$ in Table 9). All models have a potassium abundance of [K/H] = −5.
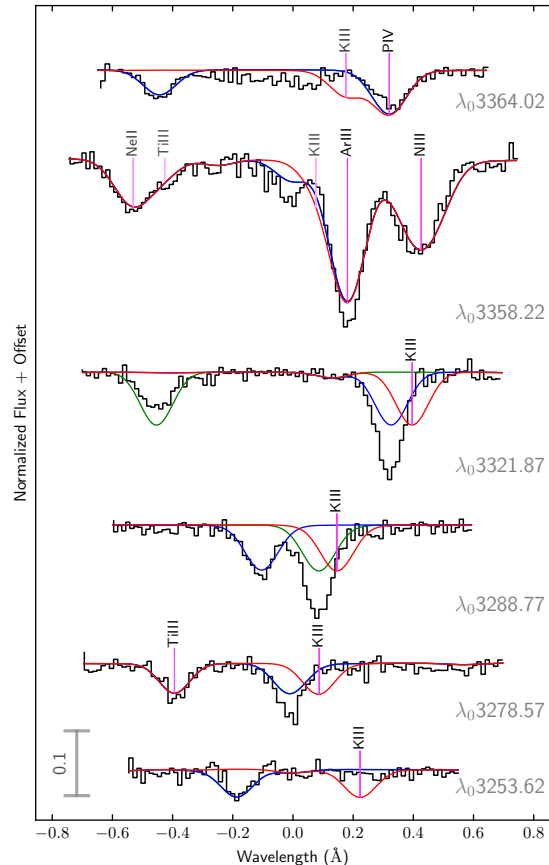
The strongest *titanium* III-IV lines lie in the UVA spectral region although some lines exist at longer wavelengths. We measure a strong enrichment in HZ 44, [Ti/H] = −4.56 ± 0.22 (150 times solar). This abundance is consistent between strong optical and ultraviolet lines (e. g. Ti IV $\lambda\lambda$ 1183.628, 1451.739, 1467.343, 1469.191 Å and Ti III 1498.695 Å). Although Ti lines at wavelengths above 3800 Å are strong in HZ 44, the same lines are weak in HD 127493. The few lines that can clearly be identified in HD 127493 (Ti IV $\lambda\lambda$ 4397.312, 5885.965 Å) do not give a consistent abundance. Other predicted lines (Ti IV $\lambda\lambda$ 4397.312, 5398.930, 5492.512 Å) are not observed. Therefore we adopt a conservative upper limit of [Ti/H] ≤ −4.40 ± 0.25 (94 times solar) for HD 127493 based on optical lines. Ti III-IV lines in the IUE range would be consistent with higher abundances.

### 5.6.3  Fe and Ni (NLTE)

We determine *iron* abundances by fitting the IUE spectrum of HZ 44 and the GHRS spectrum of HD 127493 in ranges that span 10 to 20 Å, from 1300 Å onward (at shorter wavelengths, the amount of unidentified opacity increases). This procedure may somewhat overestimate abundances. Blends are not treated exactly since Fe and Ni are fit separately. However, since abundances in the initial model were already close to the best-fit abundances, this effect is partly compensated. Missing opacity from other sources can also introduce a bias towards higher abundances. The average over all ranges yields an average abundance of [Fe/H] = −4.0 ± 0.25 (1.5 times solar) for HZ 44  and [Fe/H] = −2.8 ± 0.13 (10 times solar) for HD 127493.

The same procedure was applied for *nickel*, resulting in [Ni/H] = −4.05 ± 0.15 (26 times solar) for HZ 44 and [Ni/H] = −3.61 ± 0.13 (31 times solar) for HD 127493.

### 5.6.4  Additional iron-group abundances (LTE)

The UV spectral range is dominated by many lines from iron-peak elements. Although most lines are from iron and nickel, opacity contributions from other iron-peak elements are also significant. Figure 16 shows the number of lines from iron-peak elements with equivalent width larger than

5 mÅ in the final model for HZ 44. While many of these lines are observed in FUSE and IUE spectra, the opacity peak below 900Å is outside of our observed spectral range.
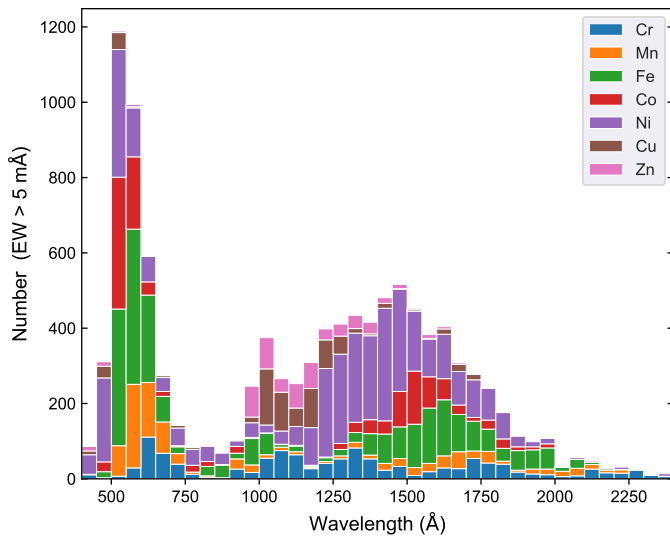


**Figure 16.** Histogram of iron-peak lines with estimated equivalent widths larger than 5 mÅ in the final model of HZ44. Bins are every 50 Å.

Our models include only Fe and Ni in non-LTE. Most other iron-peak element lines fit reasonably well when included in LTE, besides V and Cu. Cu shows many lines between 1000 Å and 1300 Å most of which fit well and can be identified as Cu IV lines but some are too strong in the model.

Many *vanadium* lines in the IUE spectrum of HZ 44 would fit well with abundances of up to $[V/H] = -4.8$ (e. g. V IV $\lambda\lambda$ 1226.53, 1308.05, 1356.53, 1426.65, 1520.16, 1522.51, 1810.58, 1817.69, 1861.57 Å, and V v 1680.20 Å). It seems unlikely that such a large amount of lines would fit the observation due to accidental alignment with unmodeled blends. However, other lines suggest abundances below $[V/H] \leq -6.0 \pm 0.4$, e. g. V IV $\lambda\lambda$ 1317.56, 1329.28, 1355.13, 1806.20 Å. Several lines in the FUSE spectrum seem to exclude abundances of more than $[V/H] \leq -5.2 \pm 0.4$, e. g. V IV $\lambda\lambda$ 1071.06, 1112.20, 1123.43 Å, and V III 1149.95 Å. However, these lines lie in regions where the continuum is poorly defined due to unidentified blends. We conclude that a precise abundance determination for vanadium would require a more complete model, possibly including V in non-LTE. Therefore we set an upper limit of $[V/H] \leq -4.8 \pm 0.4$ (893 times solar) for HZ 44. For HD 127493, V IV $\lambda\lambda$ 1317.56, 1329.28 Å exclude abundances higher than $[V/H] \leq -6.0 \pm 0.4$ (25 times solar), V IV 1355.13 Å even fits well with this abundance.

*Chromium* shows many strong lines in the ultraviolet spectrum of both stars. The overall fit is good, but some lines are too strong in the best fit (e. g. Cr IV 1401.326 Å) or are poorly modeled (e. g. Cr IV 1967.176 Å, likely listed at the wrong wavelength). There are many strong Cr lines in the IUE region, e. g. Cr IV $\lambda\lambda$ 1433.89, 1658.08, 1825.00, 1826.22, 1826.88, 1827.43 Å. We adopt an abundance of $[Cr/H] = -4.4 \pm 0.3$ (28 times solar) for HZ 44 and $[Cr/H] = -3.9 \pm 0.3$ (76 times solar) for HD 127493.

We derive the *manganese* abundance in HZ 44 from FUSE and IUE to $[Mn/H] = -4.9 \pm 0.4$ (22 times solar). Fairly strong and unblended lines are among many others: Mn III $\lambda\lambda$ 917.80, 956.47 Å and Mn IV $\lambda\lambda$ 1450.36, 1780.00, 1786.05 Å.

For HD 127493 we derive an upper limit of $[Mn/H] \leq -5.5 \pm 0.3$ (2.5 times solar) from several undetected lines in the GHRS spectrum: Mn IV $\lambda\lambda$ 1244.327, 1720.868, 1721.490, 1724.902 Å.

*Cobalt* lines in the FUSE spectrum of HZ 44, e. g. Co III $\lambda\lambda$ 944.771, 946.540, 946.608 Å suggest an upper limit of $[Co/H] \leq -5.6 \pm 0.4$. Many Co lines in the IUE region, e. g. Co IV $\lambda\lambda$ 1451.427, 1502.059, 1502.702, 1508.416 Å support this upper limit. Other lines fit well with this or a slightly higher abundance: Co IV $\lambda\lambda$ 1494.748, 1500.578, 1502.194, 1565.908 Å. Because of the unambiguous identification of Co lines but a slight discrepancy between upper limit and best-fit we adopt $[Co/H] = -5.6 \pm 0.5$ (12 times solar) with a relatively large uncertainty. In HD 127493 Co IV $\lambda\lambda$ 1535.282, 1540.557, 1548.827, 1559.637, 1636.404 Å are resolved by GHRS and fit well at an abundance of $[Co/H] = -5.1$, while Co IV $\lambda\lambda$ 1415.050, 1550.277, 1562.063 Å suggest an abundance no higher than $[Co/H] \leq -5.3$. We therefore adopt an abundance of $[Co/H] =$

−5.3 ± 0.3 (9 times solar) and note that discrepancies between single lines could result from in-accuracy in line wavelengths or non-LTE effects.

Many strong *copper* lines lie in the FUV spectral region. Cu IV λλ 1053.731, 1057.622 Å in the FUSE spectrum of HZ 44 are quite strong and almost free from blends. Other strong Cu lines are affected by unidentified blends or lie in a region where the continuum placement is not well constrained. Cu lines are weaker in the IUE spectrum, with a few notable exceptions: Cu III λλ 1674.591, 1684.627, 1702.106 1709.029, 1722.367 Å. We determine an abundance of [Cu/H] = −5.8 ± 0.4 (49 times solar) from the lines listed above.
Cu V lines such as Cu V λλ 1245.988, 1255.299, 1268.316, 1274.741, 1286.549, 1299.155 Å in the GHRS spectrum of HD 127493 exclude abundances higher than [Cu/H] ≤ −6.1 ± 0.4 (11 times solar).

## 5.7  Detected trans-iron peak elements (LTE)

We were able to measure the abundance of Ge, Ga, and Pb based on UV lines in both HZ 44 and HD 127493. In HZ 44 we could additionally derive abundances for As and Sn based on the FUSE spectrum.

In the following we will give a brief overview of the atomic data and lines used for the abundance measurement of each element. Errors on the abundances can be quite large. This is a result of the assumption of LTE, strong blending with unidentified lines in the ultraviolet region, and the sparse atomic data for most elements. Even if atomic data are available, oscillator strengths and line wavelengths are not always well tested.

In the context of of their ongoing "Stellar Laboratories" series, Rauch et al. (2015) have published a large collection of atomic data for elements with Z ≥ 30 on the TOSS website. While they focus on the analysis of hot white dwarfs with $T_{\text{eff}} > 60000$ K, they also provide atomic data for ions of stages IV-V that are observed in the sdOs discussed here.

We use their data for *gallium* IV-V and data from O'Reilly & Dunne (1998) for Ga III with updates for two lines from Nielsen et al. (2005). Many Ga lines are observed in the UV spectra of HZ 44 and HD 127493. The strongest, isolated lines in HZ 44 include Ga IV λλ 1163.609, 1170.585, 1258.801, 1299.476, 1303.540, and 1347.083 Å. However, a precise abundance measurement is difficult since most lines are relatively weak and blended with lines from other elements. Never-theless, we could measure an abundance of [Ga/H] = −6.0 ± 0.5 (440 times solar) for HZ 44. We only derive an upper limit of [Ga/H] ≤ −6.4 ± 0.4 (80 times solar) for HD 127493 since all Ga lines are weaker and blended.

*Germanium* shows many lines in the FUSE and IUE spectral range, including the strong reso-nance lines Ge IV λλ 1189.028, 1229.840 Å and Ge III 1088.463 Å. We identified lines from Ge III-V in HZ 44, which can be matched at an abundance of [Ge/H] = −5.9 ± 0.3. (140 times solar). For HD 127493, we derive an abundance of [Ge/H] = −5.0 ± 0.4 (470 times solar) from the strong resonance lines Ge IV 1189.028 Å (IUE) and Ge IV 1229.840 Å (GHRS, shown in Fig. 19).
Morton (2000) lists oscillator strengths for ten ultraviolet *arsenic* III lines from low-lying levels, as computed by Marcinek & Migdalek (1993). Oscillator strengths for several optical As IV lines are listed in ALL, originally from Churilov & Joshi (1996). The only ultraviolet As IV line listed in Morton (2000) is the resonance line As IV 1299.28 Å but the oscillator strength provided by Curtis (1992) is low ($f = 1.94 \cdot 10^{-3}$). Atomic data for the two resonance lines As V 987.651 Å and As V 1029.480 Å is provided by Pinnington et al. (1981), as listed in Morton (2000). These As V oscillator strengths have previously been used for the As abundance measurement in DO white dwarfs by Chayer et al. (2015) and Rauch et al. (2016a). Morton (2000) also lists a third resonance line, As V 1001.211 Å. This line is not observed in the spectrum of HZ 44 and was disregarded by both Chayer et al. (2015) and Rauch et al. (2016a). It is only mentioned in Froese Fischer (1977) (and may have been confused with the $^2S_{1/2}-^2P_{1/2}$ transition line As V 1029.480 Å). Neither NIST (Moore 1971) nor Joshi & van Kleef (1986) list an energy level that would be consistent with an As V resonance line at 1001.211 Å, so we decided to exclude it as well. As III lines are weak in HZ 44 and As III λλ 927.540, 944.726 Å exclude abundances higher than [As/H] ≤ −6.4 ± 0.4
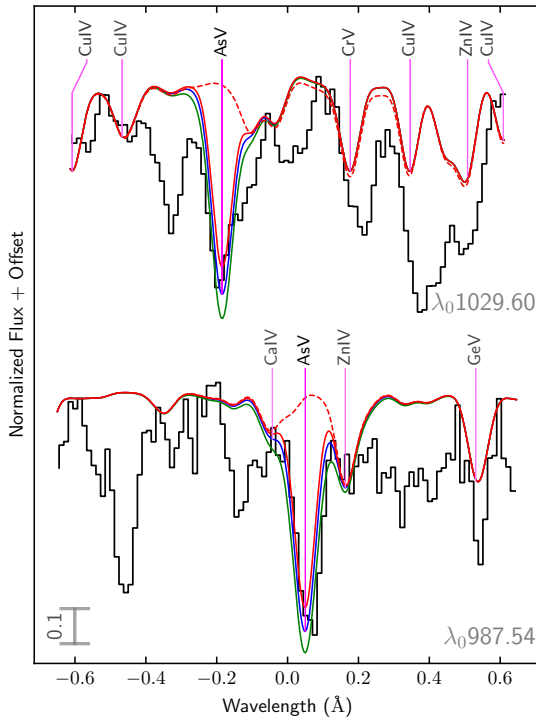
**Figure 17.** As v $\lambda\lambda$ 987.65, 1029.48 Å in the FUSE spectrum of HZ 44. In red: a model with [As/H] = −7.8; dashed without As. In blue: the adopted abundance [As/H] = −7.4. In green: [As/H] = −7.0.

(960 times solar). As IV 1299.28 Å would fit an otherwise unidentified line at an abundance of [As/H] = −5.6, which is excluded by other lines. Figure 17 shows the strongest observed As lines in HZ 44, As v 987.651 Å and As v 1029.480 Å. We use these lines to derive an abundance of [As/H] = −7.4 ± 0.4 (100 times solar).

HZ 44 is one of the few subdwarf stars that show *zirconium* in their optical spectrum. We use atomic data from Rauch et al. (2017a) for our analysis. We fitted four distinct Zr IV lines in the HIRES spectrum of HZ 44 (Zr IV $\lambda\lambda$ 3576.107, 3686.902, 4317.077, 4569.218, 4569.272 Å, see the left panel of Fig. 18) and find an abundance of [Zr/H] = −5.92 ± 0.19 (1500 times solar). Also the UV spectra of HZ 44 show Zr IV-V lines, and although none of them are strong or un-blended enough to independently measure the abundance, they are still consistent with the optical abundance measurements.

The doublet Zr IV $\lambda\lambda$ 4569.272, 4569.272 Å is visible in HD 127493 and would fit well with an abundance of [Zr/H] = −5.5 (1700 times solar). Since no other lines could clearly be identified as Zr we adopt an upper limit of [Zr/H] ≤ −5.4 ± 0.2.

*Tin* is one of the elements that were identified in HZ 44 by O'Toole (2004). We use atomic data from Safronova et al. (2003), supplemented with data from Biswas et al. (2018) for Sn IV and results from Haris & Tauheed (2012) for Sn III. We derive the Sn abundance in HZ 44 to [Sn/H] = −6.9 ± 0.4 (550 times solar), based on the strong Sn IV 1119.338 Å line, which is almost free from blends (see Fig. 18). The other strong, but blended Sn IV $\lambda\lambda$ 1019.720, 1044.487, 1314.539 Å, and Sn IV 1437.527 Å (blended with Co IV 1437.488 Å) lines support this measurement. Even if the FUSE continuum is estimated too high in our models, Sn lines in the IUE spectrum, where the model is more complete, set the upper limit to [Sn/H] ≤ −6.5 ± 0.4 (1400 times solar). Sn IV 1314.539 Å excludes abundances higher than [Sn/H] ≤ −6.6 ± 0.4 (480 times solar) for HD 127493.

We collected atomic data for *lead* III-V from several sources. Pb III oscillator strengths are from Alonso-Medina et al. (2009), with the exception of the resonance lines Pb III 1048.877 Å and Pb III 1553.021 Å, which are based on lifetime measurements by Ansbacher et al. (1988) as listed in Morton (2000). For Pb IV, we use oscillator strengths from Safronova & Johnson (2004) with additional lines from Alonso-Medina et al. (2011) and one line (Pb IV 4496.15 Å) from Naslim et al. (2013). Data for Pb V is provided by Colón et al. (2014). While this collection is far from complete, many Pb lines could be identified, including not only strong Pb III-v lines in the ultraviolet spectrum of HZ 44 but also five Pb IV lines in its optical spectrum (Pb IV $\lambda\lambda$ 3052.56,

**Figure 18.** *Left*: A selection of Zr IV and Pb IV lines in the HIRES spectrum of HZ 44. In blue: a model with [Zr/H] = −5.9 and [Pb/H] = −5.9. In red: the same model, but without Zr or Pb. *Right*: Pb III, Pb IV, Pb V, and Sn IV lines in the FUSE spectrum of HZ 44. In blue: a model with [Pb/H] = −5.9 and [Sn/H] = −6.9. In red: the same model, but without Pb.

3221.17, 3962.48, 4049.80, 4496.15 Å). Fitting all identified Pb lines in the HIRES spectrum except Pb IV 3052.56 Å (S/N too low) results in [Pb/H] = −5.89 ± 0.09 (11000 times solar), which is remarkably consistent with Pb lines observed in the UV region, including lines from Pb III and Pb V. As far as we know, this is the first time Pb V lines were modeled in any star. The strongest Pb lines per ionization stage observed in the FUSE spectrum of HZ 44 are shown in Fig. 18. The Pb abundance measurement in HD 127493 is based mostly on Pb IV 1313 Å, assuming a solar isotopic ratio as in O'Toole & Heber (2006). We derive an abundance of [Pb/H] = −5.65 ± 0.40 (8400 times solar), consistent with Pb V λλ 1233.50, 1248.46 Å in the GHRS spectrum.
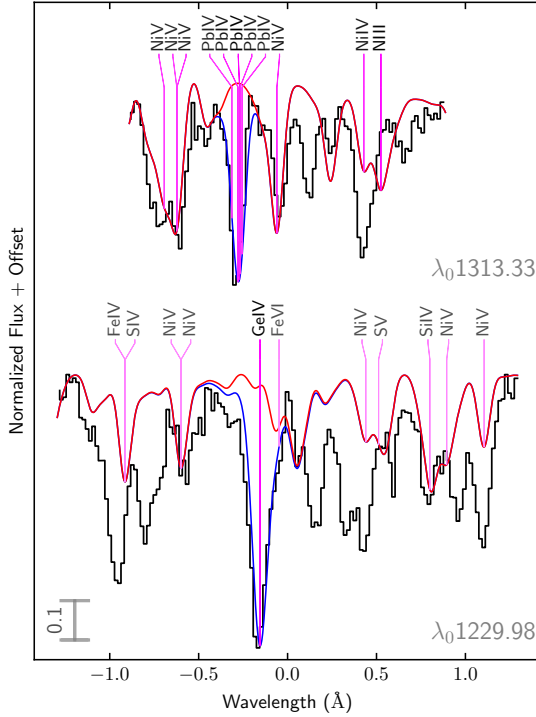


**Figure 19.** Ge IV and Pb IV lines in the GHRS spectrum of HD 127493. In blue: a model with [Ge/H] = −5.0, [Pb/H] = −5.7. In red: the same model, but without Pb and Ge.

## 5.8   Trans-iron peak elements with upper limits (LTE)

Also as part of their "Stellar Laboratories" series Rauch et al. (2017b) have measured the abundance of *selenium* in the peculiar DO white dwarf RE 0503−289. We use their oscillator strengths for Se V and results from Bahr et al. (1982) for Se IV, as listed in Morton (2000). Se IV λλ 959.590, 996.710 Å and Se V 1094.691 Å would fit an otherwise unidentified line at [Se/H] = −6.3 ± 0.4. However, Se IV 984.341 Å seems to exclude abundances higher than [Se/H] ≤ −7.6 ± 0.4. Like As V 1001.211 Å this line may not be real; its lower level is not listed in NIST nor in the newest reference on Se IV energy levels we found, Pakalka et al. (2018). Therefore, we adopt [Se/H] ≤ −6.3 ± 0.4 (110 times solar) as the upper limit for HZ 44.

*Krypton* and *strontium* belong to the group of elements that have been studied in white dwarfs by Rauch et al. (2016b, 2017b). Despite the large number of Kr IV-V lines in the TOSS line list, none of them are strong enough in the final synthetic spectrum of HZ 44 to identify in the observation. We derive a weak upper limit of [Kr/H] ≤ −5.2 ± 0.6 (1700 times solar) from four undetected Kr IV lines, the strongest being Kr IV 1538.211 Å. Kr IV 999.388 Å would fit well with an abundance of [Kr/H] = −5 but is likely blended. Kr IV λλ 1400.898, 1538.211, 1558.514 Å and Kr V 1293.917 Å in GHRS exclude abundances higher than [Kr/H] ≤ −4.8 ± 0.4 (1900 times solar) in HD 127493.

The situation is similar for *strontium* in HZ 44. The undetected Sr V 962.378 Å, Sr IV 1244.137 Å, and Sr IV 1244.763 Å lines exclude abundances higher than [Sr/H] ≤ −5.1 ± 0.6 (5100 times solar). Sr IV 1331.129 Å would fit well with [Sr/H] = −5.0. Sr IV λλ 1244.137, 1244.888, 1268.622, 1275.354, 1729.533 Å in GHRS exclude abundances higher than [Sr/H] ≤ −4.9 ± 0.3 (3600 times solar) in HD 127493.

Naslim et al. (2011) have observed *yttrium* in the intermediate He-sdOB LS IV−14°116. So far it has been observed to be extremely enriched in two additional He-sdOBs: HE 2359−2844 (Naslim et al. 2013) and UVO 0825+15 (Jeffery et al. 2017b). We used their oscillator strengths for Y III 4039.602 Å and Y III 4040.112 Å to search for Y in HZ 44 and HD 127493. Both lines are weak and not detectable in our spectra of either star. We derive an upper limit of [Y/H] ≤ −5.3 ± 0.2 (14800 times solar) for HZ 44. Due to the lower S/N of the FEROS spectrum and the higher temperature in HD 127493, the upper limit derived from the same lines for HD 127493 is even weaker: [Y/H] ≤ −4.7 ± 0.3 (26000 times solar). None of the ultraviolet Y III lines for which Redfors (1991) computed oscillator strengths are strong enough to improve on this threshold. Unfortunately, we found no oscillator strength measurements for the resonance lines Y III 1000.563 Å and Y III 1006.587 Å that are listed in Morton (2000). A more complete analysis of Y in subdwarf stars would benefit from oscillator strengths for Y IV, which should be the dominant ionization stage at effective temperatures around 40 000 K.

Rauch et al. (2016a) have observed *molybdenum* in RE 0503−289. We use their atomic data for Mo V-VI and atomic data from the Kurucz line list for Mo IV to search for Mo in HZ 44. Mo IV λλ 965.485, 966.638 Å and Mo V λλ 939.248, 1127.101 Å would fit well with [Mo/H] = −6.4 (2500 times solar). Because of weakness of these lines and the generally incomplete model in the FUSE region, we adopt an upper limit of [Mo/H] ≤ −6.2 ± 0.4 (4000 times solar). Several lines in the IUE spectrum support this upper limit, e. g. Mo V λλ 1586.898, 1590.414, 1774.317 Å and Mo IV 1929.211 Å.

Mo V λλ 1586.898, 1590.414, 1653.541 1661.215 1774.317 Å exclude abundances higher than [Mo/H] ≤ −6.1 ± 0.4 (2200 times solar) in HD 127493.

Werner et al. (2018) have recently measured the photospheric *antimony* abundance in two DO white dwarfs, RE 0503−289 and PG 0109+111. Both stars are chemically peculiar, with strong enrichment of trans-iron elements.

Despite blends with unidentified lines in FUSE and the low resolution of IUE, we were able to set the upper limit on the Sb abundance in HZ 44 to [Sb/H] ≤ −8.0 ± 0.5 (470 times solar), which is well below the extreme enrichment observed in the two aforementioned white dwarfs. This upper limit is based on three lines: Sb IV 1042.190 Å (blended with Cr IV), Sb V 1104.23 Å and Sb V 1226.001 Å. Sb V 1104.23 Å even fits well at this abundance.
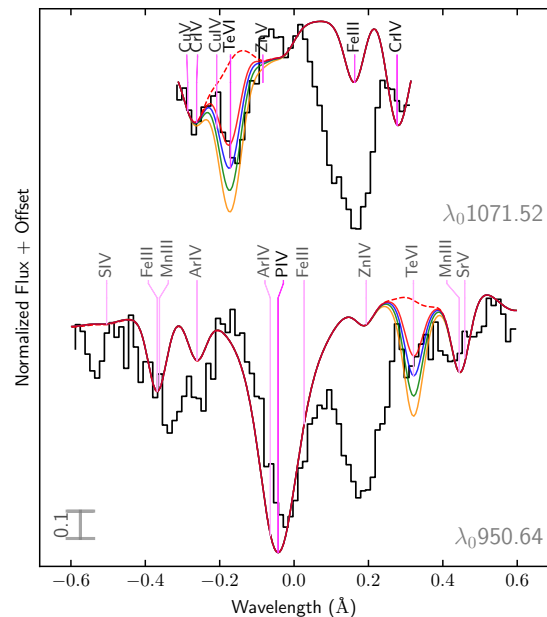


**Figure 20.** Te VI resonance lines in the FUSE spectrum of HZ 44. In red: a model with [Te/H] = −7.9, dashed without Te. In blue: [Te/H] = −7.5. In green: [Te/H] = −7.1. In orange: [Te/H] = −6.7.

Zhang et al. (2013) have computed oscillator strengths for *tellurium* II-III, including UV and optical lines. However, since the Te III population numbers are low in HZ 44, none of these lines are visible. Rauch et al. (2017b) provide oscillator strengths for Te VI lines, including the resonance lines Te VI λλ 951.021, 1071.414 Å, which are visible in HZ 44 (see Fig. 20). They are best fit at an abundance of [Te/H] = −7.5 ± 0.4 (100 times solar). However, due to the weakness of the

lines we only adopt an upper limit of [Te/H] = −7.1 ± 0.4 (250 times solar). The Te v 1281.670 Å resonance line listed in Morton (2000); Pinnington et al. (1985a) supports this upper limit.

We use oscillator strengths for *xenon* IV-v from Rauch et al. (2017a) provided on the TOSS website to search for Xe in HZ 44. Most Xe lines in the FUSE spectrum of HZ 44 are blended with unidentified lines. The resonance lines Xe IV λλ 935.251, 1003.373 Å and Xe v λλ 936.284, 945.248 Å allow us to set an upper limit of [Xe/H] ≤ −7.3 ± 0.4 (140 times solar). The actual Xe abundance in HZ 44 might be close to our upper limit, since the additional opacity improves the fit for many lines. However, the only line that could be identified as unblended Xe is Xe v 936.284 Å.

*Thorium* is the heaviest element for which we found atomic data. Th is interesting since it is not produced through the s-process and can be used for age determination because of its radioactivity. Safronova & Safronova (2013) have calculated atomic properties of 24 low-lying states in the Th IV ion. Atomic data for Th III is published in Safronova et al. (2014), but could not be used here since all transitions with calculated oscillator strengths lie in the infrared region. Even at a relatively low abundance of [Th/H] = −8.5 (1400 times solar), our models predict several Th IV lines with estimated equivalent widths up to 30 mÅ in the UV range. In particular, the non-detection of Th IV 983.140 Å (which falls conveniently on one of the few points of pseudo-continuum in the FUSE spectrum of HZ 44), Th IV 1140.612 Å (in the wing of a well-modeled Si III line), and Th IV 1682.213 Å allow us to set the upper limit for the photospheric Th abundance in HZ 44 to [Th/H] ≤ −8.0 (4600 times solar). We derive an upper limit of [Th/H] ≤ −7.8 ± 0.3 (3200 times solar) from Th IV λλ 4413.576, 5420.380, 5841.397, 6019.151 Å in the FEROS spectrum of HD 127493.

## 5.9   Undetected elements without upper limits

We also searched for predicted lines of Sc, In, Ba, Tl, and Bi in the ultraviolet and optical spectra of HZ 44. The results are negative or inconclusive.

The strongest *scandium* lines in the model of HZ 44 are the resonance line Sc III 1610.194 Å and Sc III 1603.064 Å. Both lines are weak in the model, even at a high abundance of −5 dex relative to hydrogen and are blended with both modeled and unidentified lines, so no meaningful upper limit could be determined.

Safronova et al. (2003) have calculated atomic properties along the silver isoelectronic sequence, including In III, Sn IV, and Sb V. They predict *indium* III lines from low-lying levels with high oscillator strengths in the IUE spectral region. However, the population number for In III is too low to set a meaningful upper limit in both HZ 44 and HD 127493.

*Barium* was observed in RE 0503−289 by Rauch et al. (2014b) who also provide atomic data for Ba v. The predicted Ba v lines are so weak in the model of HZ 44 that [Ba/H] = −5 (32000 times solar) is required before the strongest predicted lines in synthetic spectrum of HZ 44 (Ba v λλ 1097.415, 1103.140 Å) reach equivalent widths of 0.1 mÅ. It was therefore not possible to set a meaningful upper limit.

The strongest observable *bismuth* line in the spectrum of HZ 44 is by far Bi v 1139.549 Å. Since it is blended with an unidentified line, we can only derive an upper limit of [Bi/H] ≤ −8.5 (340 times solar). We consider this upper limit preliminary since it is based on a single, blended line in the FUSE spectrum.

Oscillator strengths along the gold isoelectronic sequence were computed by Safronova & Johnson (2004), including not only Pb IV but also *thallium* III. Similar to In III, the population number for Tl III is too low to set a meaningful upper limit in both HZ 44 and HD 127493.

## 5.10   Chemical composition summary

Figure 21 and Table 10 show our final abundance measurements for HZ 44 and HD 127493. The general abundance pattern is remarkably similar in both stars despite the ∼2500 K difference in effective temperature. Both stars show a strong CNO cycle pattern − nitrogen is enriched, while carbon and oxygen are depleted with respect to solar values. With the exception of Cl, all

**Table 10.** Abundances of HZ 44 and HD 127493[a] as derived from visual/UVA and FUV data as logarithmic number ratio of element X relative to hydrogen $\log N_X/N_H$, logarithmic mass fraction $\beta_X$, logarithmic number fraction $\epsilon_X$, and logarithmic solar fraction $\epsilon_X - \epsilon_{X,\odot}$. Uncertainties are given as standard deviation between single line fits. If an abundance was "fit by eye", uncertainties are estimated.

| Element | Abundance ($\log N_X/N_H$) | | Mass fraction ($\beta_X$) | | Particle fraction ($\epsilon_X$) | | Abundance ($\epsilon_X - \epsilon_{X,\odot}$) | |
| --- | --- | --- | --- | --- | --- | --- | --- | --- |
| | HZ 44 | HD 127493 | HZ 44 | HD 127493 | HZ 44 | HD 127493 | HZ 44 | HD 127493 |
| H | $0.00^{+0.00}_{-0.00}$ | $0.00^{+0.00}_{-0.00}$ | $-0.79^{+0.03}_{-0.03}$ | $-1.26^{+0.25}_{-0.21}$ | $-0.36^{+0.03}_{-0.03}$ | $-0.71^{+0.26}_{-0.22}$ | $-0.32^{+0.03}_{-0.03}$ | $-0.68^{+0.26}_{-0.22}$ |
| He | $0.10^{+0.05}_{-0.05}$ | $0.62^{+0.30}_{-0.30}$ | $-0.09^{+0.01}_{-0.01}$ | $-0.03^{+0.02}_{-0.01}$ | $-0.26^{+0.02}_{-0.02}$ | $-0.09^{+0.08}_{-0.04}$ | $0.85^{+0.02}_{-0.02}$ | $1.01^{+0.08}_{-0.05}$ |
| C | $-4.31^{+0.13}_{-0.13}$ | $-4.30^{+0.08}_{-0.08}$ | $-4.02^{+0.13}_{-0.14}$ | $-4.48^{+0.27}_{-0.26}$ | $-4.67^{+0.13}_{-0.13}$ | $-5.01^{+0.26}_{-0.25}$ | $-1.06^{+0.14}_{-0.15}$ | $-1.41^{+0.26}_{-0.26}$ |
| N | $-2.39^{+0.20}_{-0.20}$ | $-2.08^{+0.17}_{-0.17}$ | $-2.03^{+0.20}_{-0.21}$ | $-2.19^{+0.29}_{-0.32}$ | $-2.74^{+0.20}_{-0.21}$ | $-2.80^{+0.29}_{-0.32}$ | $1.46^{+0.21}_{-0.22}$ | $1.41^{+0.29}_{-0.33}$ |
| O | $-3.90^{+0.15}_{-0.15}$ | $<-4.30^{+0.20}$ | $-3.49^{+0.15}_{-0.16}$ | $<-4.35^{+0.30}$ | $-4.26^{+0.15}_{-0.15}$ | $<-5.01^{+0.30}$ | $-0.91^{+0.16}_{-0.17}$ | $<-1.67^{+0.30}$ |
| F | $<-5.00^{+0.40}$ | | $<-4.51^{+0.40}$ | | $<-5.36^{+0.40}$ | | $<2.12^{+0.45}$ | |
| Ne | $-3.23^{+0.11}_{-0.11}$ | $-2.90^{+0.20}_{-0.20}$ | $-2.72^{+0.11}_{-0.11}$ | $-2.85^{+0.30}_{-0.35}$ | $-3.59^{+0.11}_{-0.11}$ | $-3.61^{+0.30}_{-0.34}$ | $0.52^{+0.14}_{-0.16}$ | $0.49^{+0.31}_{-0.38}$ |
| Na | $-4.43^{+0.06}_{-0.06}$ | $<-3.40^{+0.30}$ | $-3.86^{+0.07}_{-0.07}$ | $<-3.29^{+0.36}$ | $-4.79^{+0.07}_{-0.07}$ | $<-4.11^{+0.36}$ | $1.01^{+0.08}_{-0.08}$ | $<1.68^{+0.36}$ |
| Mg | $-3.80^{+0.20}_{-0.20}$ | $-3.39^{+0.20}_{-0.20}$ | $-3.20^{+0.20}_{-0.20}$ | $-3.26^{+0.30}_{-0.35}$ | $-4.16^{+0.20}_{-0.20}$ | $-4.10^{+0.30}_{-0.34}$ | $0.28^{+0.20}_{-0.21}$ | $0.33^{+0.30}_{-0.35}$ |
| Al | $-4.86^{+0.11}_{-0.11}$ | $-4.53^{+0.10}_{-0.10}$ | $-4.21^{+0.11}_{-0.12}$ | $-4.35^{+0.27}_{-0.27}$ | $-5.21^{+0.11}_{-0.11}$ | $-5.24^{+0.27}_{-0.26}$ | $0.38^{+0.11}_{-0.12}$ | $0.34^{+0.27}_{-0.26}$ |
| Si | $-3.88^{+0.11}_{-0.11}$ | $-3.31^{+0.14}_{-0.14}$ | $-3.22^{+0.11}_{-0.11}$ | $-3.11^{+0.28}_{-0.29}$ | $-4.24^{+0.11}_{-0.11}$ | $-4.02^{+0.27}_{-0.29}$ | $0.29^{+0.12}_{-0.12}$ | $0.51^{+0.27}_{-0.29}$ |
| P | $-5.66^{+0.25}_{-0.25}$ | $<-4.70^{+0.30}$ | $-4.96^{+0.25}_{-0.25}$ | $<-4.46^{+0.36}$ | $-6.02^{+0.25}_{-0.25}$ | $<-5.41^{+0.36}$ | $0.61^{+0.25}_{-0.26}$ | $<1.21^{+0.36}$ |
| S | $-3.87^{+0.37}_{-0.37}$ | $-3.90^{+0.35}_{-0.35}$ | $-3.16^{+0.37}_{-0.38}$ | $-3.65^{+0.40}_{-0.51}$ | $-4.23^{+0.37}_{-0.37}$ | $-4.61^{+0.39}_{-0.50}$ | $0.69^{+0.37}_{-0.38}$ | $0.30^{+0.39}_{-0.50}$ |
| Cl | $-7.50^{+0.70}_{-0.70}$ | | $-6.74^{+0.70}_{-0.71}$ | | $-7.86^{+0.70}_{-0.70}$ | | $-1.32^{+0.71}_{-1.26}$ | |
| Ar | $-3.79^{+0.11}_{-0.11}$ | $<-3.60^{+0.20}$ | $-2.98^{+0.12}_{-0.12}$ | $<-3.25^{+0.30}$ | $-4.15^{+0.12}_{-0.12}$ | $<-4.31^{+0.30}$ | $1.49^{+0.17}_{-0.19}$ | $<1.32^{+0.31}$ |
| K | $-4.91^{+0.16}_{-0.16}$ | | $-4.11^{+0.16}_{-0.17}$ | | $-5.27^{+0.16}_{-0.16}$ | | $1.74^{+0.18}_{-0.20}$ | |
| Ca | $-3.90^{+0.24}_{-0.24}$ | $<-3.90^{+0.20}$ | $-3.08^{+0.24}_{-0.24}$ | $<-3.55^{+0.30}$ | $-4.25^{+0.24}_{-0.24}$ | $<-4.61^{+0.30}$ | $1.44^{+0.24}_{-0.25}$ | $<1.08^{+0.30}$ |
| Ti | $-4.56^{+0.22}_{-0.22}$ | $<-4.40^{+0.25}$ | $-3.67^{+0.22}_{-0.22}$ | $<-3.98^{+0.33}$ | $-4.92^{+0.22}_{-0.22}$ | $<-5.11^{+0.33}$ | $2.17^{+0.22}_{-0.23}$ | $<1.97^{+0.33}$ |
| V | $<-4.80^{+0.40}$ | $<-6.00^{+0.40}$ | $<-3.88^{+0.40}$ | $<-5.55^{+0.43}$ | $<-5.16^{+0.40}$ | $<-6.71^{+0.43}$ | $<2.95^{+0.40}$ | $<1.39^{+0.44}$ |
| Cr | $-4.40^{+0.30}_{-0.30}$ | $-3.90^{+0.30}_{-0.30}$ | $-3.47^{+0.30}_{-0.30}$ | $-3.44^{+0.36}_{-0.45}$ | $-4.76^{+0.30}_{-0.30}$ | $-4.61^{+0.36}_{-0.44}$ | $1.64^{+0.30}_{-0.31}$ | $1.78^{+0.36}_{-0.45}$ |
| Mn | $-4.90^{+0.40}_{-0.40}$ | $<-5.50^{+0.30}$ | $-3.95^{+0.40}_{-0.40}$ | $<-5.02^{+0.36}$ | $-5.26^{+0.40}_{-0.40}$ | $<-6.21^{+0.36}$ | $1.35^{+0.40}_{-0.41}$ | $<0.39^{+0.36}$ |
| Fe | $-4.00^{+0.25}_{-0.25}$ | $-2.82^{+0.12}_{-0.12}$ | $-3.04^{+0.25}_{-0.25}$ | $-2.33^{+0.27}_{-0.28}$ | $-4.36^{+0.25}_{-0.25}$ | $-3.53^{+0.27}_{-0.27}$ | $0.18^{+0.25}_{-0.26}$ | $1.00^{+0.27}_{-0.28}$ |
| Co | $-5.60^{+0.50}_{-0.50}$ | $-5.30^{+0.30}_{-0.30}$ | $-4.62^{+0.50}_{-0.50}$ | $-4.78^{+0.36}_{-0.51}$ | $-5.96^{+0.50}_{-0.50}$ | $-6.01^{+0.36}_{-0.44}$ | $1.09^{+0.50}_{-0.53}$ | $1.03^{+0.36}_{-0.47}$ |
| Ni | $-4.05^{+0.15}_{-0.15}$ | $-3.61^{+0.13}_{-0.13}$ | $-3.07^{+0.15}_{-0.16}$ | $-3.10^{+0.28}_{-0.29}$ | $-4.41^{+0.15}_{-0.15}$ | $-4.33^{+0.27}_{-0.28}$ | $1.41^{+0.16}_{-0.16}$ | $1.49^{+0.27}_{-0.29}$ |
| Cu | $-5.80^{+0.40}_{-0.40}$ | $<-6.10^{+0.40}$ | $-4.79^{+0.40}_{-0.40}$ | $<-5.55^{+0.43}$ | $-6.16^{+0.40}_{-0.40}$ | $<-6.81^{+0.43}$ | $1.69^{+0.40}_{-0.41}$ | $<1.03^{+0.43}$ |
| Zn | $-5.70^{+0.20}_{-0.30}$ | $-5.30^{+0.30}_{-0.30}$ | $-4.67^{+0.20}_{-0.30}$ | $-4.74^{+0.36}_{-0.45}$ | $-6.06^{+0.20}_{-0.30}$ | $-6.01^{+0.36}_{-0.44}$ | $1.42^{+0.20}_{-0.31}$ | $1.46^{+0.36}_{-0.46}$ |
| Ga | $-6.00^{+0.50}_{-0.50}$ | $<-6.40^{+0.40}$ | $-4.95^{+0.50}_{-0.51}$ | $<-5.81^{+0.43}$ | $-6.36^{+0.50}_{-0.50}$ | $<-7.11^{+0.43}$ | $2.64^{+0.50}_{-0.54}$ | $<1.88^{+0.44}$ |
| Ge | $-5.90^{+0.30}_{-0.30}$ | $-5.00^{+0.40}_{-0.40}$ | $-4.83^{+0.30}_{-0.30}$ | $-4.39^{+0.43}_{-0.57}$ | $-6.26^{+0.30}_{-0.30}$ | $-5.71^{+0.43}_{-0.56}$ | $2.13^{+0.31}_{-0.34}$ | $2.67^{+0.44}_{-0.61}$ |
| As | $-7.40^{+0.40}_{-0.40}$ | | $-6.31^{+0.40}_{-0.40}$ | | $-7.76^{+0.40}_{-0.40}$ | | $1.98^{+0.40}_{-0.41}$ | |
| Se | $<-6.30^{+0.40}$ | | $<-5.19^{+0.40}$ | | $<-6.66^{+0.40}$ | | $<2.04^{+0.40}$ | |
| Kr | $<-5.20^{+0.60}$ | $<-4.80^{+0.40}$ | $<-4.07^{+0.60}$ | $<-4.13^{+0.43}$ | $<-5.56^{+0.60}$ | $<-5.51^{+0.43}$ | $<3.23^{+0.60}$ | $<3.27^{+0.43}$ |
| Sr | $<-5.10^{+0.60}$ | $<-4.90^{+0.30}$ | $<-3.95^{+0.60}$ | $<-4.21^{+0.36}$ | $<-5.46^{+0.60}$ | $<-5.61^{+0.36}$ | $<3.71^{+0.60}$ | $<3.55^{+0.36}$ |
| Y | $<-5.30^{+0.20}$ | $<-4.70^{+0.30}$ | $<-4.14^{+0.20}$ | $<-4.01^{+0.36}$ | $<-5.66^{+0.20}$ | $<-5.41^{+0.36}$ | $<4.17^{+0.20}$ | $<4.41^{+0.36}$ |
| Zr | $-5.92^{+0.19}_{-0.19}$ | $<-5.30^{+0.20}$ | $-4.75^{+0.19}_{-0.20}$ | $<-4.60^{+0.30}$ | $-6.28^{+0.19}_{-0.19}$ | $<-6.01^{+0.30}$ | $3.18^{+0.19}_{-0.20}$ | $<3.44^{+0.30}$ |
| Mo | $<-6.20^{+0.40}$ | $<-6.10^{+0.40}$ | $<-5.01^{+0.40}$ | $<-5.37^{+0.43}$ | $<-6.56^{+0.40}$ | $<-6.81^{+0.43}$ | $<3.60^{+0.40}$ | $<3.34^{+0.44}$ |
| Sn | $-6.90^{+0.40}_{-0.40}$ | $<-6.60^{+0.40}$ | $-5.61^{+0.40}_{-0.40}$ | $<-5.78^{+0.43}$ | $-7.26^{+0.40}_{-0.40}$ | $<-7.31^{+0.43}$ | $2.74^{+0.40}_{-0.44}$ | $<2.68^{+0.44}$ |
| Sb | $<-8.00^{+0.50}$ | | $<-6.70^{+0.50}$ | | $<-8.36^{+0.50}$ | | $<2.67^{+0.50}$ | |
| Te | $<-7.10^{+0.40}$ | | $<-5.78^{+0.40}$ | | $<-7.46^{+0.40}$ | | $<2.40^{+0.40}$ | |
| Xe | $<-7.30^{+0.40}$ | | $<-5.97^{+0.40}$ | | $<-7.66^{+0.40}$ | | $<2.14^{+0.40}$ | |
| Pb | $-5.89^{+0.09}_{-0.09}$ | $-5.65^{+0.40}_{-0.40}$ | $-4.36^{+0.09}_{-0.10}$ | $-4.59^{+0.43}_{-0.57}$ | $-6.25^{+0.09}_{-0.10}$ | $-6.36^{+0.43}_{-0.56}$ | $4.04^{+0.13}_{-0.15}$ | $3.92^{+0.44}_{-0.61}$ |
| Th | $<-8.00^{+0.30}$ | $<-7.80^{+0.30}$ | $<-6.42^{+0.30}$ | $<-6.69^{+0.36}$ | $<-8.36^{+0.30}$ | $<-8.51^{+0.36}$ | $<3.66^{+0.31}$ | $<3.50^{+0.36}$ |

**Notes.** [a] He abundance from Hirsch (2009).

elements with $11 \leq Z \leq 20$ are enriched in HZ 44. Ne is enriched by a factor of 3 in both stars. The abundance of Mg, Al, and Si is similar in HD 127493 and HZ 44, S is slightly more abundant

in HZ 44. At a measured abundance of $148^{+98}_{-61}$ times solar, Ti IV lines are very strong in the UVA spectrum of HZ 44. In contrast, the Ti lines covered by our FEROS spectrum of HD 127493 are weak and set the upper limit for the Ti abundance to $94^{+105}$ times solar. Co and Ni have very similar abundances in both stars: they are about 30 times enriched compared to solar values. Mn and Cu could not be detected in HD 127493, indicating that they are less abundant than in HZ 44. Similar to other sdOB stars, Fe is the least enriched element in the iron group in HZ 44 (~1.5 times solar). In HD 127493, Fe is more abundant than in HZ 44 at ~10 times solar, but still less than other Fe-group elements. The Zn abundance in both stars is similar to their Ni abundance, between 25 and 30 times solar. While the Ge abundances in HD 127493 (~470 times solar) and HZ 44 (~140 times solar) are similar considering uncertainties, the Ga abundance in HD 127493 ($\lesssim$ 75 times solar) is lower than in HZ 44 (~440 times solar). As is enriched by a factor of about 100 in HZ 44. Interestingly, HZ 44 is one of the few stars that show Zr IV and Pb IV lines in their optical spectrum. As far as we know Zr IV has so far been identified in the optical spectrum of two intermediate He-sdOBs, LS IV−14° 116 and HE 2359-2844 (Naslim et al. 2011, 2013). Zr is enriched to about 1500 times solar in HZ 44, which is not excluded also in HD 127493. The measured Sn enrichment in HZ 44 is moderate in comparison, about 550 times solar. Interestingly the measured Pb abundance in both stars is almost identical; they are about 10000 times enriched. This enrichment is significantly lower for other heavy elements in HZ 44. In particular Xe and Te are less than 500 times enriched in HZ 44.

## 5.11 Comparison with literature

The only previous metal analysis of HZ 44 was performed by Peterson (1970) using the curve-of-growth method. Their results for C, N, O, Ne, Mg, Al, Si, and S are consistent with the values presented here considering 1-$\sigma$ uncertainties. Only their H abundance (based on early ATLAS model atmospheres) and Fe abundance (based on three weak optical Fe III lines with at the time uncertain oscillator strengths) are overestimated compared to ours.

Peterson (1970) also performed a curve-of-growth analysis of optical spectra for HD 127493 (including C, N, Mg, and Si) that agrees well with the abundances derived here. A similar analysis was performed by Tomley (1970); his abundance results for C and Ne are higher by about 1 dex, while the abundances of N, Mg, and Si match within the respective uncertainties. C and Si abundance determinations from early NLTE models by Bauer & Husfeld (1995) are higher by ~0.5 dex whereas their N and Mg abundances match well. The C and N abundances derived by Hirsch (2009) are consistent with our results.

Figure 28 in the appendix visualizes the comparison of abundances determined in this work with literature values for HZ 44 and HD 127493.

## 5.12 Discussion

The strong overabundances of heavy elements found for HZ 44, HD 127493, and several iHe-sdOB stars are generally believed to be caused by atmospheric diffusion processes (radiative levitation). On the other hand, it is not plausible to assume that diffusion creates an abundance pattern of C, N, O, and Ne that mimics the nucleosynthesis pattern so well. We shall first discuss the evidence for diffusion process and compare the abundance patterns to that of other hot compact stars. Then we shall revisit the nuclear synthesis aspect and discuss implications for the evolutionary status.

### 5.12.1 Diffusion

Diffusion refers to the equilibrium between gravitational settling and radiative levitation. While heavy elements (like Fe) are pulled down by gravity, their large opacities in the UV region lead to an opposing force due to radiative pressure. This force is limited by the saturation of spectral lines at high abundances. A different equilibrium abundance is reached for each element and each depth in the atmosphere, depending on the abundance before diffusion/mixing and the strength

and wavelengths of the element's absorption lines.

Michaud et al. (2011) have studied the effects of non-equilibrium diffusion and radiative levitation on element abundances up to Ni for sdB stars on the horizontal branch (up to $T_{\text{eff}} \approx 30\,000$ K), but not sdOs. To match the iron abundances observed in sdBs by Geier et al. (2010) and later Geier (2013), they required some process to dampen the effect of radiative levitation. They suggested a turbulent surface mixing zone during the HB evolution that includes the outer $\sim 10^{-7.5}$ M$_\odot$ of the envelope. Alternatively, a stellar wind may also damp diffusion processes at the surface if the mass-loss rate is appropriate. Similar to the sdOs discussed here, the photospheric iron abundance in sdBs is approximately solar. This low Fe enhancement is favored by the high absolute abundance in the photosphere and the consequent line saturation. Since heavy elements, such as Zr and Pb, are usually less abundant in absolute terms, a stronger enrichment with respect to the Sun due to radiative levitation is expected.

Models by Michaud et al. (2011) can not explain the He-enrichment and CNO-cycle pattern observed in some sdBs (and the sdO/Bs discussed here) since they use approximate methods for the He-flash. Byrne et al. (2018) have preformed similar calculations for post common envelope sdBs from the top of the RGB to the zero age HB with an improved treatment of the He-flash using the Mesa[10] code. Their delayed He-flash models produced He-rich atmospheres with C and N predicted to be enriched and O to be depleted for sdBs on the ZAHB. The abundances of other elements are similar to those of Michaud et al. (2011) but both models are not well-suited for the sdO/Bs discussed here. Detailed sdO evolutionary models (e. g. through the HeWD-merger channel) including diffusion of heavy elements beyond the iron group would be required to explain the observed abundance pattern. Unfortunately, the atomic data required for modeling diffusion of elements heavier than Ni is not available.

### 5.12.2  Examples of diffusion in hot, compact stars

If the abundance pattern of sdOBs were determined by diffusion alone one would expect similar abundances for stars with similar $\log g$ and $T_{\text{eff}}$. However, this is not what is observed, especially for low-mass elements like H and He or C, N, and O. There is significant diversity of surface He abundances in sdOs, ranging from $10^{-3}$ to $10^{+4}$ times solar. Stroeer et al. (2007) classified He-sdOs in three classes: N-rich, C-rich, and CN-rich stars. This variety of abundances is a result of different nuclear burning and mixing during the stars' evolutionary history.

In the following, we compare the abundance pattern of HZ 44 and HD 127493 with literature abundances of four other stars that are affected by diffusion to varying degrees: CD–31° 4800 and UVO 0825+15 (see Fig. 21), as well as Feige 110 and RE 0503−289 (see Fig. 22). The abundances of all comparison stars are listed in Table 14 in the appendix.

CD–31° 4800 is a He-sdO star with $T_{\text{eff}} = 42\,230$ K, $\log g = 5.60$, and $\log N_{\text{He}}/N_{\text{H}} = 2.75$ (Schindewolf et al. 2018). Despite its extreme H-deficiency, its metal abundances are very similar to HD 127493. Its shows the same CNO-cylce pattern, intermediate elements from Ne to S are equally enriched, and even the Fe and Ni abundances are similar. However, a comparison of its FUSE and IUE spectra with models including heavy elements revealed that the As and Pb abundances are drastically lower compared to HD 127493 and HZ 44. This lack of strong enhancement and the low H abundance indicate that diffusion is less important in CD–31° 4800.

UVO 0825+15 is an entirely different case – in this heavy-metal enhanced intermediate He-sdOB, the effects of diffusion seem to be more pronounced. We selected it for our comparisons since it is the only known C-deficient heavy-metal enhanced sdOB next to LS IV−14°116[11]. With $T_{\text{eff}} = 38\,900$ K, $\log g = 5.97$, and $\log N_{\text{He}}/N_{\text{H}} = -0.6$ (Jeffery et al. 2017b), UVO 0825+15 has a temperature and surface gravity similar to those of HZ 44 but is less enriched in helium. Its abundance pattern is also similar to HZ 44 and HD 127493 in that the CNO-cycle pattern is evident and lead is equally enriched. However, the abundances of some specific elements differ significantly: Mg and Si are less abundant by $\sim$1 dex, while Cl is about 2 dex more abundant in

---

[10]Modules for Experiments in Stellar Astrophysics, http://mesa.sourceforge.net/

[11]which is, however, colder ($T_{\text{eff}} = 35\,000$ K; Green et al. 2011)
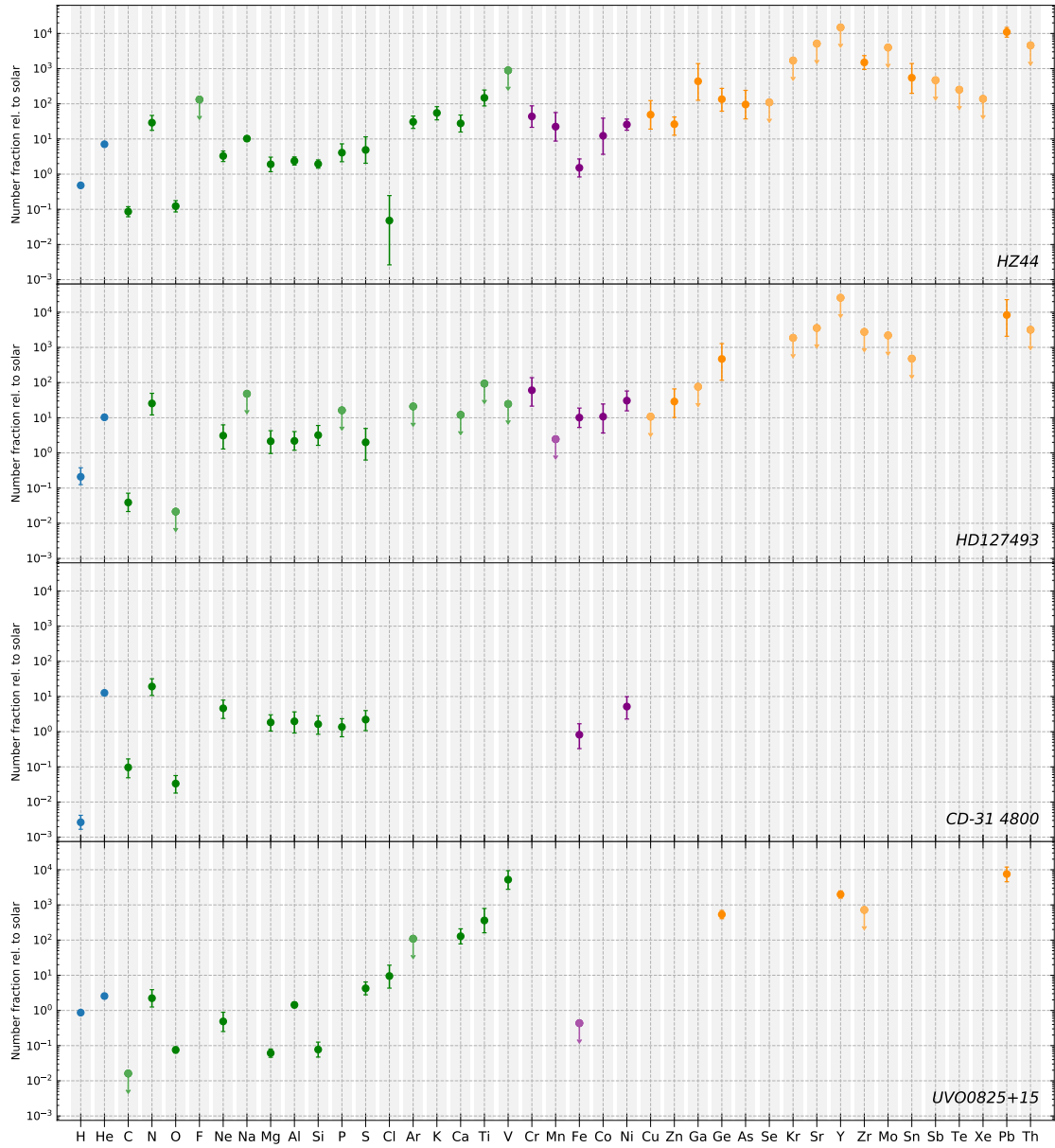
**Figure 21.** Abundance pattern of HD 127493 and HZ 44 with respect to solar composition. Results for the He-sdO CD–31 4800 (Schindewolf et al. 2018) and UVO 0825+15 (Jeffery et al. 2017b), an intermediate He-sdOB, are shown for comparison. Light elements (23 ≤ Z) are marked by green symbols, iron-peak elements (24 ≤ Z ≤ 28) in purple, and heavier elements (Z ≥ 29) in orange. Upper limits are marked with an arrow and less saturated colors. The abundance pattern is very similar in both stars. We observe the typical CNO bi-cycle abundance pattern – N is enriched, while C and O are depleted with respect to solar values. In addition, almost all elements heavier than Ar are enriched, most notably Zr and Pb in HZ 44.
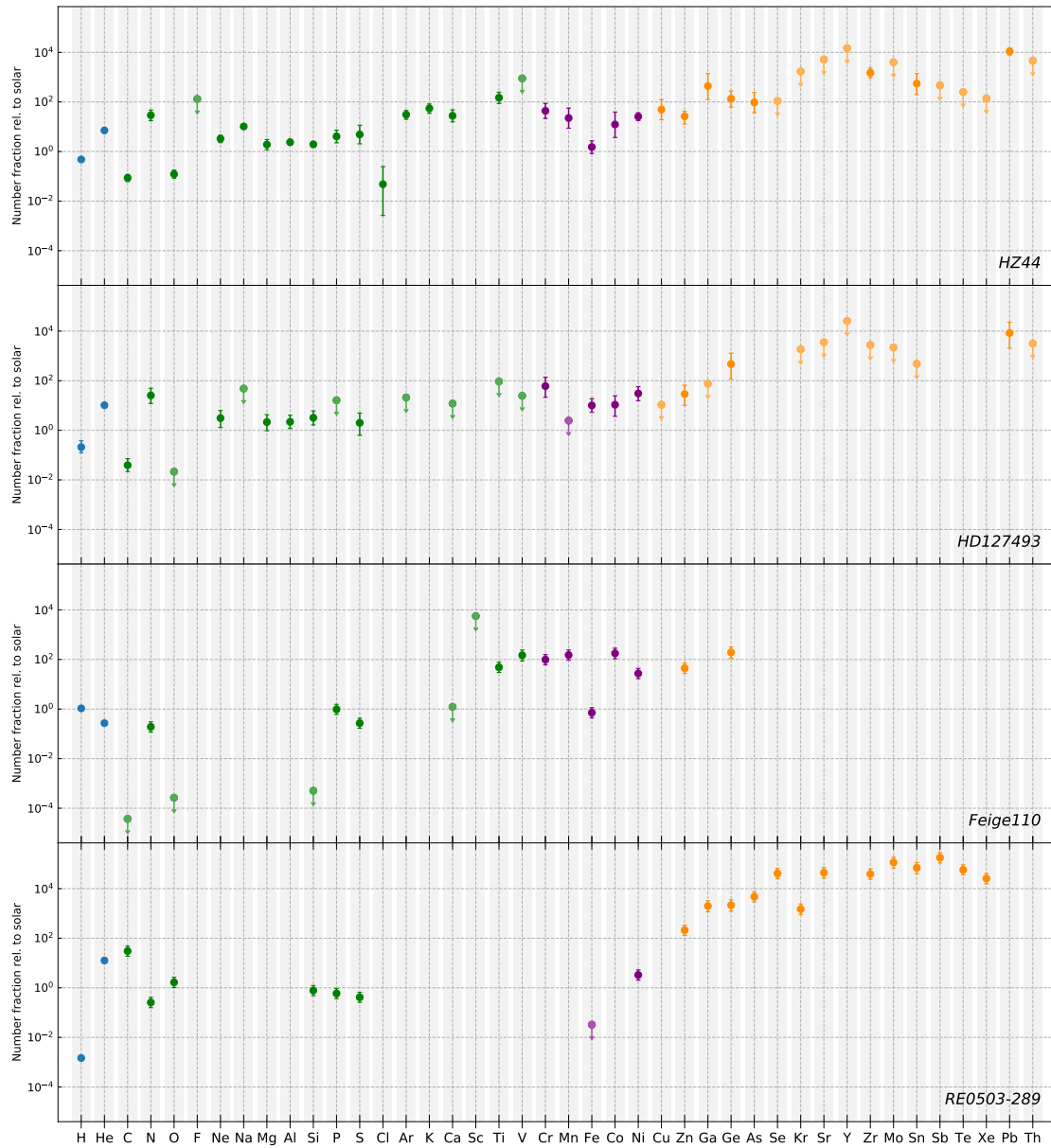
**Figure 22.** Same as Fig. 21, but with results for the He-deficient sdO Feige 110 (Rauch et al. 2014a) and the DO WD RE 0503−289 (Rauch et al. 2017b; Werner et al. 2018, and references therein). The scales differ from those in Fig. 21.

UVO 0825+15.

Feige 110 is a H-rich sdO star with $T_{\text{eff}} = 47\,250$ K, $\log g = 6.0$, and $\log N_{\text{He}}/N_{\text{H}} = -1.66$ (Rauch et al. 2014a). The enrichment in elements from Ti to Ge, as determined by Rauch et al. (2014a), is similar to the intermediate He-sdOBs discussed here. However, Si is significantly depleted with an abundance more than than 3 dex lower than in HZ 44, and the extremely low C abundance can not be explained with the CNO-cycle equilibrium.

RE 0503−289 is among the compact stars that are most effected by diffusion (compare Sect. 4). It is a DO WD with $T_{\text{eff}} = 70\,000$ K and $\log g = 7.5$ (Dreizler & Werner 1996; Rauch et al. 2012) and it shows a different abundance pattern compared to intermediate He-sdOs. The enrichment in heavy elements is significantly more pronounced than in HZ 44 and HD 127493, while the Fe abundance is sub-solar. Rauch et al. (2016a) calculated diffusion models for RE 0503−289 including several heavy metals and predicted strong abundance enhancements in the line-forming region. Despite strong stratification, the predicted abundance pattern was in qualitative agreement with abundances derived from their chemically homogeneous TMAP models.

The importance of diffusion of heavy elements in hot subdwarfs seems to be linked to their helium abundance. The extremely He-rich CD−31° 4800 is less affected by diffusion compared to intermediate He-sdOs and sdBs. If one assumes a common evolutionary path for these stars, starting from a He-rich phase after the He-flash, the observed behavior could be explained by an earlier onset of radiative levitation for heavy elements than the gravitational settling of He.

### 5.12.3 Nuclear synthesis and evolutionary status

The creation of sdO/Bs with intermediate He abundances (10%–90% by number) through merging He-WDs with low-mass MS stars was investigated by Zhang et al. (2017). In these models, subdwarfs with intermediate He-rich atmospheres represent a short ($< 5$ Myr) phase after the He-flash is ignited during the merger. The initially He-rich atmosphere of the merger remnant transforms into a H-rich one as the heavier He diffuses downward (gravitational settling) until the atmosphere is H-rich when the zero-age horizontal branch (ZAHB) is reached. The same process is predicted in accretion-based HeWD+HeWD mergers (Zhang & Jeffery 2012) that can also reproduce the He abundance in intermediate He-sdOs.

A known problem is that merger calculations predict a fast surface rotation. Schwab (2018) have calculated post-HeWD+HeWD merger models with initial conditions taken from hydrodynamic merger calculations. They find that merger products have $v_{\text{rot}} \geq 30$ km s$^{-1}$ once they appear as hot subdwarfs. This rotation is usually not observed in single sdBs (Geier & Heber 2012) and Hirsch (2009) finds N-rich He-sdOs (such as HZ 44 and HD 127493) to have $v_{\text{rot}}$ similar to sdBs. For individual stars, this can be explained by a small inclination $i$ (which leads to a small $v_{\text{rot}} \sin i$). However, with increasing evidence for slowly rotating (intermediate) He-sdOs, it seems likely that additional physics is needed to match the observations (Schwab 2018). Alternatively, slowly-rotating sdOs and sdBs may be created through a different process altogether.

The observation of the CNO cycle pattern in HD 127493 and HZ 44 indicates that the CNO process must have been efficient in a H-burning shell or mixed from a sufficiently hot core in the stars' progenitor. In fact, the slow HeWD+HeWD merger model by Zhang & Jeffery (2012) is able to reproduce the CNO pattern observed in HZ 44 and HD 127493 well except for the O abundance that is predicted to be somewhat higher than the observation. This may be an indication that O has been processed to Ne through the $\alpha$ capture $^{16}_{8}\text{O}(\alpha, \gamma)^{20}_{10}\text{Ne}$. In HeWD+MS merger models presented by Zhang et al. (2017), temperatures high enough for $^{18}_{8}\text{O}(\alpha, \gamma)^{22}_{10}\text{Ne}$ burning are reached following the first He-flash. However, the processed material is not always mixed to the surface. The fact that the He, C, N, O, and Ne abundances in He-sdOs can be explained by nuclear synthesis indicates that diffusion is inefficient for these light elements.

Since the dominant effect of diffusion is thought to work similarly in sdO stars with similar atmospheric parameters, the question remains why some of them show extreme enrichment in Zr and Pb, while others do not. A possible explanation is that these elements were created in the stars' progenitors. Heavy elements like Zr and Pb are produced mainly in the s-process, which

is thought to be efficient in AGB stars. However, diffusion calculations for these elements are required before conclusions on possible AGB progenitors of heavy-metal enriched intermediate He-sdOs can be made. Also, C-enrichment would be expected from thermally pulsing AGB stars.

## 5.13 Summary and conclusions

We have performed a detailed spectroscopic analysis of the two peculiar intermediate He-sdOs HZ 44 and HD 127493. Despite a temperature difference of more than 2000 K the stars have very similar abundance patterns. SED-fits combined with parallax distances for both stars result in masses that are consistent with the canonical subdwarf mass of $0.47\,M_\odot$ within 1-$\sigma$ uncertainty. No indication of binarity was found for either star. Our main focus was the determination of photospheric metal abundances, including heavy metals. We find the abundance pattern in both stars to be very similar. They show a typical CNO-cycle pattern and enrichment of intermediate-mass elements ($10 \leq Z \leq 30$, except Cl) with respect to solar values. As observed in other sdO and sdB stars, Fe is less enriched than other iron-group elements. Heavier elements such as Ga, Ge, and As were found to be enriched in the order of 100 times solar. Most interestingly, the abundance of Zr could be measured from optical lines in HZ 44, and turned out to be more than 1000 times solar. The abundance of Pb was measured in both HZ 44 and HD 127493 to be even more strongly enriched, about 10000 times solar in both stars. Sn is less enriched in HZ 44 at about 400 times solar. We also determined upper limits for several other heavy elements. In particular Xe and Te are less than 500 times enriched in HZ 44. The strong enrichment of some heavy elements such as Pb and weaker enrichment in other (heavy) elements poses a challenge to diffusion theories. To improve the accuracy of our abundance measurements, additional atomic data are much-needed, in particular for heavy elements. Many lines in both optical and ultra-violet spectra remain unidentified. This is especially evident in the FUSE spectrum of HZ 44, where not only interstellar but also many photospheric lines are missing from our models. Some of those lines may belong to highly ionized heavy elements for which no atomic data are available. It would be favorable to collect all measurements and theoretical predictions of oscillator strengths and line wavelengths in an online database.

As of now, we are not able to fully explain the observed abundance pattern in intermediate He-sdOs. Evolutionary simulations for sdOs including diffusion for heavy elements and mixing during hot flasher/merger tracks would be required to interpret the abundance pattern. A better understanding of diffusion is required to relate the observed abundances to the evolution of the stars, for example the production of s-process elements on the AGB. Since pulsation was observed in other peculiar He-sdO/Bs (e. g. Feige 46 and LS IV −14°116), it would be interesting to search for pulsation in HZ 44 and HD 127493 as well.

# 6   Feige 46: a pulsating twin of LS IV–14°116

The procedure to model spectral lines of heavy elements developed for HZ 44 and HD 127493 can easily be applied to other stars of similar spectral type. One such star is Feige 46, an intermediate He-sdOB[12] very similar to the unique star LS IV−14°116.
LS IV−14°116 was found to be a multi-periodic pulsator by Ahmad & Jeffery (2005) and Green et al. (2011). Recently, Latour et al. (2019) found Feige 46 to be pulsating as well, with oscillation periods between about 40 minutes and one hour, similar to LS IV−14°116. The origin of these oscillations is not identified yet, but the $\epsilon$-mechanism (Battich et al. 2018) and $g$-modes due to the $\kappa$-mechanism driven by C/O opacity bumps (Saio & Jeffery 2019) have been suggested.

Another common feature between LS IV−14°116 and Feige 46 is their membership to the Galactic halo. Randall et al. (2015) found LS IV−14°116 to be on an eccentric and retrograde orbit around the center of the galaxy. Feige 46's orbit is highly eccentric as well, but aligned with the rotation of the galaxy (Latour et al. 2019). Since LS IV−14°116 is known to be extremely

---

[12] LS IV−14°116 has been previously referred to as a sdB star. Since the He II 4686 Å line is strong in both Feige 46 and LS IV−14°116, they will be referred to as sdOBs here.

enriched in Sr, Y, and Zr (Naslim et al. 2011), we decided to investigate the abundances in the similar Feige 46.

Our abundance analysis is based on an optical spectrum taken with CASPEC (see Drilling & Heber 1987 and Bauer & Husfeld 1995), an echelle spectrograph that was mounted at the Cassegrain focus of the ESO 3.6-meter telescope at La Silla Observatory. The spectrum covers the 3860 Å – 4840 Å range at a resolution of $R \approx 20\,000$ and has a S/N of about 45.

Fitting hydrogen and helium lines in the CASPEC spectrum results in atmospheric parameters of $T_{\mathrm{eff}}$ = 36240 K, $\log g$ = 6.10, and $\log N_{\mathrm{He}}/N_{\mathrm{H}}$ = −0.36. We used these parameters and metal abundances as determined for LS IV−14°116 by Naslim et al. (2011) as initial parameters for our model. The abundances were then estimated following the same method as described in Chapter 5. The final model includes in NLTE: H I, He I-II, C II-IV, N II-V, O II-VI, Mg II-V, Si II-IV, Fe II-V, Ni III-V, as well as an additional ion of the next higher stage for each element represented by its ground state only.
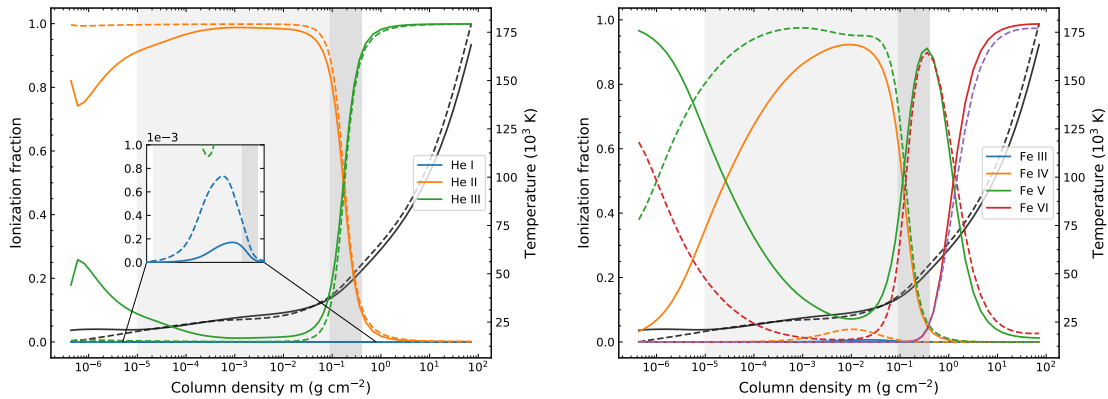


**Figure 23.** Ionization fractions for He (left) and Fe (right) in the final model atmospheres for HZ 44 (solid lines) and Feige 46 (dashed lines). The inset in the left panel magnifies the low He I population. The black curves show the temperature stratification of the two models. The dark grey area marks the continuum forming region, while the lighter grey area marks the range in which the strongest lines in the UV region are formed.

Figure 23 compares the ionization fractions of He and Fe in our models of Feige 46 and HZ 44, in addition to their temperature structures. Despite its higher $T_{\mathrm{eff}}$, the temperature in deep layers in the atmosphere of HZ 44 is actually lower than in Feige 46, even up to the continuum forming region. This is likely a result of the higher $\log g$ = 6.10 in Feige 46. However, all elements are generally more ionized in HZ 44. The decrease in temperature in Feige 46 at $m$ = $10^{-2}$ g cm$^{-2}$ is aligned with an increase in the abundance of Fe III and Ni III ions. This might be due to the following coupling: initially low temperatures in this region allow for a substantial amount of Fe/Ni III ions. Fe/Ni III ions have many lines in the UV region, where the flux is highest (compare Fig. 7), which block outgoing flux. This leads to the so-called back-warming and surface cooling effects. The higher opacity in the UV region requires a steeper temperature gradient in the region where the continuum originates. This results in higher temperatures in the continuum region and lower temperatures in the outer atmosphere, where photons escape from the atmosphere. This in turn increases the abundance of Fe/Ni III ions. Another interesting effect shown in Fig. 23 is that both HZ 44 and Feige 46 are hot enough that increasing their effective temperature would lead a decrease of He II in the line forming region.

## 6.1   Zirconium in the optical spectrum of Feige 46

Unlike the hotter stars HZ 44 and HD 127493, Feige 46 does not show the typical CNO-cycle pattern. Fitting optical C, N, and O lines (including the lines shown in Fig. 24) results instead in abundances of [C/H] = −2.94 ± 0.27, [N/H] = −3.41 ± 0.12, and [O/H] = −4.09 ± 0.23.
Figure 25 shows the three strongest Zr IV lines observed in the CASPEC spectrum of Feige 46.
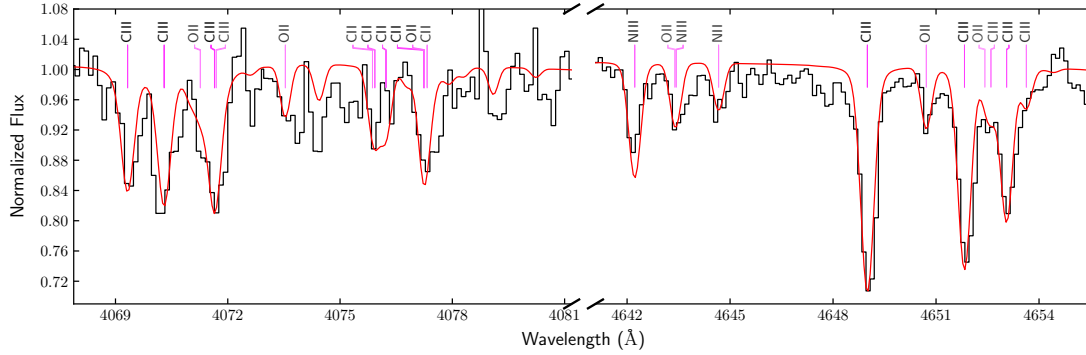
**Figure 24.** Two ranges in the CASPEC spectrum of Feige 46, showing C II-III, N II-III, and O II lines. The model (in red) has abundances of [C/H] = −2.94, [N/H] = −3.41, and [O/H] = −4.09.

Fitting these lines results in [Zr/H] = −4.99±0.11, which translates to the extreme overabundance of $20\,000^{+5900}_{-4700}$ times solar. For comparison, the Zr enrichment in LS IV−14°116 was found to be 8500 times solar by Naslim et al. (2011).
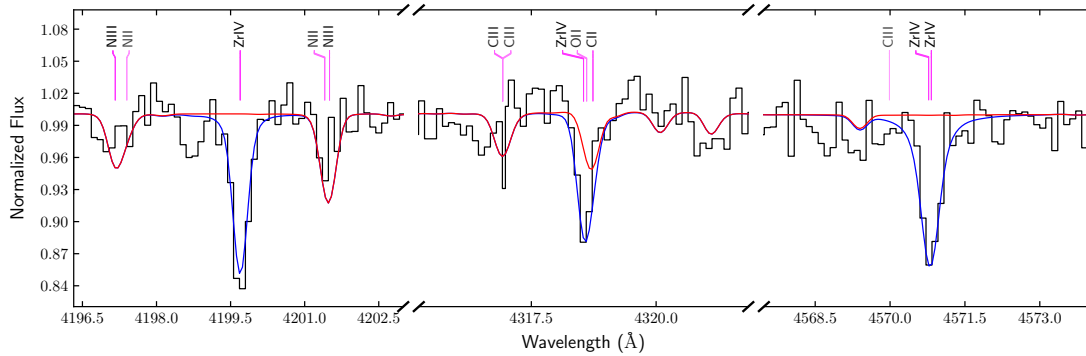


**Figure 25.** The strongest Zr IV lines in the CASPEC spectrum of Feige 46. In blue: a model with [Zr/H] = −5.06. In red: the same model, but without Zr.

Unfortunately, the quality of the CASPEC spectrum is not sufficient to measure the abundances of strontium or yttrium.

## 6.2   The GHRS spectrum of Feige 46

In addition to the optical spectrum, an ultraviolet GHRS spectrum of Feige 46 is also available. It covers the 1323 Å – 1518 Å range with a resolution of about 0.07 Å and lacks coverage in the 1359.1 Å – 1377.4 Å, 1414.1 Å – 1438.0 Å, and 1474.5 Å – 1482.5 Å ranges. Simultaneously fitting the many sharp metal lines in this region results in a projected radial velocity of $v_{\rm rot} \sin i = 11.6 \pm 2.6\,{\rm km\,s^{-1}}$ (uncertainty determined via bootstrapping).

S V 1501.763 Å sets the upper limit for sulfur to [S/H] ≤ −5.7 ± 0.3 (0.1 times solar). The strong Si IV $\lambda\lambda$ 1394, 1403 Å resonance lines and Si III 1501.87 Å are best fit at an abundance of [Si/H] = −5.91±0.11 ($2.9 \times 10^{-2}$ times solar). There are some strong Ti lines in GHRS spectrum of Feige 46, most notably Ti IV $\lambda\lambda$ 1451.739, 1467.343, 1469.191 Å, and Ti III 1455.195 Å. Fitting these lines gives an abundance of [Ti/H] = −5.69±0.15 (17 times solar). The iron abundance was determined to [Fe/H] = −4.65 ± 0.14 (0.5 times solar) by fitting seven 10 Å ranges, centered at $\lambda\lambda$ 1410, 1450, 1460, 1470, 1490, 1500, and 1510 Å. This approach may somewhat overestimate the abundance as not all the spectral lines observed in these ranges are included in our models (see Sect. 5.6.3). Thus some missing opacity might artificially be compensated by a higher Fe abundance during the fitting procedure. Indeed, visual inspection of the GHRS spectrum suggests an iron abundance closer to [Fe/H] ≈ −4.8. Fitting 14 ranges between 1323 Å and 1518 Å results in a nickel abundance of [Ni/H] = −4.54 ± 0.11 (13 times solar).
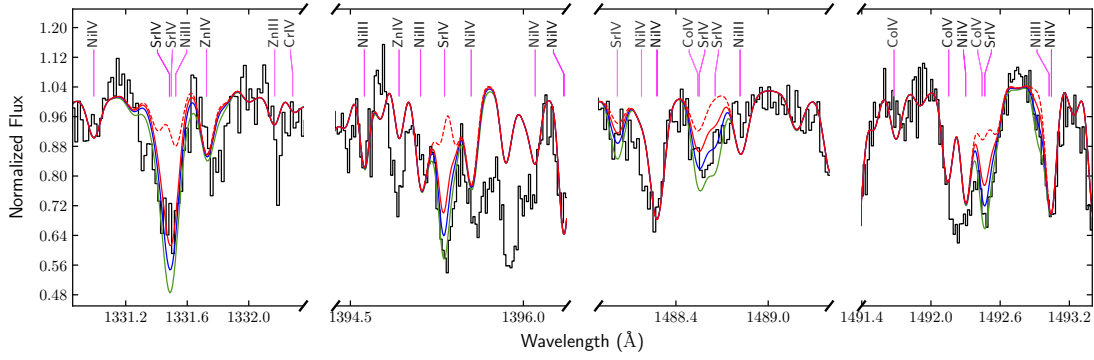
**Figure 26.** Some of the strongest Sr ɪᴠ lines in the GHRS spectrum of Feige 46. In red: a model with [Sr/H] = −4.8; dashed without Sr. In blue: the adopted abundance [Sr/H] = −4.4. In green: [Sr/H] = −4.0.

There are several strong Sr ɪᴠ lines in the GHRS spectrum of Feige 46, e. g. Sr ɪᴠ $\lambda\lambda$ 1331.129, 1338.087, 1394.944, and 1492.069 Å. Figure 26 shows some of the strongest Sr lines along with synthetic models. Visual comparison with synthetic spectra suggests an abundance of [Sr/H] = −4.4 ± 0.4 ($40\,000^{+61000}_{-25000}$ times solar). However, this extreme overabundance is not perfectly consistent between all lines. This might be due to non-LTE effects, but also due to inaccurate atomic data for some lines.

Figure 27 visualizes the very similar abundance patterns of Feige 46 and LS IV−14°116. A wider spectral coverage in the UV region and better S/N optical spectra of Feige 46 would additionally enable the abundance determination for germanium, yttrium, and lead, as well as the many other elements that were investigated in HZ 44 and HD 127493.
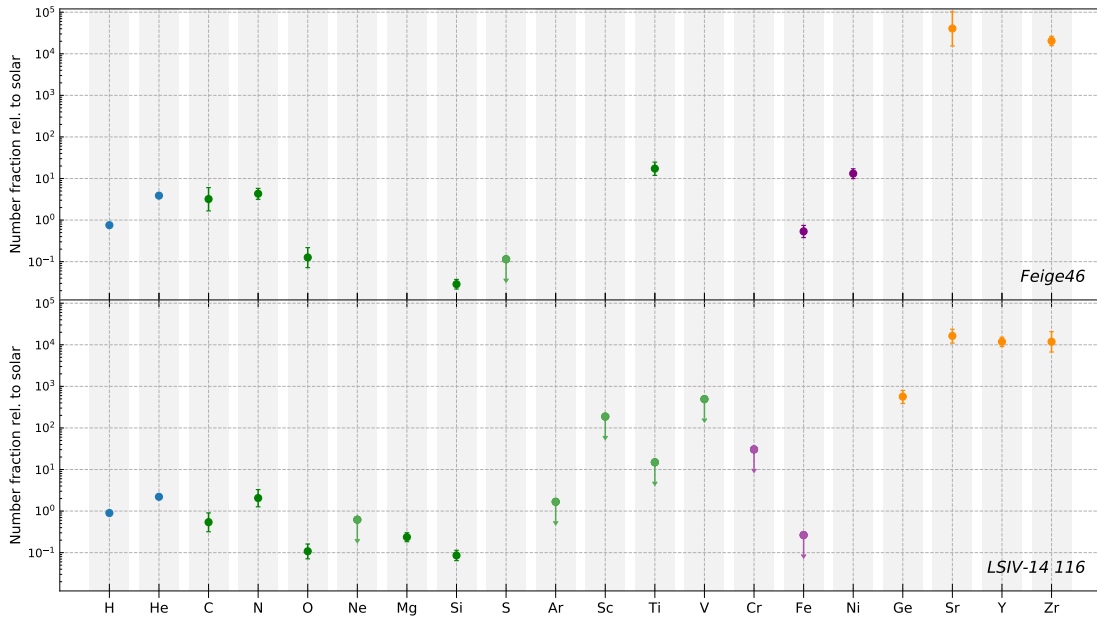


**Figure 27.** Abundance pattern of Feige 46 and LS IV−14°116 with respect to solar composition. The abundances for LS IV−14°116 are from Naslim et al. (2011).

# 7 Conclusions

The main part of this thesis consisted in the detailed abundance analysis of HD 127493 and HZ 44, two intermediately He-rich subdwarf stars. Particular attention was paid to the abundances of heavy metals, by studying both the ultraviolet and high-resolution optical spectra. In addition, a similar analysis was performed for the peculiar intermediate He-sdOB star Feige 46, although the observational data basis of this star is not as optimal as that of the two other stars. The analysis was based on non-LTE TLUSTY model atmospheres and SYNSPEC synthetic spectra that include millions of spectral lines. Atmospheric parameters for HD 127493 and HZ 44 were determined using a model grid that was built especially for the analysis of He-sdOs enriched in nitrogen. The following parameters were derived for HD 127493: $T_{\text{eff}} = 42\,070$ K, $\log g = 5.61$, and $\log N_{\text{He}}/N_{\text{H}}$ = 0.33, in good agreement with the parameters estimated by Hirsch (2009). As for HZ 44, we obtained $T_{\text{eff}} = 39\,096$ K, $\log g = 5.64$, and $\log N_{\text{He}}/N_{\text{H}} = 0.08$. Stellar masses were determined by combining atmospheric parameters, photometric data, and precise parallax distance measurements from the *Gaia* satellite. Both HD 127493 and HZ 44 were found to have a mass consistent with the canonical value for hot subdwarfs ($0.47\,M_\odot$).

To derive the abundances of elements heavier than zinc, the set of atomic data included in SYNSPEC was extended to cover the ionization stages present in the stars (including excitation and ionization energies and statistical weights). Atomic data for transitions of ionized heavy elements (most importantly wavelengths and oscillator strengths) were collected from several theoretical investigations. The updated atomic data and the synthetic spectra computed with SYNSPEC were tested by modeling the spectra of two well-studied white dwarfs, G191–B2B and RE 0503−289.

In total, the abundances of 28 metallic elements were determined in HZ 44, 14 in HD 127493, and 9 in Feige 46. Upper limits were derived for 14 additional elements in HZ 44 and 17 in HD 127493. All three stars were found to be extremely enriched in heavy metals with respect to the Sun. The high-quality optical HIRES spectrum of HZ 44 revealed zirconium and lead lines that were matched with overabundances of 1500 and 10 000 times solar, respectively. The lead abundance measured from the optical lines was further supported by the strength of Pb III-v lines in the FUSE and IUE spectra of HZ 44. To our knowledge, it was the first time that Pb v lines were modeled in a star. Many strong lines in the FUSE spectrum remained unidentified, very likely including additional transitions from trans-iron elements for which no atomic data are currently available. Although the optical spectrum of HD 127493 showed neither Zr nor Pb lines, the Pb IV 1313 Å resonance line seen in the UV spectrum revealed that Pb is enriched almost to the same degree as in HZ 44. Both stars are enriched in nitrogen, but depleted in carbon and oxygen, at a level consistent with predictions for hydrogen fusion in the CNO-cycle.

Feige 46 is similar to the prototypical iHe-sdOB LS IV−14°116, sharing its peculiar pulsation properties and membership to the galactic halo. This work found that Feige 46 also shares the extreme enrichment of zirconium that is characteristic for LS IV−14°116. An abundance of about 20 000 times solar was derived from the strong Zr IV lines present in the optical CASPEC spectrum of Feige 46. Strontium lines in its UV GHRS spectrum were used to estimate an enrichment in strontium that appears to be even more pronounced. Like LS IV−14°116, Feige 46 is enriched in carbon and nitrogen but depleted in oxygen. Fitting the GHRS spectrum showed Feige 46 to have a projected rotational velocity ($v_{\text{rot}} \sin i$) between 10 and 15 km s$^{-1}$, which is faster than the few other iHe-sdOBs for which $v_{\text{rot}} \sin i$ has been measured.

Both HD 127493 and HZ 44 are hotter than the other known "heavy-metal" subdwarfs, suggesting that such particular enhancement may be found across a broader temperature range than previously thought. Given that for most He-sdO/Bs only optical spectra are available, for example from the recent survey by Jeffery et al. (2017a), and that the optical zirconium and lead lines are weaker in hotter stars (caused by a shift toward higher ionization stages), a similar enrichment may remain undetected without the help of UV observations.

These overabundances in heavy elements are probably related to the effects of diffusion. A careful examination of the spectra of CD−31° 4800, a He-sdO, revealed that it does not share the extreme

overabundances of trans-iron elements seen in the iHe-sdOBs. Although the colder, hydrogen-rich sdBs are known to be enriched in Ge and Pb, that enrichment remains smaller than what is observed in iHe-sdOBs. A comprehensive understanding of the abundance patterns could be achieved by self-consistently treating the diffusion of heavy elements in stellar evolution models. This would help us understand why such extreme enrichment appears to be favored in the intermediately helium-rich sdOBs, and not in the He-sdOs or typical sdBs.

# 8 Bibliography

Ahmad A., Jeffery C. S., 2005, A&A, 437, L51

Ahmad A., Jeffery C. S., 2006, Baltic Astronomy, 15, 139

Alonso-Medina A., Colón C., Zanón A., 2009, MNRAS, 395, 567

Alonso-Medina A., Colón C., Porcher P., 2011, Atomic Data and Nuclear Data Tables, 97, 36

Andersen T., Lindgard A., 1977, Journal of Physics B Atomic Molecular Physics, 10, 2359

Andersen T., Eriksen P., Poulsen O., Ramanujam P. S., 1979, Phys. Rev. A, 20, 2621

Ansbacher W., Pinnington E. H., Kernahan J. A., 1988, Canadian Journal of Physics, 66, 402

Asplund M., Grevesse N., Sauval A. J., Scott P., 2009, Annual Review of Astronomy and Astrophysics, 47, 481

Bahr J. L., Pinnington E. H., Kernahan J. A., O'Neill J. A., 1982, Canadian Journal of Physics, 60, 1108

Barnard A. J., Cooper J., Smith E. W., 1974, J. Quant. Spectr. Rad. Transf., 14, 1025

Barstow M. A., Holberg J. B., Hubeny I., Good S. A., Levan A. J., Meru F., 2001, MNRAS, 328, 211

Barstow M. A., Good S. A., Burleigh M. R., Hubeny I., Holberg J. B., Levan A. J., 2003, MNRAS, 344, 562

Battich T., Miller Bertolami M. M., Córsico A. H., Althaus L. G., 2018, A&A, 614, A136

Bauer F., Husfeld D., 1995, Astronomy & Astrophysics, 300, 481

Bessell M. S., 1999, Publications of the Astronomical Society of the Pacific, 111, 1426

Bethe H. A., 1939, Physical Review, 55, 434

Biswas S., Das A., Bhowmik A., Majumder S., 2018, MNRAS, 477, 5605

Bohlin R. C., 1996, AJ, 111, 1743

Bohlin R. C., Harris A. W., Holm A. V., Gry C., 1990, ApJS, 73, 413

Bohlin R. C., Dickinson M. E., Calzetti D., 2001, AJ, 122, 2118

Burbidge E. M., Burbidge G. R., Fowler W. A., Hoyle F., 1957, Reviews of Modern Physics, 29, 547

Busso M., Gallino R., Wasserburg G. J., 1999, ARA&A, 37, 239

Byrne C. M., Jeffery C. S., Tout C. A., Hu H., 2018, MNRAS, 475, 4728

Castellani M., Castellani V., 1993, ApJ, 407, 649

Charpinet S., et al., 2011, Nature, 480, 496

Chayer P., Dupuis J., Kruk J. W., 2015, in Dufour P., Bergeron P., Fontaine G., eds, Astronomical Society of the Pacific Conference Series Vol. 493, 19th European Workshop on White Dwarfs. p. 3 (arXiv:1412.3356)

Churilov S. S., Joshi Y. N., 1996, Journal of the Optical Society of America B Optical Physics, 13, 11

Colón C., Alonso-Medina A., Porcher P., 2014, Atomic Data and Nuclear Data Tables, 100, 272

Copperwheat C. M., Morales-Rueda L., Marsh T. R., Maxted P. F. L., Heber U., 2011, Monthly Notices of the Royal Astronomical Society, 415, 1381

Curtis L. J., 1992, Journal of the Optical Society of America B Optical Physics, 9, 5

Cutri R. M., et al. 2012, VizieR Online Data Catalog, 2311

Cutri R. M., et al., 2003, VizieR Online Data Catalog, 2246

D'Cruz N. L., Dorman B., Rood R. T., O'Connell R. W., 1996, ApJ, 466, 359

Dan M., Rosswog S., Guillochon J., Ramirez-Ruiz E., 2011, ApJ, 737, 89

Dimitrijevic M. S., Sahal-Brechot S., 1984, J. Quant. Spectr. Rad. Transf., 31, 301

Dorsch M., Latour M., Heber U., 2018, Open Astronomy, 27, 19

Dreizler S., Werner K., 1996, A&A, 314, 217

Drilling J. S., Heber U., 1987, in Philip A. G. D., Hayes D. S., Liebert J. W., eds, IAU Colloq. 95: Second Conference on Faint Blue Stars. pp 603–606

Edelmann H., Heber U., Hagen H.-J., Lemke M., Dreizler S., Napiwotzki R., Engels D., 2003, A&A, 400, 939

Fitzpatrick E. L., 1999, PASP, 111, 63

Fontaine G., Brassard P., Charpinet S., Green E. M., Randall S. K., Van Grootel V., 2012, A&A, 539, A12

Froese Fischer C., 1977, Journal of Physics B: Atomic and Molecular Physics, 10, 1241

Gaia Collaboration 2018, VizieR Online Data Catalog, 1345

Geier S., 2013, A&A, 549, A110

Geier S., Heber U., 2012, A&A, 543, A149

Geier S., Heber U., Edelmann H., Morales-Rueda L., Napiwotzki R., 2010, Ap&SS, 329, 127

Gianninas A., Bergeron P., Dupuis J., Ruiz M. T., 2010, ApJ, 720, 581

Good S. A., Barstow M. A., Burleigh M. R., Dobbie P. D., Holberg J. B., Hubeny I., 2005, MNRAS, 363, 183

Green E. M., et al., 2011, ApJ, 734, 59

Gruschinske J., Hunger K., Kudritzki R. P., Simon K., 1980, in Battrick B., Mort J., eds, ESA Special Publication Vol. 157, Ultraviolet observations of Quasars. pp 311–314

Han Z., Podsiadlowski P., Maxted P. F. L., Marsh T. R., Ivanova N., 2002, Monthly Notices of the Royal Astronomical Society, 336, 449

Haris K., Tauheed A., 2012, Phys. Scr, 85, 055301

Heber U., 2009, Annual Review of Astronomy and Astrophysics, 47, 211

Heber U., 2016, Publications of the Astronomical Society of the Pacific, 128, 082001

Heber U., Irrgang A., Schaffenroth J., 2018, Open Astronomy, 27, 35

Hirsch H. A., 2009, PhD thesis, Friedrich-Alexander University Erlangen-Nürnberg

Hoyle F., 1946, MNRAS, 106, 343

Hoyle F., 1954, ApJS, 1, 121

Hubeny I., 1988, Computer Physics Communications, 52, 103

Hubeny I., Lanz T., 1995, The Astrophysical Journal, 439, 875

Hubeny I., Lanz T., 2017a, preprint, (arXiv:1706.01859)

Hubeny I., Lanz T., 2017b, preprint, (arXiv:1706.01935)

Hubeny I., Lanz T., 2017c, preprint, (arXiv:1706.01937)

Hubeny I., Mihalas D., 2014, Theory of Stellar Atmospheres

Hubeny I., Hummer D. G., Lanz T., 1994, A&A, 282, 151

Humason M. L., Zwicky F., 1947, ApJ, 105, 85

Jeffery C. S., Neelamkodan N., Woolf V. M., Crawford S. M., Østensen R. H., 2017a, Open Astronomy, 26, 202

Jeffery C. S., et al., 2017b, MNRAS, 465, 3101

Joshi Y. N., van Kleef T. A. M., 1986, Canadian Journal of Physics, 64, 330

Kaufer A., Stahl O., Tubbesing S., Nørregaard P., Avila G., Francois P., Pasquini L., Pizzella A., 1999, The Messenger, 95, 8

Kilkenny D., van Wyk F., Roberts G., Marang F., Cooper D., 1998, MNRAS, 294, 93

Kudritzki R. P., 1976, A&A, 52, 11

Kurucz R. L., 2018, in Astronomical Society of the Pacific Conference Series. p. 47

Landolt A. U., Uomoto A. K., 2007a, AJ, 133, 768

Landolt A. U., Uomoto A. K., 2007b, AJ, 133, 768

Lanz T., Hubeny I., 2003, ApJS, 146, 417

Lanz T., Brown T. M., Sweigart A. V., Hubeny I., Landsman W. B., 2004, The Astrophysical Journal, 602, 342

Latour M., Fontaine G., Green E. M., Brassard P., 2015, A&A, 579, A39

Latour M., Green E. M., Fontaine G., 2019, arXiv e-prints, p. arXiv:1903.03444

Lawrence A., et al., 2013, VizieR Online Data Catalog, 2319

Lemke M., 1997, A&AS, 122, 285

Marcinek R., Migdalek J., 1993, Journal of Physics B Atomic Molecular Physics, 26, 1403

Marinoni S., et al., 2016, MNRAS, 462, 3616

Massey P., Strobel K., Barnes J. V., Anderson E., 1988, ApJ, 328, 315

Maxted P. F. L., Heber U., Marsh T. R., North R. C., 2001, MNRAS, 326, 1391

Menzies J. W., Marang F., Westerhuys J. E., 1990, South African Astronomical Observatory Circular, 14, 33

Mermilliod J. C., 2006, VizieR Online Data Catalog, 2168

Michaud G., Richer J., Richard O., 2011, A&A, 529, A60

Migdałek J., 1983, J. Quant. Spectr. Rad. Transf., 30, 169

Miller Bertolami M. M., Althaus L. G., Unglaub K., Weiss A., 2008, Astronomy & Astrophysics, 491, 253

Moore C. E., 1971, in , Nat. Stand. Ref. Data Ser., NSRDS-NBS 35, Vol. II (Reprint of NBS Circ. 467, Vol. II, 1952). Nat. Bur. Stand., U.S.

Morton D. C., 2000, ApJS, 130, 403

Münch G., 1958, ApJ, 127, 642

Napiwotzki R., 1992, in Heber U., Jeffery C. S., eds, Lecture Notes in Physics, Berlin Springer Verlag Vol. 401, The Atmospheres of Early-Type Stars. p. 310, doi:10.1007/3-540-55256-1_328

Napiwotzki R., Karl C. A., Lisker T., Heber U., Christlieb N., Reimers D., Nelemans G., Homeier D., 2004, Ap&SS, 291, 321

Naslim N., Jeffery C. S., Behara N. T., Hibbert A., 2011, MNRAS, 412, 363

Naslim N., Jeffery C. S., Hibbert A., Behara N. T., 2013, MNRAS, 434, 1920

Nielsen K. E., Wahlgren G. M., Proffitt C. R., Leckrone D. S., Adelman S. J., 2005, AJ, 130, 2312

O'Reilly F., Dunne P., 1998, Journal of Physics B Atomic Molecular Physics, 31, 1059

O'Toole S. J., 2004, A&A, 423, L25

O'Toole S., Heber U., 2006, arXiv e-prints, pp astro–ph/0612535

Oke J. B., 1990, AJ, 99, 1621

Pakalka S., Kučas S., Masys i. c. v., Kynienė A., Momkauskaitė A., Jonauskas V., 2018, Phys. Rev. A, 97, 012708

Paunzen E., 2015, VizieR Online Data Catalog, 358

Pereira C., Wesemael F., Bergeron P., 2006, Baltic Astronomy, 15, 123

Peterson A. V., 1970, PhD thesis, California Institute of Technology

Pinnington E. H., Bahr J. L., Kernahan J. A., Irwin D. J. G., 1981, Journal of Physics B Atomic Molecular Physics, 14, 1291

Pinnington E. H., Ansbacher W., Kernahan J. A., Inamdar A. S., 1985a, Journal of the Optical Society of America B Optical Physics, 2, 331

Pinnington E. H., Ansbacher W., Kernahan J. A., Gosselin R. N., Bahr J. L., 1985b, Journal of the Optical Society of America B Optical Physics, 2, 1653

Pinnington E. H., Ansbacher W., Kernahan J. A., Ge Z.-Q., Inamdar A. S., 1988, Nuclear Instruments and Methods in Physics Research B, 31, 206

Preval S. P., Barstow M. A., Badnell N. R., Holberg J. B., Hubeny I., 2015, in Dufour P., Bergeron P., Fontaine G., eds, Astronomical Society of the Pacific Conference Series Vol. 493, 19th European Workshop on White Dwarfs. p. 15 (arXiv:1410.0811)

Randall S. K., Bagnulo S., Ziegerer E., Geier S., Fontaine G., 2015, A&A, 576, A65

Rauch T., Werner K., Biémont É., Quinet P., Kruk J. W., 2012, A&A, 546, A55

Rauch T., Werner K., Bohlin R., Kruk J. W., 2013, A&A, 560, A106

Rauch T., Rudkowski A., Kampka D., Werner K., Kruk J. W., Moehler S., 2014a, A&A, 566, A3

Rauch T., Werner K., Quinet P., Kruk J. W., 2014b, A&A, 566, A10

Rauch T., Quinet P., Hoyer D., Werner K., Demleitner M., Kruk J. W., 2015, Tuebingen Oscillator Strengths Service Form Interface, VO resource provided by the GAVO Data Center, doi:10.21938/3i01isnuCODnh1zjbCvuwA, http://dc.zah.uni-heidelberg.de/toss/q/legacy/info

Rauch T., Quinet P., Hoyer D., Werner K., Demleitner M., Kruk J. W., 2016a, A&A, 587, A39

Rauch T., Quinet P., Hoyer D., Werner K., Richter P., Kruk J. W., Demleitner M., 2016b, A&A, 590, A128

Rauch T., Gamrath S., Quinet P., Löbling L., Hoyer D., Werner K., Kruk J. W., Demleitner M., 2017a, A&A, 599, A142

Rauch T., Quinet P., Knörzer M., Hoyer D., Werner K., Kruk J. W., Demleitner M., 2017b, A&A, 606, A105

Redfors A., 1991, A&A, 249, 589

Safronova U. I., Johnson W. R., 2004, Phys. Rev. A, 69, 052511

Safronova M. S., Safronova U. I., 2013, Phys. Rev. A, 87, 062509

Safronova U. I., Savukov I. M., Safronova M. S., Johnson W. R., 2003, Phys. Rev. A, 68, 062505

Safronova M. S., Safronova U. I., Clark C. W., 2014, Phys. Rev. A, 90, 032512

Saio H., Jeffery C. S., 2019, MNRAS, 482, 758

Schaffenroth V., Classen L., Nagel K., Geier S., Koen C., Heber U., Edelmann H., 2014, A&A, 570, A70

Schindewolf M., Németh P., Heber U., Battich T., Miller Bertolami M. M., Irrgang A., Latour M., 2018, A&A, 620, A36

Schoening T., Butler K., 1989, A&AS, 78, 51

Schönberner D., Drilling J. S., 1984, ApJ, 278, 702

Schork M., 2017, Die unterleuchtkräftigen O-Sterne HZ 44 und BD+75 325: Eine Radialgeschwindigkeitsstudie

Schuler S. C., King J. R., The L.-S., 2009, ApJ, 701, 837

Schwab J., 2018, MNRAS, 476, 5303

Schwab J., Shen K. J., Quataert E., Dan M., Rosswog S., 2012, MNRAS, 427, 190

Shamey L. J., 1969, PhD thesis, University of Colorado at Boulder

Simon K. P., Gruschinske J., Hunger K., Kudritzki R. P., 1980, in Battrick B., Mort J., eds, ESA Special Publication Vol. 157, Ultraviolet observations of Quasars. pp 305–306

Spencer Jones J. H., 1985, Monthly Notes of the Astronomical Society of South Africa, 44, 33

Stroeer A., Heber U., Lisker T., Napiwotzki R., Dreizler S., Christlieb N., Reimers D., 2007, Astronomy and Astrophysics, 462, 269

Sweigart A. V., 1997, ApJ, 474, L23

Tomley L., 1970, ApJ, 162, 239

Tremblay P.-E., Bergeron P., 2009, ApJ, 696, 1755

Van Grootel V., Fontaine G., Charpinet S., Brassard P., Green E. M., 2013, in European Physical Journal Web of Conferences. p. 04007, doi:10.1051/epjconf/20134304007

Vidal C. R., Cooper J., Smith E. W., 1970, J. Quant. Spectr. Rad. Transf., 10, 1011

Wamsteker W., Skillen I., Ponz J., de la Fuente A., Barylak M., Yurrita I., 2000, Astrophysics and Space Science, 273, 155

Webbink R. F., 1984, The Astrophysical Journal, 277, 355

Werner K., 1996, ApJ, 457, L39

Werner K., Dreizler S., 1999, Journal of Computational and Applied Mathematics, 109, 65

Werner K., Rauch T., Knörzer M., Kruk J. W., 2018, A&A, 614, A96

Zhang X., Jeffery C. S., 2012, Monthly Notices of the Royal Astronomical Society, 419, 452

Zhang W., Palmeri P., Quinet P., Biémont É., 2013, A&A, 551, A136

Zhang X., Hall P. D., Jeffery C. S., Bi S., 2017, The Astrophysical Journal, 835, 242

van Hoof P., 2017, The Atomic Line List v2.05b21, http://www.pa.uky.edu/~peter/newpage/

von Weizsäcker C. F., 1937, Physikalische Zeitschrift, 38, 176

von Weizsäcker C. F., 1938, Physikalische Zeitschrift, 39, 633

# Appendices

## A   Additional material

### A.1   Spectroscopic data

**Table 11.** List of spectra used in our analysis.

| Star | Instrument | Dataset | Range (Å) | Exp. (s) | R |
|---|---|---|---|---|---|
| HD 127493 | FEROS | ADP.2016-09-21T07:07:18.680 | $3527.9 - 9217.7$ | 600 | 48000 |
| | | ADP.2016-09-21T07:07:18.736 | $3527.9 - 9217.7$ | 300 | |
| | | ADP.2016-09-21T07:07:18.686 | $3527.9 - 9217.7$ | 300 | |
| | IUE LWR | LWR03587HS | $1850.0 - 3350.0$ | 5400 | 10000 |
| | | LWR04198HL | $1850.0 - 3350.0$ | 4450 | |
| | | LWR06702HL | $1850.0 - 3350.0$ | 5400 | |
| | | LWR07211HL | $1850.0 - 3350.0$ | 2950 | |
| | GHRS G160M | Z2H60107T | $1222.6 - 1258.8$ | 462 | 0.07Å |
| | | Z2H60109T | $1254.9 - 1291.0$ | 462 | |
| | | Z2H6010BT | $1285.6 - 1321.6$ | 462 | |
| | | Z2H6010DT | $1317.7 - 1353.6$ | 462 | |
| | | Z2H6010FT | $1349.7 - 1385.5$ | 517 | |
| | | Z2H6010HT | $1383.0 - 1418.8$ | 598 | |
| | | Z2H6010JT | $1414.9 - 1450.5$ | 517 | |
| | | Z2H6010LT | $1532.5 - 1567.7$ | 653 | |
| | | Z2H6010OT | $1623.2 - 1658.1$ | 462 | |
| | | Z2H6010QT | $1713.0 - 1747.6$ | 462 | |
| | IUE SWP | SWP04071HS | $1150.0 - 1980.0$ | 5880 | 10000 |
| | | SWP04860HL | $1150.0 - 1980.0$ | 3000 | |
| | | SWP07695HL | $1150.0 - 1980.0$ | 4500 | |
| | | SWP08276HL | $1150.0 - 1980.0$ | 3930 | |
| HZ 44 | HIRES | HI.20050810.20686 | $3214 \quad - 5990$ | 600 | 36000 |
| | | HI.20050810.21381 | $3890 \quad - 6732$ | 600 | |
| | | HI.20050812.21565 | $3214 \quad - 5990$ | 500 | |
| | | HI.20070504.38715 | $3022 \quad - 5800$ | 900 | |
| | | HI.20160203.58141 | $4716 \quad - 7580$ | 600 | |
| | | HI.20160401.55323 | $3128 \quad - 5947$ | 600 | |
| | IUE SWP | SWP16294HL | $1150.0 - 1980.0$ | 9600 | |
| | | SWP17350HL | $1150.0 - 1980.0$ | 14820 | |
| | FUSE MDRS | p3020401000 | $904.3 - 1188.4$ | 5919 | 19000 |
| | FUSE LWRS | m1080401000 | $904.3 - 1188.4$ | 4679 | 17000? |
| | FUSE LWRS | s5051901000 | $904.3 - 1188.4$ | 3937 | |

## A.2   **Photometric data**

**Table 12.** Photometric data used for the SED-fit of HZ 44.

| system | passband | magnitude | uncertainty | type | reference |
|--------|----------|-----------|-------------|------|-----------|
| 2MASS | H | 12.569 | 0.023 | magnitude | (Cutri et al. 2003, 2MASS: II/246/out) |
| 2MASS | J | 12.386 | 0.022 | magnitude | (Cutri et al. 2003, 2MASS: II/246/out) |
| 2MASS | K | 12.672 | 0.027 | magnitude | (Cutri et al. 2003, 2MASS: II/246/out) |
| Stroemgren | $H_\beta$ | 2.617 | | color | (Paunzen 2015, J/A+A/580/A23/catalog) |
| Stroemgren | bmy | −0.151 | | color | (Paunzen 2015, J/A+A/580/A23/catalog) |
| Stroemgren | m1 | 0.104 | 0.020 | color | (Paunzen 2015, J/A+A/580/A23/catalog) |
| Stroemgren | y | 11.715 | 0.007 | magnitude | (Paunzen 2015, J/A+A/580/A23/catalog) |
| UKIDSS | H | 12.560 | 0.002 | magnitude | (Lawrence et al. 2013, UKIDSS DR9: II/319/las9) |
| UKIDSS | J | 12.400 | 0.001 | magnitude | (Lawrence et al. 2013, UKIDSS DR9: II/319/las9) |
| UKIDSS | K | 12.687 | 0.002 | magnitude | (Lawrence et al. 2013, UKIDSS DR9: II/319/las9) |
| UKIDSS | Y | 12.276 | 0.001 | magnitude | (Lawrence et al. 2013, UKIDSS DR9: II/319/las9) |
| WISE | W1 | 12.750 | 0.023 | magnitude | (Cutri & et al. 2012, AllWISE: II/328/allwise) |
| WISE | W2 | 12.830 | 0.025 | magnitude | (Cutri & et al. 2012, AllWISE: II/328/allwise) |
| IUE box | $1300 - 1800\,\text{Å}$ | 7.903 | 0.020 | magnitude | (Wamsteker et al. 2000, VI/110/inescat, SWP03432LL) |
| IUE box | $2000 - 2500\,\text{Å}$ | 8.609 | 0.020 | magnitude | (Wamsteker et al. 2000, VI/110/inescat, LWR03017LL) |
| IUE box | $2500 - 3000\,\text{Å}$ | 9.047 | 0.020 | magnitude | (Wamsteker et al. 2000, VI/110/inescat, LWR03017LL) |
| *Gaia* | G | 11.6350 | 0.001 | magnitude | (Gaia Collaboration 2018, I/345/gaia2) |
| *Gaia* | GBP | 11.3913 | 0.007 | magnitude | (Gaia Collaboration 2018, I/345/gaia2) |
| *Gaia* | GRP | 11.9377 | 0.001 | magnitude | (Gaia Collaboration 2018, I/345/gaia2) |
| Johnson | VmI | −0.322 | 0.002 | color | (Landolt & Uomoto 2007b, J/AJ/133/768/table4) |
| Johnson | RmI | −0.181 | 0.001 | color | (Landolt & Uomoto 2007b, J/AJ/133/768/table4) |
| Johnson | VmR | −0.141 | 0.001 | color | (Landolt & Uomoto 2007b, J/AJ/133/768/table4) |
| Johnson | BmV | −0.291 | 0.001 | color | (Landolt & Uomoto 2007b, J/AJ/133/768/table4) |
| Johnson | UmB | −1.196 | 0.003 | color | (Landolt & Uomoto 2007b, J/AJ/133/768/table4) |
| Johnson | V | 11.673 | 0.002 | magnitude | (Landolt & Uomoto 2007b, J/AJ/133/768/table4) |

**Table 13.** Photometric data used for the SED-fit of HD 127493.

| system | passband | magnitude | uncertainty | type | reference |
|--------|----------|-----------|-------------|------|-----------|
| 2MASS | H | 10.816 | 0.028 | magnitude | (Cutri et al. 2003, 2MASS: II/246/out) |
| 2MASS | J | 10.641 | 0.023 | magnitude | (Cutri et al. 2003, 2MASS: II/246/out) |
| 2MASS | K | 10.907 | 0.025 | magnitude | (Cutri et al. 2003, 2MASS: II/246/out) |
| Johnson | BmV | -0.234 | | color | (Mermilliod 2006, II/168/ubvmeans) |
| Johnson | UmB | -1.17 | | color | (Mermilliod 2006, II/168/ubvmeans) |
| Johnson | V | 10.05 | | magnitude | (Mermilliod 2006, II/168/ubvmeans) |
| Stroemgren | Hbeta-B | 2.57 | | color | (Paunzen 2015, J/A+A/580/A23/catalog) |
| Stroemgren | bmy | -0.114 | 0.003 | color | (Paunzen 2015, J/A+A/580/A23/catalog) |
| Stroemgren | c1 | -0.214 | 0.013 | color | (Paunzen 2015, J/A+A/580/A23/catalog) |
| Stroemgren | m1 | 0.048 | 0.002 | color | (Paunzen 2015, J/A+A/580/A23/catalog) |
| Stroemgren | y | 10.035 | 0.009 | magnitude | (Paunzen 2015, J/A+A/580/A23/catalog) |
| WISE | W1 | 10.954 | 0.023 | magnitude | (Cutri & et al. 2012, AllWISE: II/328/allwise) |
| WISE | W2 | 11.045 | 0.021 | magnitude | (Cutri & et al. 2012, AllWISE: II/328/allwise) |
| IUE box | 1300-1800 | 6.306 | 0.02 | magnitude | (Wamsteker et al. 2000, VI/110/inescat, SWP08275LL) |
| IUE box | 2000-2500 | 7.164 | 0.02 | magnitude | (Wamsteker et al. 2000, VI/110/inescat, LWR07210LL) |
| IUE box | 2500-3000 | 7.547 | 0.02 | magnitude | (Wamsteker et al. 2000, VI/110/inescat, LWR07210LL) |
| *Gaia* G | | 9.9636 | 0.0011 | Magnitude | (Gaia Collaboration 2018, I/345/gaia2) |
| *Gaia* GBP | | 9.8227 | 0.0038 | Magnitude | (Gaia Collaboration 2018, I/345/gaia2) |
| *Gaia* GRP | | 10.2446 | 0.0015 | Magnitude | (Gaia Collaboration 2018, I/345/gaia2) |
| Johnson | BmV | -0.258 | | color | Menzies et al. (1990) |
| Johnson | UmB | -1.165 | | color | Menzies et al. (1990) |
| Johnson | V | 10.01 | | magnitude | Menzies et al. (1990) |
| Johnson | BmV | -0.269 | | color | Kilkenny et al. (1998) |
| Johnson | UmB | -1.184 | | color | Kilkenny et al. (1998) |
| Johnson | VmR | -0.115 | | color | Kilkenny et al. (1998) |
| Johnson | VmI | -0.276 | | color | Kilkenny et al. (1998) |
| Johnson | V | 10.039 | | magnitude | Kilkenny et al. (1998) |

## A.3   Abundance results & literature

**Table 14.** Abundances of HZ 44 and HD 127493[a] compared to other hot stars affected by diffusion: the He-sdO CD–31° 4800[b], the intermediate He-sdOB UVO 0825+15[c], the H-rich sdO Feige 110[d], and the DO WD RE 0503−289[e].

| Element | Particle fraction ($\epsilon_X$) | | | | | | Particle fraction relative to solar ($\epsilon_X - \epsilon_{X,\odot}$) | | | | | |
|---|---|---|---|---|---|---|---|---|---|---|---|---|
| | HZ44 | HD127493 | CD-31° 4800 | UVO0825+15 | Feige110 | RE0503-289 | HZ44 | HD127493 | CD-31° 4800 | UVO0825+15 | Feige110 | RE0503-289 |
| H | $-0.36^{+0.03}_{-0.03}$ | $-0.71^{+0.26}_{-0.22}$ | $-2.61^{+0.20}_{-0.20}$ | $-0.10^{+0.00}_{-0.00}$ | $-0.01^{+0.00}_{-0.00}$ | $-2.87^{+0.00}_{-0.00}$ | $-0.32^{+0.03}_{-0.03}$ | $-0.68^{+0.26}_{-0.22}$ | $-2.58^{+0.20}_{-0.20}$ | $-0.06^{+0.00}_{-0.00}$ | $0.03^{+0.00}_{-0.00}$ | $-2.83^{+0.00}_{-0.00}$ |
| He | $-0.26^{+0.02}_{-0.02}$ | $-0.09^{+0.08}_{-0.04}$ | $-0.00^{+0.00}_{-0.00}$ | $-0.70^{+0.00}_{-0.00}$ | $-1.67^{+0.10}_{-0.10}$ | $-0.00^{+0.00}_{-0.00}$ | $0.85^{+0.02}_{-0.02}$ | $1.01^{+0.08}_{-0.05}$ | $1.10^{+0.01}_{-0.01}$ | $0.41^{+0.01}_{-0.01}$ | $-0.57^{+0.10}_{-0.10}$ | $1.10^{+0.01}_{-0.01}$ |
| C | $-4.67^{+0.13}_{-0.13}$ | $-5.01^{+0.26}_{-0.25}$ | $-4.62^{+0.24}_{-0.24}$ | $<-5.40^{+0.00}$ | $<-8.03^{+0.20}$ | $-2.12^{+0.20}_{-0.20}$ | $-1.06^{+0.14}_{-0.14}$ | $-1.41^{+0.26}_{-0.26}$ | $-1.02^{+0.24}_{-0.24}$ | $<-1.79^{+0.05}$ | $<-4.43^{+0.20}$ | $1.48^{+0.20}_{-0.20}$ |
| N | $-2.74^{+0.20}_{-0.21}$ | $-2.80^{+0.29}_{-0.32}$ | $-2.92^{+0.22}_{-0.24}$ | $-3.86^{+0.24}_{-0.24}$ | $-4.92^{+0.20}_{-0.22}$ | $-4.80^{+0.20}_{-0.20}$ | $1.46^{+0.21}_{-0.21}$ | $1.41^{+0.29}_{-0.33}$ | $1.28^{+0.22}_{-0.25}$ | $0.35^{+0.24}_{-0.24}$ | $-0.72^{+0.20}_{-0.21}$ | $-0.59^{+0.20}_{-0.21}$ |
| O | $-4.26^{+0.15}_{-0.15}$ | $<-5.01^{+0.30}$ | $-4.82^{+0.23}_{-0.26}$ | $-4.47^{+0.07}_{-0.07}$ | $<-6.92^{+0.20}$ | $-3.13^{+0.20}_{-0.20}$ | $-0.91^{+0.16}_{-0.17}$ | $<-1.67^{+0.30}$ | $-1.48^{+0.23}_{-0.27}$ | $-1.12^{+0.08}_{-0.09}$ | $<-3.58^{+0.20}$ | $0.22^{+0.20}_{-0.21}$ |
| F | $<-5.36^{+0.40}$ | | | | | | $<2.12^{+0.45}$ | | | | | |
| Ne | $-3.59^{+0.11}_{-0.11}$ | $-3.61^{+0.30}_{-0.34}$ | $-3.44^{+0.22}_{-0.25}$ | $-4.42^{+0.25}_{-0.25}$ | | | $0.52^{+0.14}_{-0.16}$ | $0.49^{+0.31}_{-0.38}$ | $0.66^{+0.23}_{-0.29}$ | $-0.31^{+0.26}_{-0.29}$ | | |
| Na | $-4.79^{+0.07}_{-0.07}$ | $<-4.11^{+0.36}$ | | | | | $1.01^{+0.08}_{-0.08}$ | $<1.68^{+0.36}$ | | | | |
| Mg | $-4.16^{+0.20}_{-0.20}$ | $-4.10^{+0.30}_{-0.34}$ | $-4.17^{+0.21}_{-0.24}$ | $-5.65^{+0.11}_{-0.11}$ | | | $0.28^{+0.20}_{-0.21}$ | $0.33^{+0.30}_{-0.35}$ | $0.26^{+0.22}_{-0.24}$ | $-1.21^{+0.12}_{-0.12}$ | | |
| Al | $-5.21^{+0.11}_{-0.11}$ | $-5.24^{+0.27}_{-0.26}$ | $-5.29^{+0.27}_{-0.33}$ | $-5.43^{+0.07}_{-0.07}$ | | | $0.38^{+0.11}_{-0.12}$ | $0.34^{+0.27}_{-0.26}$ | $0.29^{+0.27}_{-0.33}$ | $0.16^{+0.08}_{-0.08}$ | | |
| Si | $-4.24^{+0.11}_{-0.11}$ | $-4.02^{+0.27}_{-0.29}$ | $-4.31^{+0.24}_{-0.28}$ | $-5.64^{+0.21}_{-0.21}$ | $<-7.82^{+0.20}$ | $-4.63^{+0.20}_{-0.20}$ | $0.29^{+0.12}_{-0.12}$ | $0.51^{+0.27}_{-0.29}$ | $0.21^{+0.24}_{-0.29}$ | $-1.11^{+0.21}_{-0.21}$ | $<-3.29^{+0.20}$ | $-0.11^{+0.20}_{-0.20}$ |
| P | $-6.02^{+0.25}_{-0.25}$ | $<-5.41^{+0.36}$ | $-6.49^{+0.23}_{-0.28}$ | | $-6.64^{+0.20}_{-0.20}$ | $-6.86^{+0.20}_{-0.20}$ | $0.61^{+0.25}_{-0.26}$ | $<1.21^{+0.36}$ | $0.13^{+0.23}_{-0.28}$ | | $-0.01^{+0.20}_{-0.20}$ | $-0.23^{+0.20}_{-0.20}$ |
| S | $-4.23^{+0.37}_{-0.37}$ | $-4.61^{+0.39}_{-0.50}$ | $-4.57^{+0.26}_{-0.31}$ | $-4.29^{+0.18}_{-0.18}$ | $-5.49^{+0.20}_{-0.20}$ | $-5.30^{+0.20}_{-0.20}$ | $0.69^{+0.37}_{-0.38}$ | $0.30^{+0.39}_{-0.50}$ | $0.34^{+0.26}_{-0.31}$ | $0.63^{+0.18}_{-0.18}$ | $-0.57^{+0.20}_{-0.20}$ | $-0.38^{+0.20}_{-0.20}$ |
| Cl | $-7.86^{+0.70}_{-0.70}$ | | | $-5.56^{+0.11}_{-0.11}$ | | | $-1.32^{+0.71}_{-1.26}$ | | | $0.98^{+0.31}_{-0.34}$ | | |
| Ar | $-4.15^{+0.12}_{-0.12}$ | $<-4.31^{+0.30}$ | | $<-3.60^{+0.00}$ | | | $1.49^{+0.17}_{-0.19}$ | $<1.32^{+0.31}$ | | $<2.04^{+0.13}$ | | |
| K | $-5.27^{+0.16}_{-0.16}$ | | | | | | $1.74^{+0.17}_{-0.20}$ | | | | | |
| Ca | $-4.25^{+0.24}_{-0.24}$ | $<-4.61^{+0.30}$ | | $-3.59^{+0.21}_{-0.21}$ | $<-5.61^{+0.20}$ | | $1.44^{+0.24}_{-0.25}$ | $<1.08^{+0.30}$ | | $2.11^{+0.21}_{-0.22}$ | $<-0.09^{+0.20}$ | |
| Ti | $-4.92^{+0.22}_{-0.22}$ | $<-5.11^{+0.33}$ | | $-4.53^{+0.34}_{-0.34}$ | $-5.40^{+0.20}_{-0.20}$ | | $2.17^{+0.22}_{-0.23}$ | $<1.97^{+0.33}$ | | $2.56^{+0.34}_{-0.35}$ | $1.68^{+0.20}_{-0.21}$ | |
| V | $<-5.16^{+0.40}$ | $<-6.71^{+0.43}$ | | $-4.39^{+0.25}_{-0.25}$ | $-5.94^{+0.20}_{-0.20}$ | | $<2.95^{+0.40}$ | $<1.39^{+0.44}$ | | $3.72^{+0.26}_{-0.27}$ | $2.17^{+0.21}_{-0.23}$ | |
| Cr | $-4.76^{+0.30}_{-0.30}$ | $-4.61^{+0.36}_{-0.44}$ | | | $-4.40^{+0.20}_{-0.20}$ | | $1.64^{+0.30}_{-0.31}$ | $1.78^{+0.36}_{-0.45}$ | | | $1.99^{+0.20}_{-0.21}$ | |
| Mn | $-5.26^{+0.40}_{-0.40}$ | $<-6.21^{+0.36}$ | | | $-4.43^{+0.20}_{-0.20}$ | | $1.35^{+0.40}_{-0.41}$ | $<0.39^{+0.36}$ | | | $2.18^{+0.20}_{-0.21}$ | |
| Fe | $-4.36^{+0.25}_{-0.25}$ | $-3.53^{+0.27}_{-0.27}$ | $-4.62^{+0.31}_{-0.39}$ | $<-4.90^{+0.00}$ | $-4.68^{+0.20}_{-0.20}$ | $<-6.02^{+0.20}$ | $0.18^{+0.25}_{-0.26}$ | $1.00^{+0.27}_{-0.28}$ | $-0.09^{+0.31}_{-0.40}$ | $<-0.36^{+0.04}$ | $-0.15^{+0.20}_{-0.21}$ | $<-1.49^{+0.20}$ |
| Co | $-5.96^{+0.50}_{-0.50}$ | $-6.01^{+0.36}_{-0.44}$ | | | $-4.80^{+0.20}_{-0.20}$ | | $1.09^{+0.50}_{-0.53}$ | $1.03^{+0.36}_{-0.47}$ | | | $2.25^{+0.20}_{-0.22}$ | |
| Ni | $-4.41^{+0.15}_{-0.15}$ | $-4.33^{+0.27}_{-0.28}$ | $-5.10^{+0.28}_{-0.35}$ | | $-4.38^{+0.20}_{-0.20}$ | $-5.30^{+0.20}_{-0.20}$ | $1.41^{+0.16}_{-0.16}$ | $1.49^{+0.27}_{-0.29}$ | $0.71^{+0.28}_{-0.35}$ | | $1.44^{+0.20}_{-0.21}$ | $0.52^{+0.20}_{-0.21}$ |
| Cu | $-6.16^{+0.40}_{-0.40}$ | $<-6.81^{+0.43}$ | | | | | $1.69^{+0.40}_{-0.41}$ | $<1.03^{+0.43}$ | | | | |
| Zn | $-6.06^{+0.20}_{-0.30}$ | $-6.01^{+0.36}_{-0.44}$ | | | $-5.83^{+0.20}_{-0.20}$ | $-5.15^{+0.20}_{-0.20}$ | $1.42^{+0.20}_{-0.31}$ | $1.46^{+0.36}_{-0.46}$ | | | $1.65^{+0.20}_{-0.21}$ | $2.32^{+0.20}_{-0.21}$ |
| Ga | $-6.36^{+0.50}_{-0.50}$ | $<-7.11^{+0.43}$ | | | | $-5.70^{+0.20}_{-0.20}$ | $2.64^{+0.50}_{-0.54}$ | $<1.88^{+0.44}$ | | | | $3.30^{+0.21}_{-0.23}$ |
| Ge | $-6.26^{+0.30}_{-0.30}$ | $-5.71^{+0.43}_{-0.56}$ | | $-5.66^{+0.06}_{-0.06}$ | $-6.10^{+0.20}_{-0.20}$ | $-5.05^{+0.20}_{-0.20}$ | $2.13^{+0.31}_{-0.34}$ | $2.67^{+0.44}_{-0.61}$ | | $2.73^{+0.11}_{-0.12}$ | $2.29^{+0.21}_{-0.24}$ | $3.33^{+0.21}_{-0.23}$ |
| As | $-7.76^{+0.40}_{-0.40}$ | | | | | $-6.06^{+0.20}_{-0.20}$ | $1.98^{+0.40}_{-0.41}$ | | | | | $3.68^{+0.20}_{-0.20}$ |
| Se | $<-6.66^{+0.40}$ | | | | | $-4.08^{+0.20}_{-0.20}$ | $<2.04^{+0.40}$ | | | | | $4.61^{+0.20}_{-0.20}$ |
| Kr | $<-5.56^{+0.60}$ | $<-5.51^{+0.43}$ | | | | $-5.61^{+0.20}_{-0.20}$ | $<3.23^{+0.60}$ | $<3.27^{+0.43}$ | | | | $3.17^{+0.21}_{-0.22}$ |
| Sr | $<-5.46^{+0.60}$ | $<-5.61^{+0.36}$ | | | | $-4.52^{+0.20}_{-0.20}$ | $<3.71^{+0.60}$ | $<3.55^{+0.36}$ | | | | $4.65^{+0.21}_{-0.22}$ |
| Y | $<-5.66^{+0.20}$ | $<-5.41^{+0.36}$ | | $-6.53^{+0.09}_{-0.09}$ | | | $<4.17^{+0.20}$ | $<4.41^{+0.36}$ | | $3.30^{+0.10}_{-0.11}$ | | |
| Zr | $-6.28^{+0.19}_{-0.19}$ | $<-6.01^{+0.30}$ | | $<-6.60^{+0.00}$ | | $-4.87^{+0.20}_{-0.20}$ | $3.18^{+0.19}_{-0.20}$ | $<3.44^{+0.30}$ | | $<2.86^{+0.04}$ | | $4.59^{+0.20}_{-0.21}$ |
| Mo | $<-6.56^{+0.40}$ | $<-6.81^{+0.43}$ | | | | $-5.10^{+0.20}_{-0.20}$ | $<3.60^{+0.40}$ | $<3.34^{+0.44}$ | | | | $5.06^{+0.21}_{-0.23}$ |
| Sn | $-7.26^{+0.40}_{-0.40}$ | $<-7.31^{+0.43}$ | | | | $-5.15^{+0.20}_{-0.20}$ | $2.74^{+0.40}_{-0.44}$ | $<2.68^{+0.44}$ | | | | $4.84^{+0.21}_{-0.24}$ |
| Sb | $<-8.36^{+0.50}$ | | | | | $-5.78^{+0.20}_{-0.20}$ | $<2.67^{+0.50}$ | | | | | $5.25^{+0.21}_{-0.22}$ |
| Te | $<-7.46^{+0.40}$ | | | | | $-5.10^{+0.20}_{-0.20}$ | $<2.40^{+0.40}$ | | | | | $4.76^{+0.20}_{-0.20}$ |
| Xe | $<-7.66^{+0.40}$ | | | | | $-5.39^{+0.20}_{-0.20}$ | $<2.14^{+0.40}$ | | | | | $4.41^{+0.21}_{-0.22}$ |
| Pb | $-6.25^{+0.09}_{-0.10}$ | $-6.36^{+0.43}_{-0.56}$ | $-6.41^{+0.18}_{-0.18}$ | | | | $4.04^{+0.13}_{-0.15}$ | $3.92^{+0.44}_{-0.61}$ | $3.88^{+0.20}_{-0.22}$ | | | |
| Th | $<-8.36^{+0.30}$ | $<-8.51^{+0.36}$ | | | | | $<3.66^{+0.31}$ | $<3.50^{+0.36}$ | | | | |

**Notes.** [a] He abundance from Hirsch (2009). [c] Abundances from Schindewolf et al. (2018). [c] Abundances from Jeffery et al. (2017b). [d] Abundances from Rauch et al. (2014a). [e] Abundances from Rauch et al. (2017b); Werner et al. (2018) and references therein.
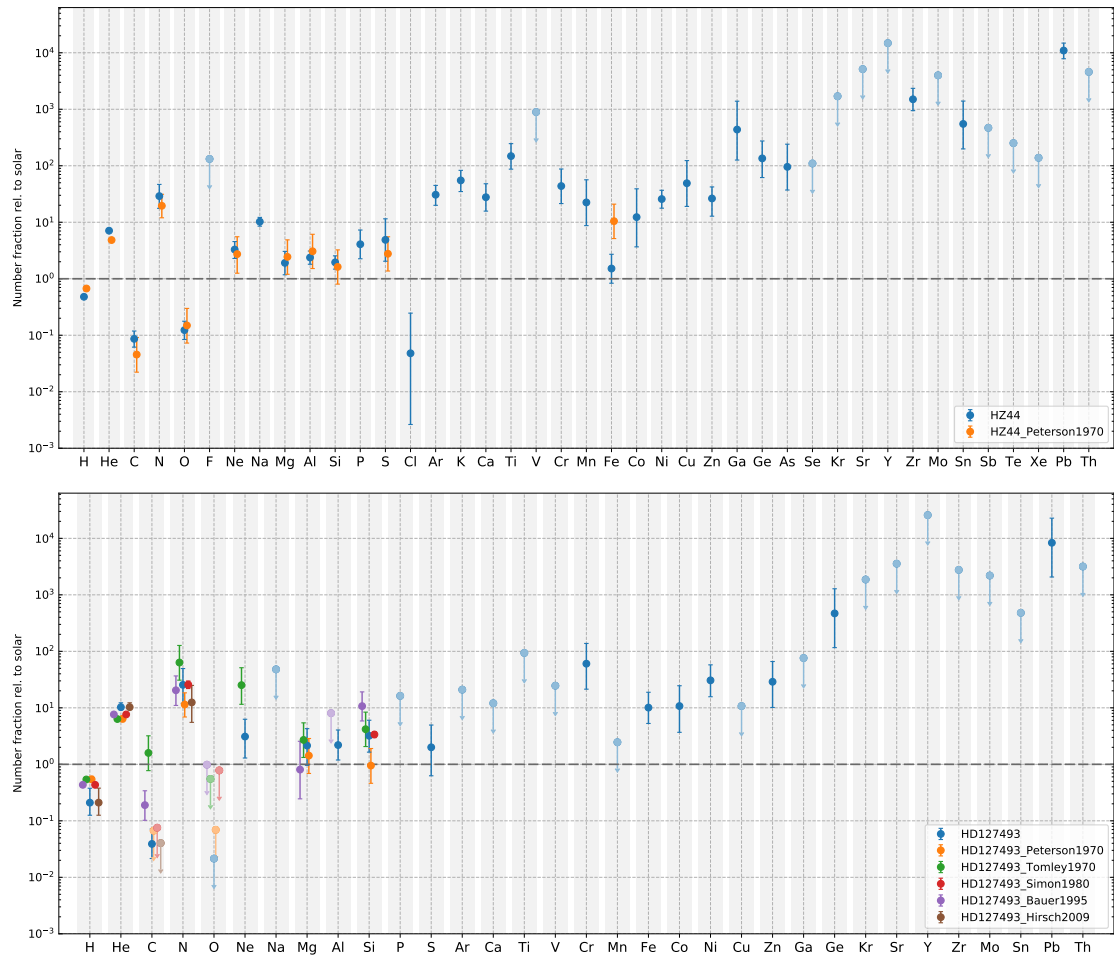
**Figure 28.** Same as Fig. 21 but for the comparison of abundances derived in this work with literature values.

# B Full spectra

This section shows the full observed and final synthetic spectra of HD 127493, HZ 44, and Feige 46. Elements with upper limits only are included at their upper limit. The synthetic spectra are convolved with a Gaussian kernel (constant for GHRS, but wavelength-depended for all echelle spectrographs) to match the resolution of the respective spectrograph. The strongest photospheric metal lines are labeled with pink marks, interstellar lines are labeled with green marks. The normalization of the HIRES spectrum of HZ 44 was only possible using the final synthetic spectrum as a template, so the wings of broad hydrogen and helium lines are modified to fit the synthetic spectrum. However, metal lines are not affected. The optical spectra of HZ 44 and HD 127493 are shown up to 6710 Å (due to the lack of metal lines at longer wavelengths). The model for Feige 46 compared to the GHRS spectrum includes in addition to the metals for which abundances were derived: Cr, Mn, Co, Zn, Ge, and Y. Specifically the inclusion of Cr, Mn, Co, and Zn lines improves the fit quality and abundances for these elements could be determined in a future analysis.
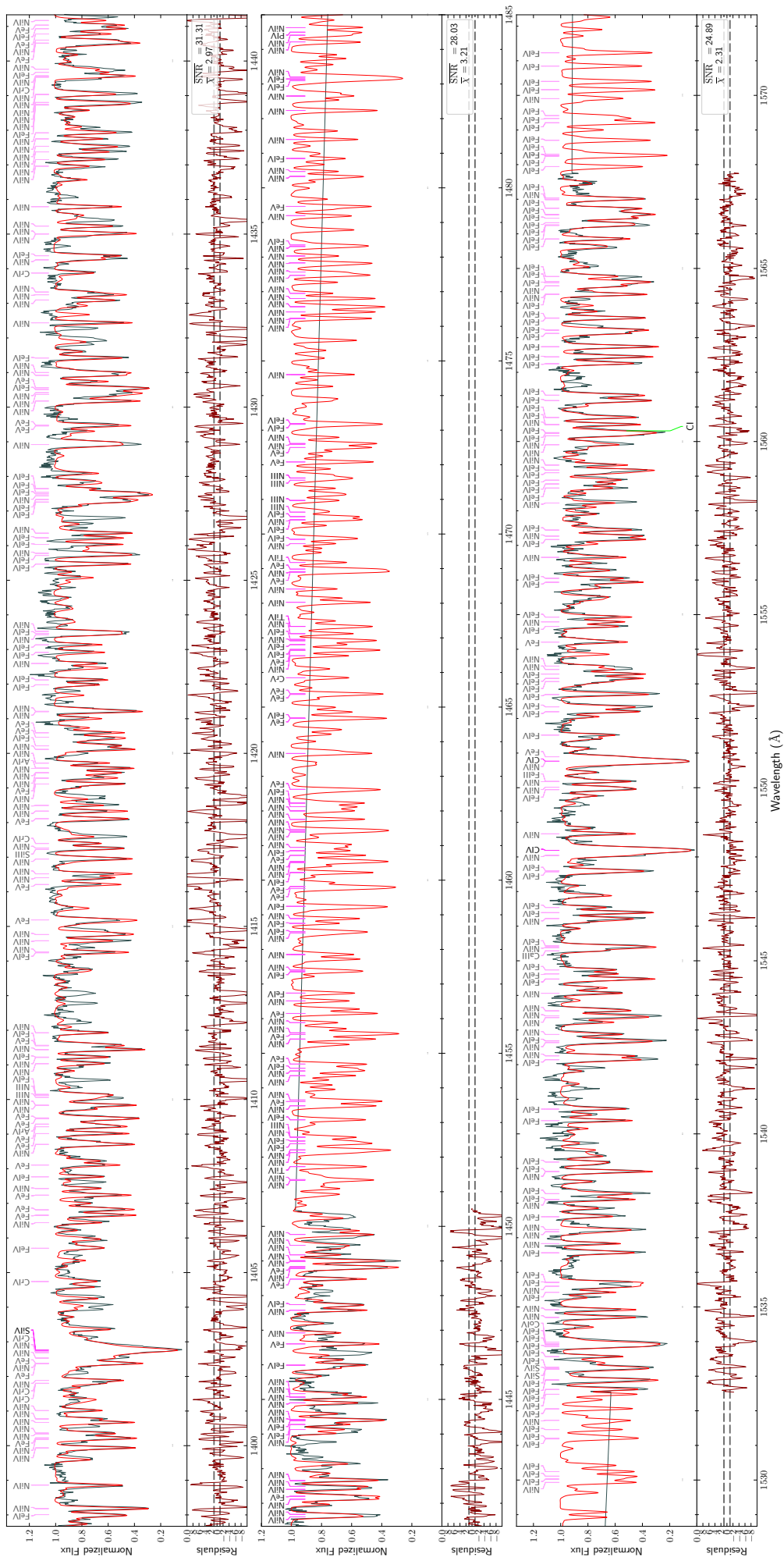
**Figure 29.** GHRS spectrum of HD 127493 (grey) and the final model (red).
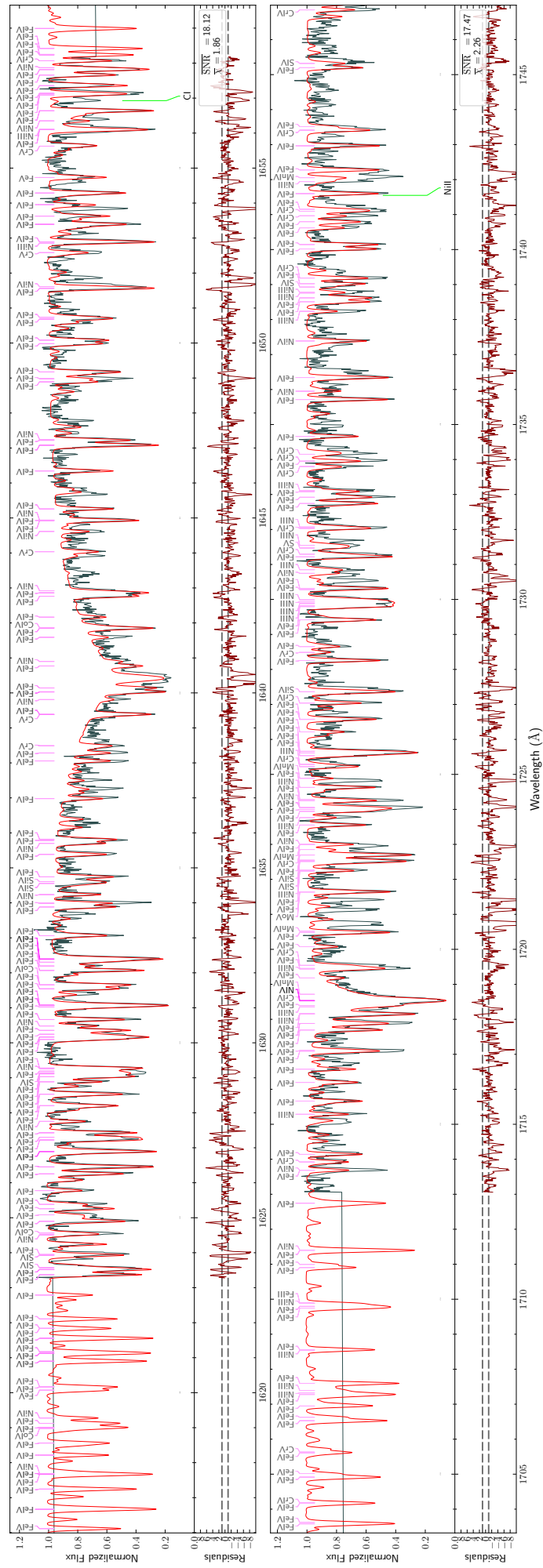
**Figure 29 (continued).** GHRS spectrum of HD 127493 (grey) and the final model (red).

**Figure 29 (continued).** GHRS spectrum of HD 127493 (grey) and the final model (red).

**Figure 30.** IUE spectrum of HD 127493 (grey) and the final model (red).

**Figure 30 (continued).** IUE spectrum of HD 127493 (grey) and the final model (red).

**Figure 30 (continued).** FEROS spectrum of HD 127493 (grey) and the final model (red).

**Figure 30 (continued).** FEROS spectrum of HD 127493 (grey) and the final model (red).

**Figure 30 (continued).** FEROS spectrum of HD 127493 (grey) and the final model (red).

**Figure 30 (continued).** FEROS spectrum of HD 127493 (grey) and the final model (red).
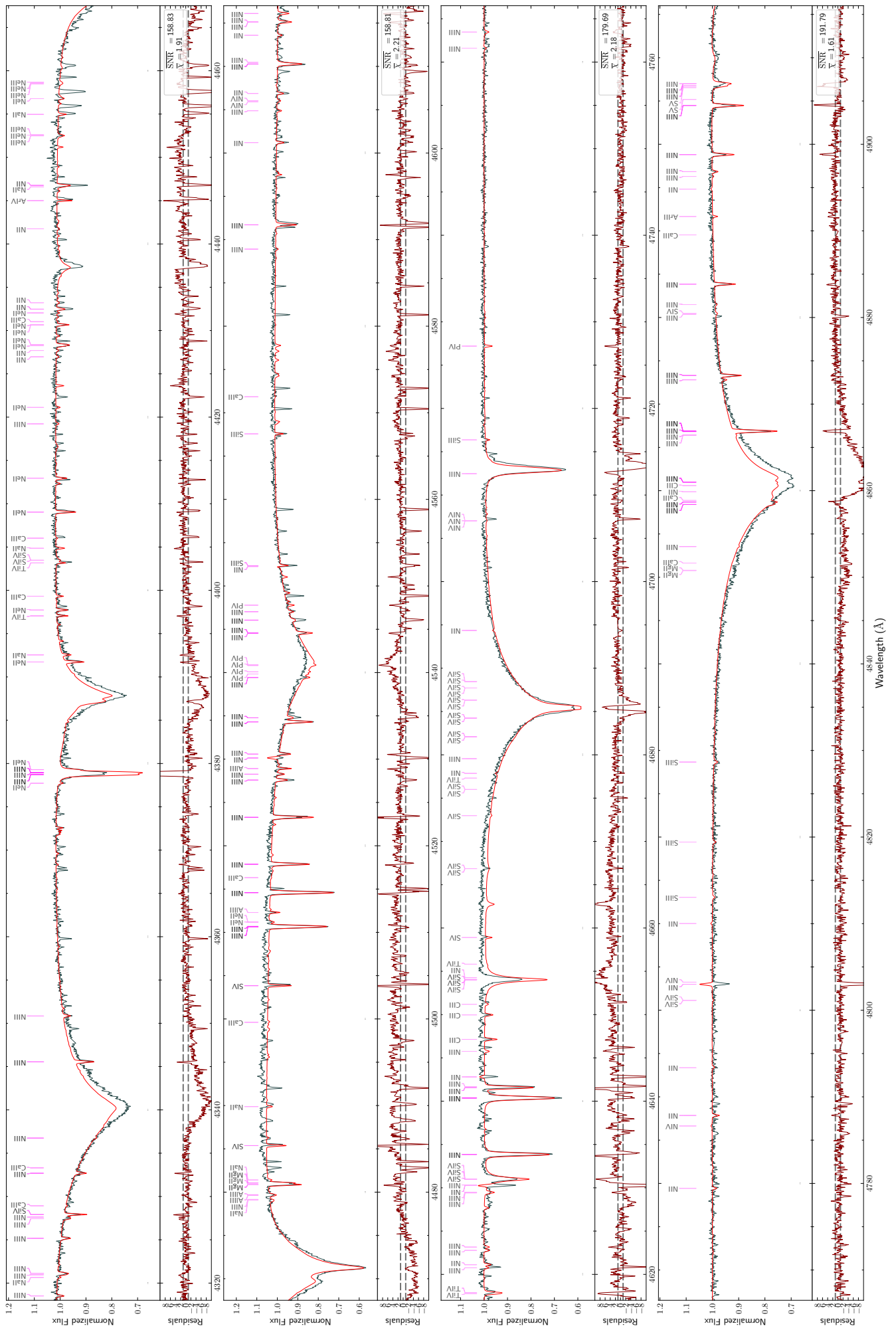
**Figure 30 (continued).** FEROS spectrum of HD 127493 (grey) and the final model (red).
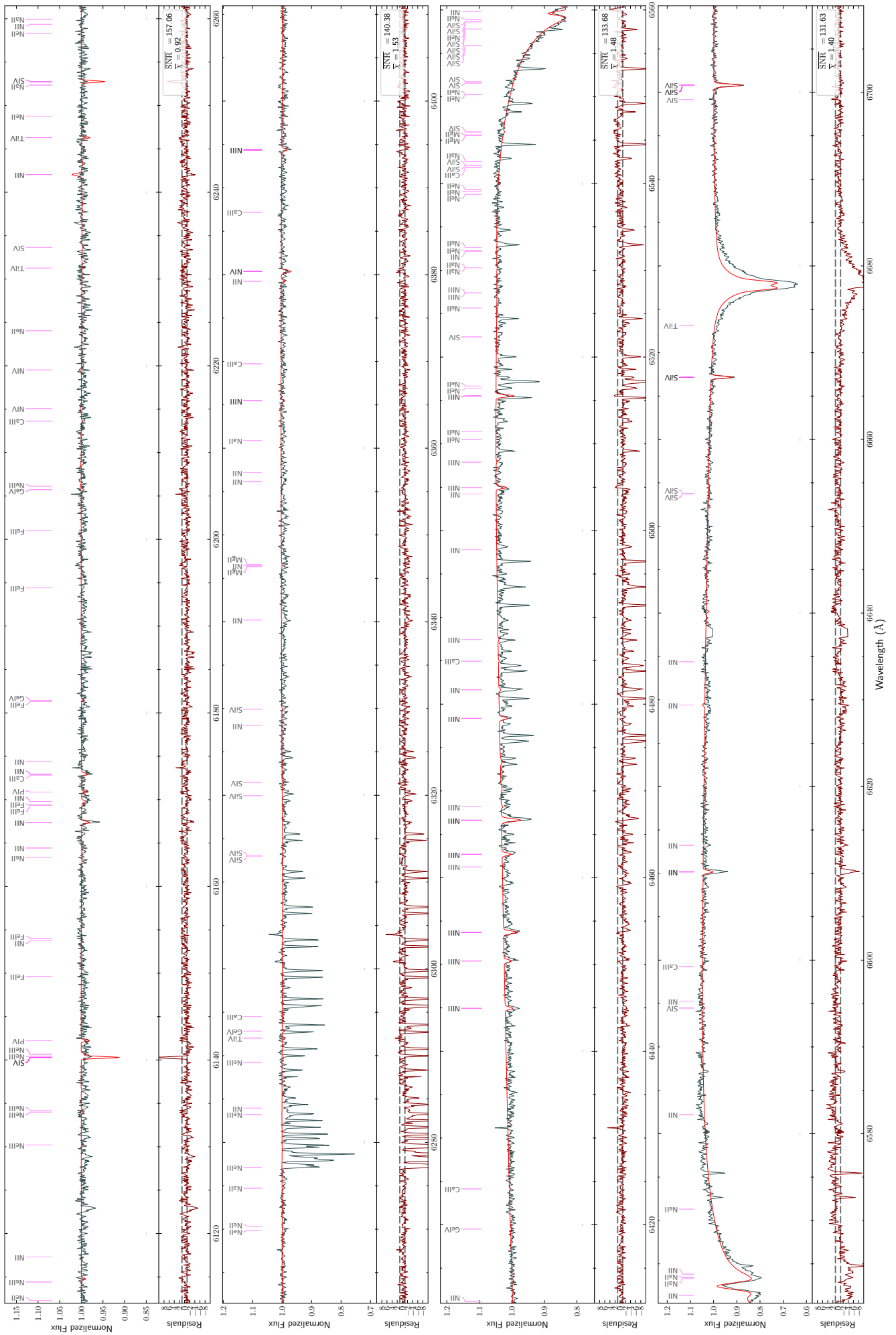
**Figure 31.** FUSE spectrum of HZ 44 (grey) and the final model (red).
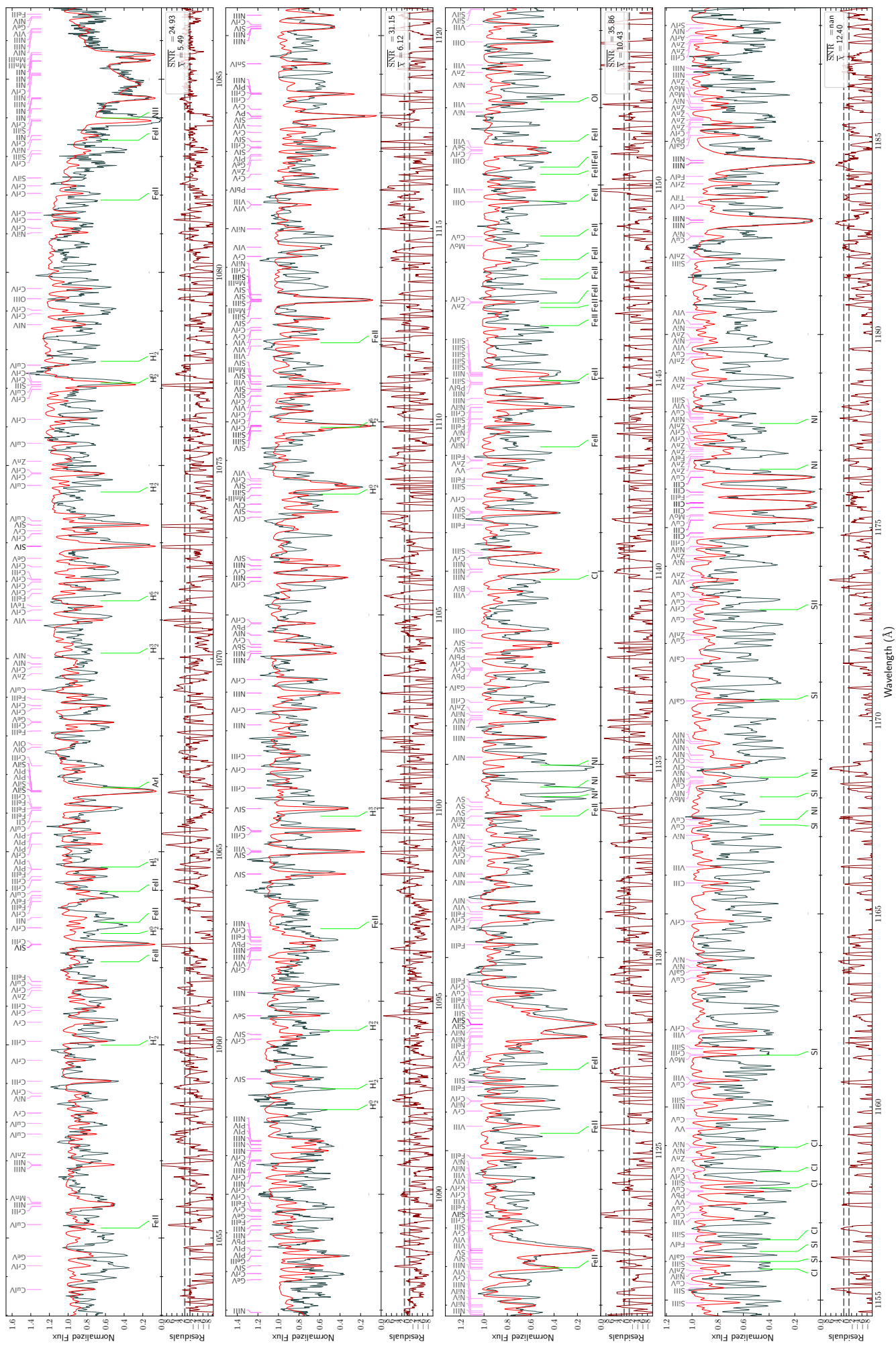
**Figure 31 (continued).** FUSE spectrum of HZ 44 (grey) and the final model (red).
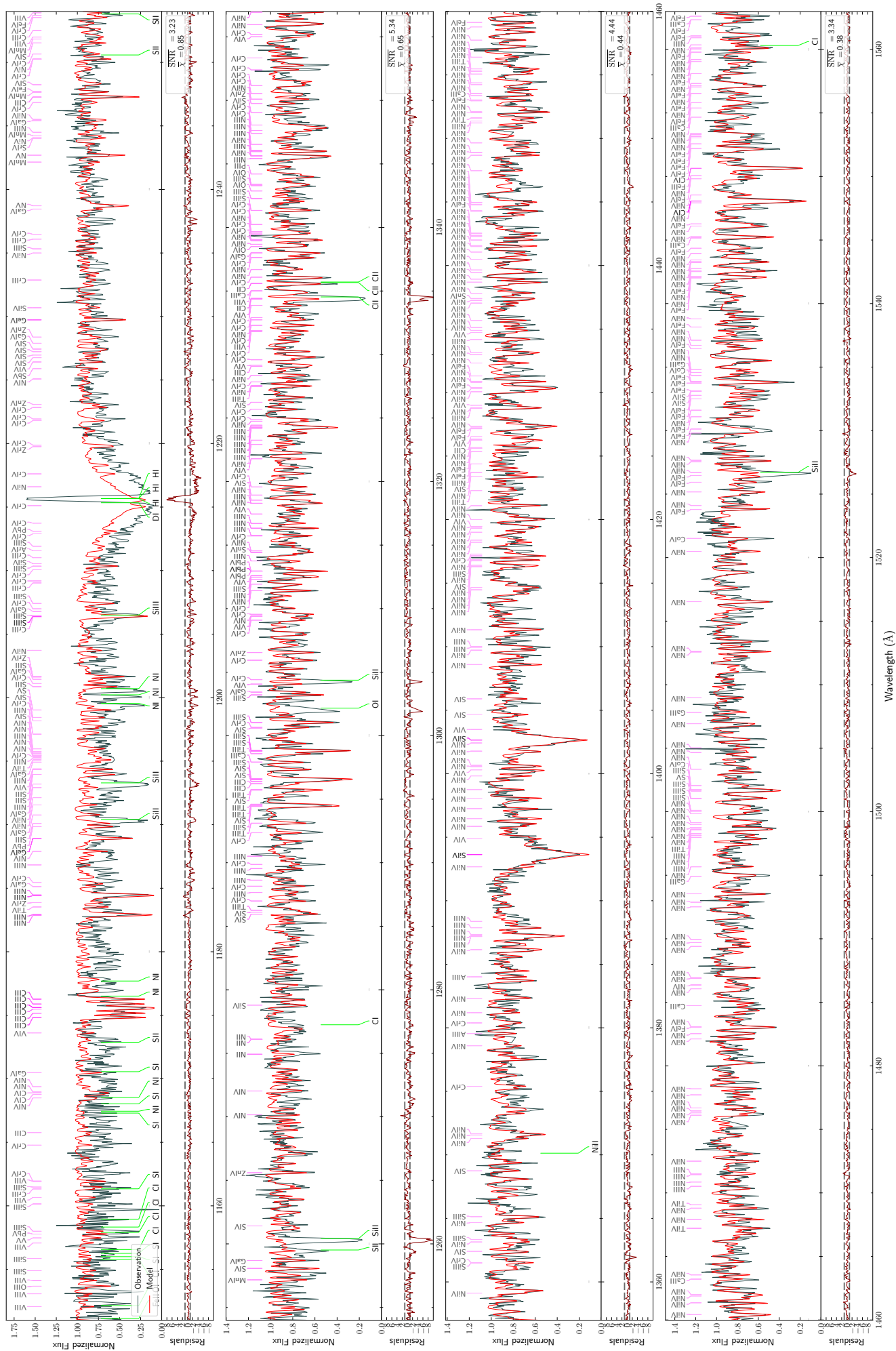
**Figure 32.** IUE spectrum of HZ 44 (grey) and the final model (red).
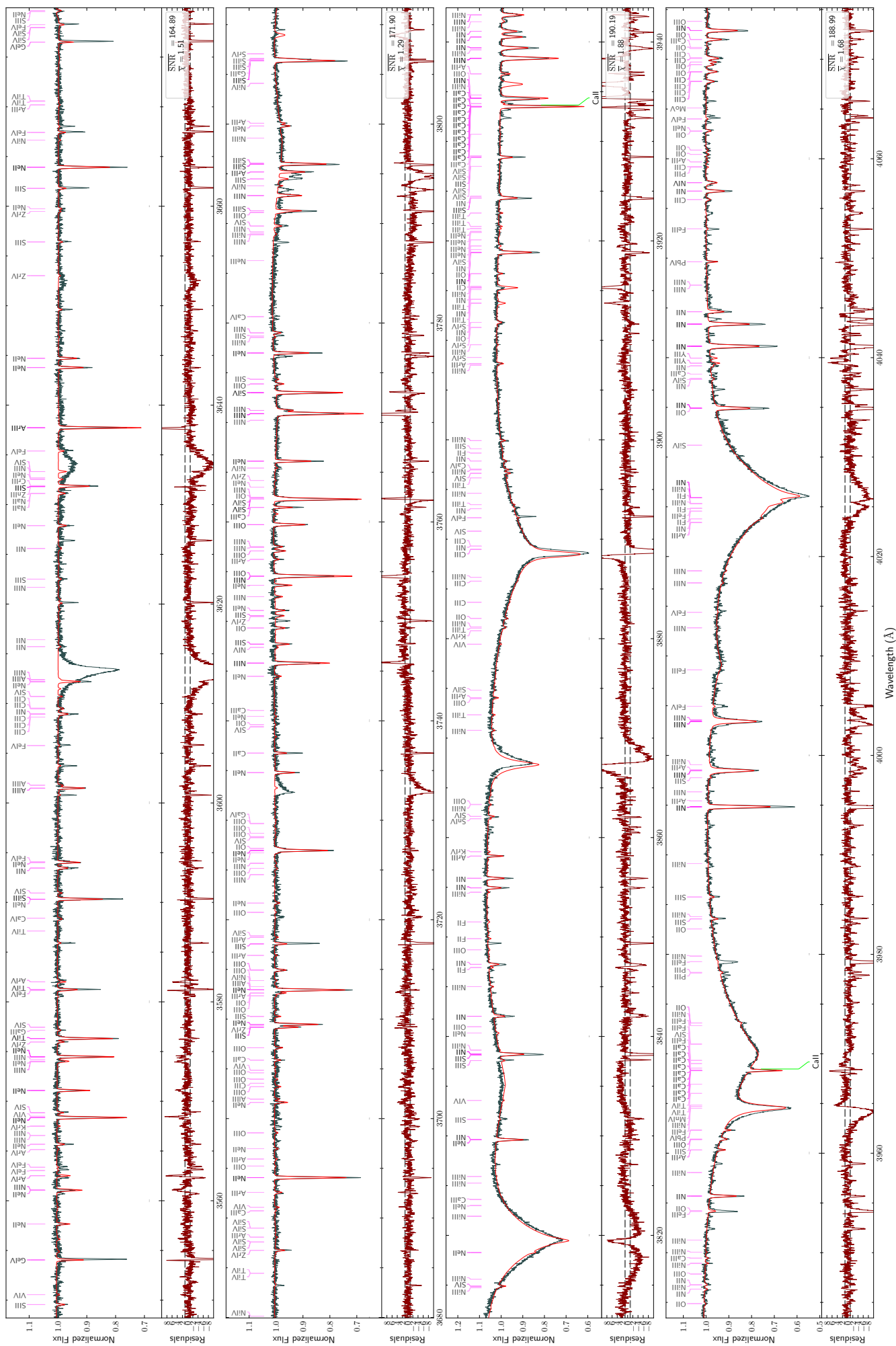
**Figure 32 (continued).** IUE spectrum of HZ 44 (grey) and the final model (red).

**Figure 33.** HIRES spectrum of HZ 44 (grey) and the final model (red).

**Figure 33 (continued).** HIRES spectrum of HZ 44 (grey) and the final model (red).

**Figure 33 (continued).** HIRES spectrum of HZ 44 (grey) and the final model (red).

**Figure 33 (continued).** HIRES spectrum of HZ 44 (grey) and the final model (red).

73

**Figure 33 (continued).** HIRES spectrum of HZ 44 (grey) and the final model (red).

**Figure 33 (continued).** HIRES spectrum of HZ 44 (grey) and the final model (red).

75
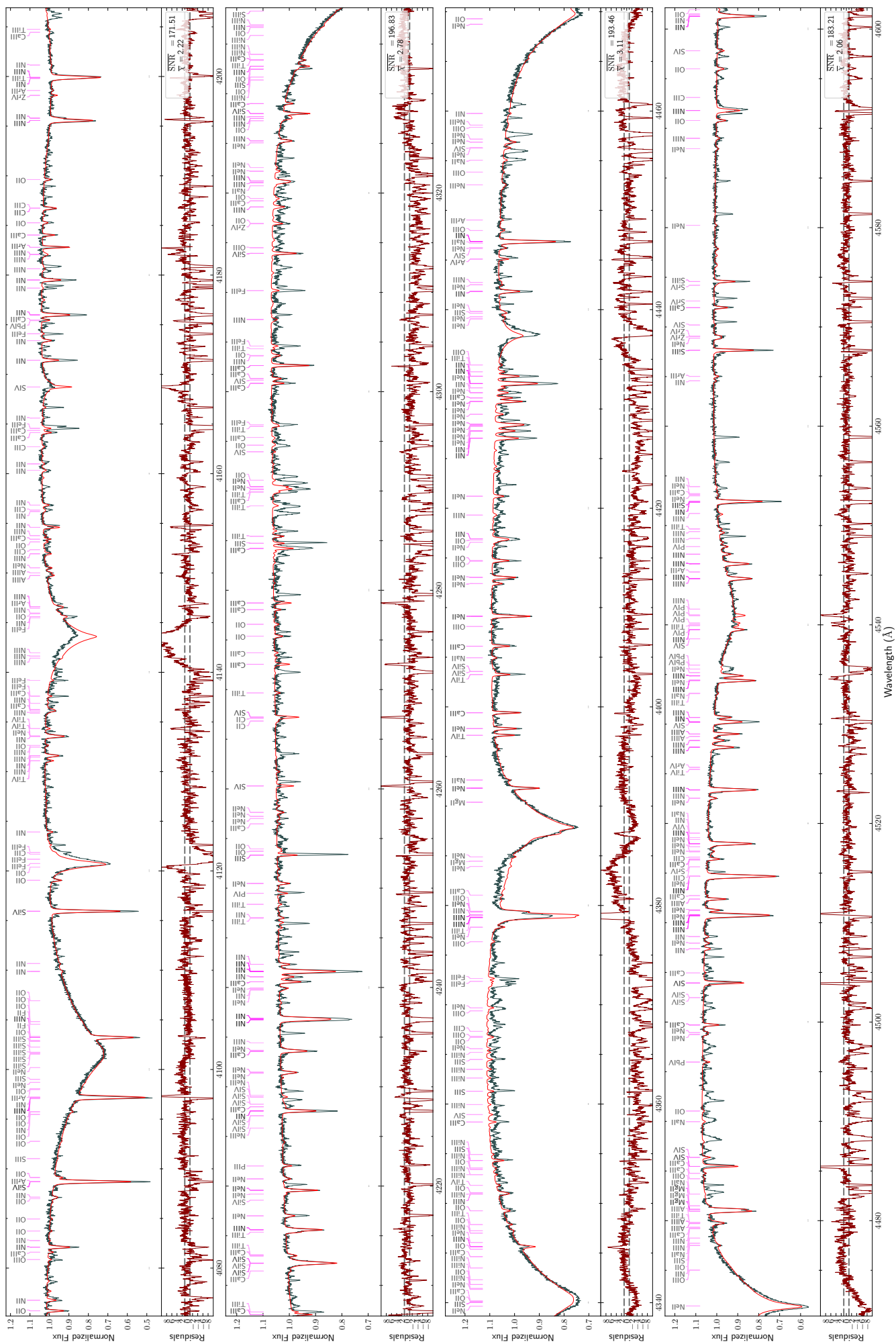
**Figure 33 (continued).** HIRES spectrum of HZ 44 (grey) and the final model (red).
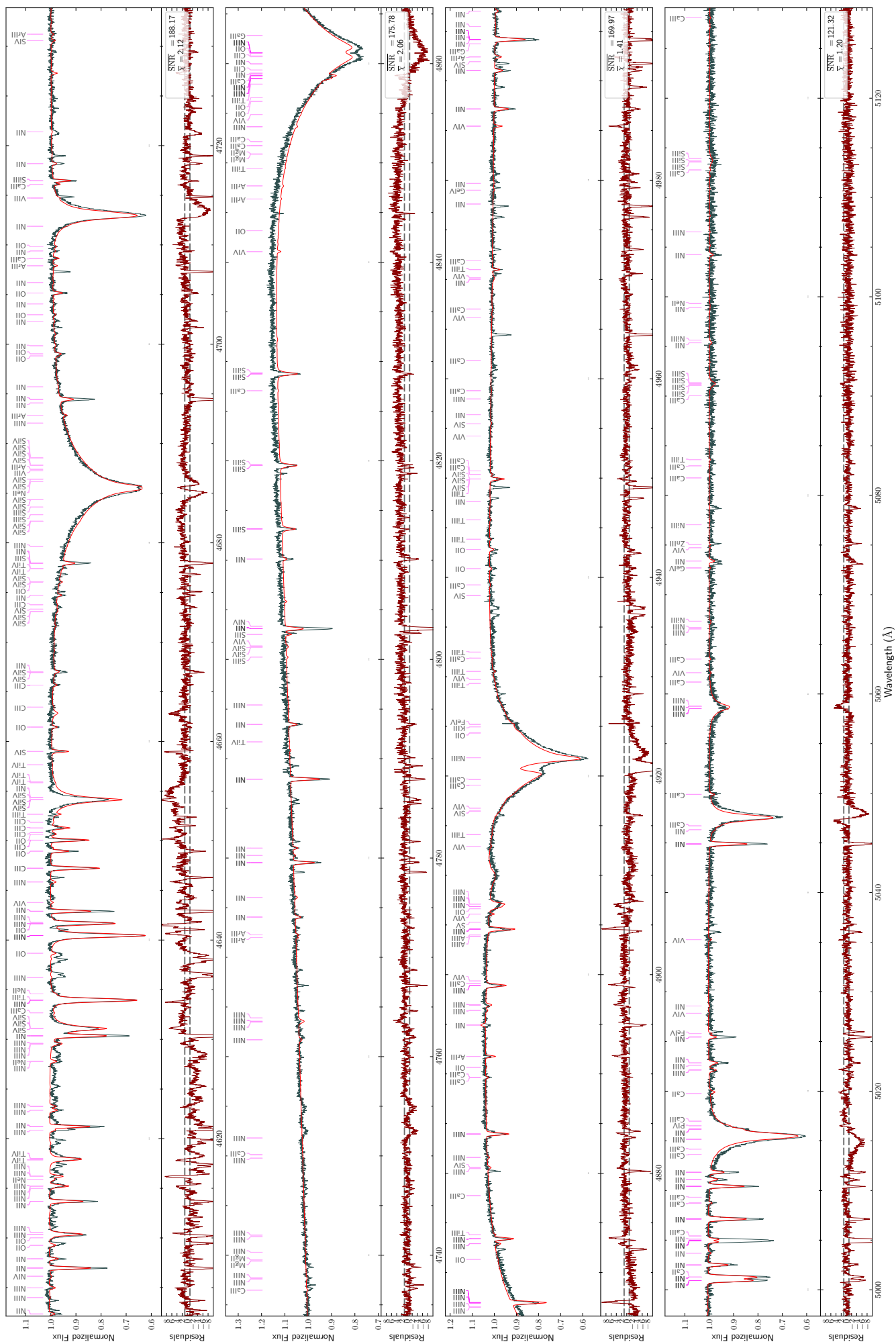
**Figure 34.** GHRS spectrum of Feige 46 (grey) and the final model with $v_{rot} \sin i = 10 \, \text{km} \, \text{s}^{-1}$ (red).
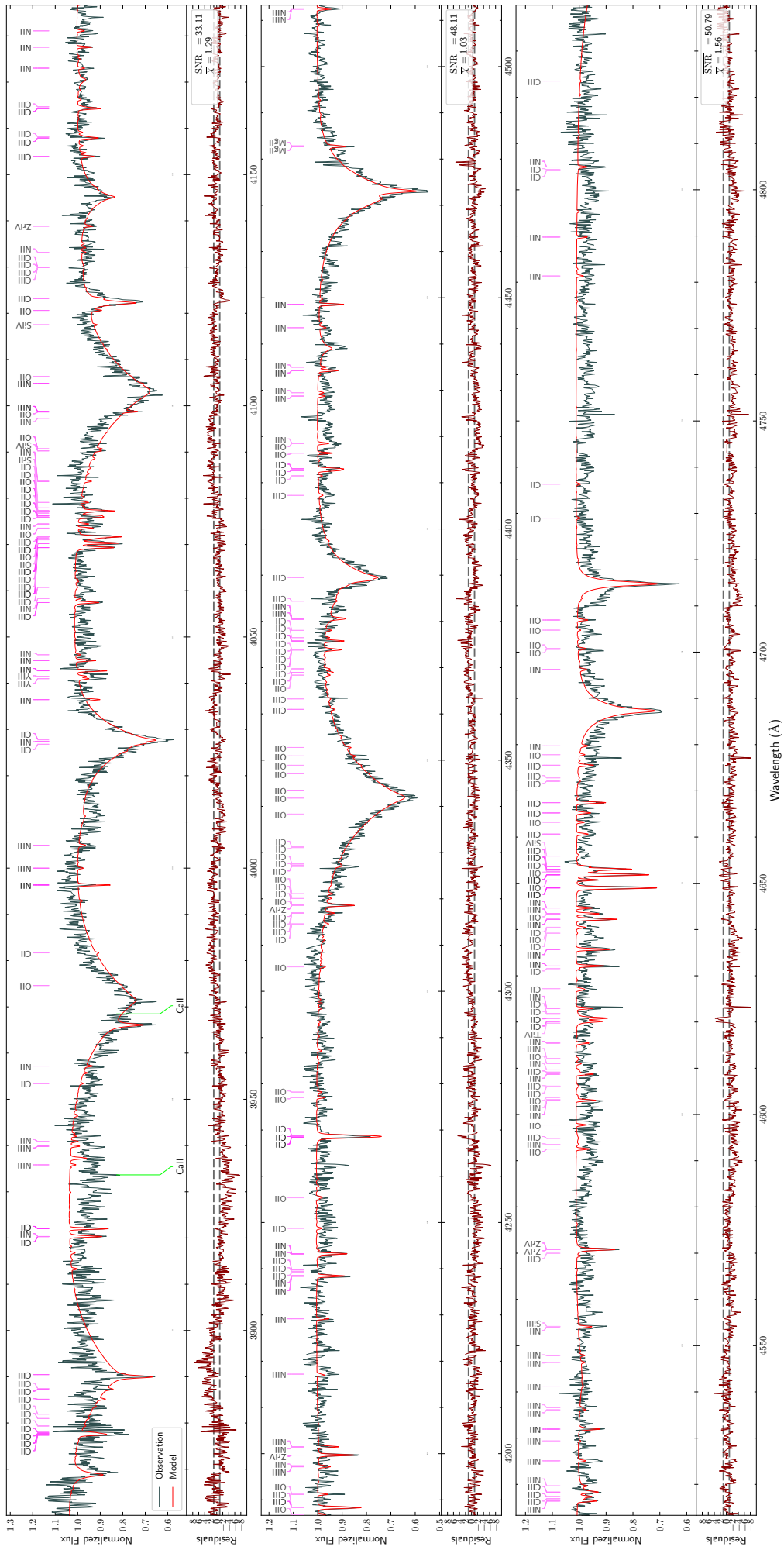
**Figure 35.** CASPEC spectrum of Feige 46 (grey) and the final model with $v_{\rm rot}\sin i = 10\,{\rm km\,s^{-1}}$ (red).

# Acknowledgments

I had a great time at the observatory. I would like to thank my supervisors Ulrich Heber and Marilyn Latour for making it possible for me to continue working on an interesting topic. They both helped me a lot throughout the thesis and answered many questions, Marilyn even from Göttingen.

Thank you to Uli for taking me to the HDEF4 conference in Armagh where I learned a lot, not only about hydrogen deficient stars. I would also like to thank the stellar group, especially David and Andreas who were always open for questions. Thanks to everyone at the observatory for making it such a nice place to work!

Finally, a big thank you to my parents for their generous support throughout all of my studies.

## Erklärung

Ich versichere, dass ich meine Masterarbeit ohne Hilfe Dritter und ohne Benutzung anderer als der angegebenen Quellen und Hilfsmittel angefertigt habe und die aus benutzten Quellen wörtlich oder inhaltlich entnommenen Stellen als solche kenntlich gemacht habe. Diese Arbeit hat in gleicher oder ähnlicher Form noch keiner Prüfungsbehörde vorgelegen.

Bamberg, den _____                        _____

Matti Dorsch